

ANALYSIS AND DESIGN OF PLANAR PERIODIC CORRUGATED ANTENNAS

By

DESPOINA KAMPOURIDOU

A thesis submitted to
the University of Birmingham
for the degree of
DOCTOR OF PHILOSOPHY



Metamaterials Engineering Laboratory
Department of Electronic, Electrical and Systems Engineering
College of Engineering and Physical Sciences
University of Birmingham
June 2020

UNIVERSITY OF
BIRMINGHAM

University of Birmingham Research Archive

e-theses repository

This unpublished thesis/dissertation is copyright of the author and/or third parties. The intellectual property rights of the author or third parties in respect of this work are as defined by The Copyright Designs and Patents Act 1988 or as modified by any successor legislation.

Any use made of information contained in this thesis/dissertation must be in accordance with that legislation and must be properly acknowledged. Further distribution or reproduction in any format is prohibited without the permission of the copyright holder.

ABSTRACT

This dissertation investigates the leaky wave properties of planar periodic corrugated metallic antennas with novel analysis and design techniques, as well as novel antennas of this type with improved farfield performance. For the first time, the dispersion analysis of one-dimensional corrugated metallic designs with gaps larger than half-wavelength is presented. A novel analytical periodic method based on a transverse resonance is developed. Additionally, a full-wave unit cell dispersion analysis tool and the matrix pencil method are employed for the leaky wave analysis of a standard corrugated design. The analytical calculation of the radiation patterns of a finite size antenna evaluates the leaky wave analysis when compared to simulated patterns. Subsequently, the improvement of the farfield performance of a practical corrugated antenna is achieved with novel antenna design techniques. The matching bandwidth of a corrugated antenna at the low THz spectrum is extended with the substitution of the typical subwavelength feeding aperture with an open-ended and, next, a tapered waveguide aperture. The 3-dB gain bandwidth of such an antenna at low THz is also enhanced, by introducing a dual-depth corrugation concept. A suitable leaky wave analysis reveals the expected characteristics of a finite size dual-depth antenna in the farfield region. Fabricated prototypes and measured results are available for the aforementioned proposed models. The final part of this thesis introduces new corrugation types at microwave frequencies towards the goal of antenna bandwidth enhancement. Such corrugations are able to produce on their own extraordinary radiation characteristics, namely flat high gain response, extended 3-dB bandwidth and improved radiation patterns.

ACKNOWLEDGMENTS

As my doctoral studies come to an end, I feel the need to acknowledge the people without whom I would not have been able to complete this dissertation.

I would like to express my deepest gratitude and appreciation for my supervisor Dr. Alexandros Feresidis for his research guidance, encouragement and feedback throughout my studies.

I would also like to thank my second supervisor Prof. Michael Lancaster, and Prof. Costas Constantinou, for the insight and useful conversations during this research endeavour.

Thanks to Alan Yates, Jag Sangha and Anthony Page for their advice and assistance with respect to the technical aspects of my work.

I am extremely grateful to the present and former researchers of the Metamaterials Engineering Laboratory for our friendly chats and collaboration during these past four years, namely Thomas Thatapudi, Evangelos Vassos, Ioannis Gerafentis, Anastasios Christodoulides, Dr. Muhammad Rabbani, Dr. James Churm and Dr. Konstantinos Konstantinidis.

I would like to acknowledge the financial support from the Department of Electronic, Electrical and Systems Engineering.

Special thanks to my lifetime friends from Greece, the wonderful people I met during my stay in Birmingham, and my family for their encouragement and emotional support during this journey.

Table of Contents

	Page
1 Introduction	1
1.1 Context of the Study	1
1.1.1 Metamaterial-Based Leaky Wave Antennas	4
1.1.2 Enhanced Transmission of Light	6
1.2 Motivation and Contribution	10
1.3 Outline of Chapters	11
References	14
2 Theoretical Background	25
2.1 Fundamentals of Leaky Waves	26
2.1.1 One-Dimensional Periodic Leaky Wave Antennas	29
2.1.2 The Problem of Radiation at Broadside	32
2.1.3 Array Factor Approach	33
2.2 Periodic Full-Wave Analysis	35
2.3 The Matrix Pencil Method	39
2.4 Periodically Corrugated Metallic Surfaces	41
2.4.1 Bull’s Eye Antennas Design Configurations	42
2.4.2 Leaky Wave Analysis of 1-D Corrugated Metallic Surfaces with Nar- row Gaps	44
2.5 Commercial Electromagnetic Solver	48

References	50
3 Leaky Wave Analysis of Periodically Corrugated Metallic Surfaces . .	54
3.1 Corrugated Metallic Antennas at 15 GHz	56
3.2 Analytical Periodic Method for Corrugated Surfaces with Large Gaps . . .	57
3.3 Unit Cell Periodic Method	61
3.4 The Application of Matrix Pencil Method on Corrugated Antennas	65
3.5 Dispersion Analysis: Numerical Results	68
3.5.1 Case of $w < \lambda_0/2$	69
3.5.2 Case of $w > \lambda_0/2$	71
3.6 Far Field Pattern Calculation	73
3.6.1 Case of $w < \lambda_0/2$	76
3.6.2 Case of $w > \lambda_0/2$	79
3.7 Conclusion	83
References	86
4 Effects of the Feeding Structure on Planar Corrugated Metal Antennas 88	
4.1 A Bull's Eye Antenna at low THz	89
4.1.1 The Subwavelength Slot Aperture	89
4.1.2 The Open-Ended Waveguide Aperture	92
4.1.3 The Tapered Waveguide Aperture	93
4.1.4 Comparison Between the Three Feeding Techniques	94
4.2 Fabricated Prototype of 300 GHz Bull's Eye with Tapered Aperture	99
4.3 Conclusion	103
References	105
5 Dual-depth corrugations for broadband Bull's Eye antennas	106
5.1 Effect of corrugations' depth h	108
5.2 The Dual-Depth Concept	109
5.2.1 Optimized Slot-Fed Dual-Depth Bull's Eye Antenna	113

5.2.2	Optimized Waveguide-Fed Dual-Depth Bull’s Eye Antenna	117
5.3	Leaky Wave Analysis of the Dual-Depth Antenna	119
5.4	Fabricated Prototype and Measured Results	122
5.5	Conclusion	126
References	128
6	Broadband Corrugated Antennas with Complex Shaped Unit Cells . .	129
6.1	The Impact of Standard Shaped Gaps on Planar Corrugated Antennas . .	130
6.2	The Perturbed Corrugation Concept	131
6.3	The Double Corrugation Concept	135
6.4	The Hybrid Corrugation Concept	138
6.4.1	Optimized Hybrid Prototype with Flat Gain Response	139
6.4.2	Optimized Prototype with Enhanced 3-dB Gain Bandwidth	144
6.5	Implementation of Different Feeding Techniques on Hybrid Corrugated Bull’s Eye Antennas	148
6.6	Conclusion	151
7	Conclusions	153
7.1	Thesis Review	153
7.2	Future Directions	156
7.3	Impact	157
A	Measurement of a Ku Band Bull’s Eye Antenna	159

List of Figures

1.1	Examples of high impedance surface applications. (a) Schematic of the mushroom type HIS (cross-section). (b) Prototype of holographic antenna excited by a microstrip patch antenna (from [28]).	5
1.2	Fabry-Perot cavity antenna. (a) Schematic of single layer antenna. (b) Fabricated multi-layer prototype at 14 GHz (from [35]).	6
1.3	Corrugated metallic surface.	7
1.4	Popular corrugated antenna implementations (a) a 16 GHz Bull's Eye antenna (from [61]), (b) a 60 GHz Bull's Eye antenna with high aperture efficiency (from [64]).	9
2.1	A unidirectional leaky wave antenna of infinite size on the xy plane.	27
2.2	One-dimensional periodic leaky wave antenna.	30
2.3	Bidirectional (symmetrically-fed) leaky wave antenna.	33
2.4	Array factor of a unidirectional leaky wave antenna.	34
2.5	A periodic unit cell (a) 2-D lattice (b) corresponding Brillouin zone.	36
2.6	Setup of field sampling points for the calculation of the complex wavenumber.	37

2.7	Alternative setup of field sampling points for the calculation of the complex wavenumber.	39
2.8	Front view of a standard Bull's Eye antenna with a subwavelength slot aperture.	42
2.9	A subwavelength resonant slot on an infinite ground plane.	43
2.10	1-D infinite size corrugated metallic plane with $w < \lambda_0/2$	45
3.1	1-D periodically corrugated structure with $d \sim \lambda_0$, $h \sim \lambda_0/4$ and (a) $w < \lambda_0/2$ and (b) $w > \lambda_0/2$	56
3.2	Boundary conditions for the implementation of the unit cell periodic method in CST. Periodic boundary conditions are imposed at x, y axes, open boundary is chosen along $+z$ and PEC is chosen along $-z$ axis.	62
3.3	Unit cell setup for the calculation of β_{-1} (a) case of $w < \lambda_0/2$ and (b) case of $w > \lambda_0/2$	63
3.4	Simulated E -field of a corrugated unit cell at 15 GHz with (a) $w < \lambda_0/2$ and (b) $w > \lambda_0/2$	64
3.5	Unit cell setup for the calculation of α (a) case of $w < \lambda_0/2$ and (b) case of $w > \lambda_0/2$	65
3.6	Front view of the 2D corrugated antenna geometry. The blue rectangular defines the sampling domain for the H_x component to be approximated by the matrix pencil method, just above the level of corrugations.	67

3.7	Complex wavenumber distribution of k_{y-1} for the narrow gap case (a) phase constant β_{-1} and (b) attenuation constant α	70
3.8	Complex wavenumber distribution of k_{y-1} for the wide gap case (a) phase constant β_{-1} and (b) attenuation constant α	72
3.9	Symmetrically-fed corrugated antennas (a) narrow gap case and (b) wide gap case.	74
3.10	Radiating slot aperture on an infinite ground plane surrounded by one corrugated ring.	75
3.11	Simulated (maximum) E -field at 14.8 GHz for the narrow gap antenna. . .	76
3.12	Normalized radiation patterns of the 18-unit cell narrow gap antenna at (a) 14.8 GHz, (b) 13 GHz.	78
3.13	Simulated E_y -field (maximum) at 14.2 GHz for the wide gap antenna. . . .	79
3.14	Phase animation of the simulated E_y -field at 14.2 GHz (a) 0° (b) 90°	80
3.15	Normalized radiation patterns of the 26-unit cell wide gap antenna at (a) 14.2 GHz, (b) 13.2 GHz.	82
3.16	Effect of the TEM mode on the radiation patterns of the 26-unit cell wide gap antenna at (a) 14.2 GHz, (b) 13.2 GHz.	83
4.1	Bull's Eye antenna with slot aperture (a) Front view (b) Side view.	90
4.2	Simulation study for number of rings vs maximum directivity at around 300 GHz (feeding via a subwavelength slot).	91

4.3	Simulated performance of Bull’s Eye antenna with slot aperture at around 300 GHz.	91
4.4	Open-ended waveguide aperture design (a) xz plane, (b) yz plane.	93
4.5	Simulated performance of Bull’s Eye antenna with open-ended waveguide aperture at around 300 GHz.	93
4.6	Tapered waveguide aperture design (a) xz plane, (b) yz plane.	94
4.7	Simulated performance of Bull’s Eye antenna with tapered waveguide aperture at around 300 GHz.	94
4.8	Simulated S11 comparison between three feeding aperture types on a bare ground plane at around 300 GHz.	95
4.9	Simulated directivity comparison between three feeding aperture types on a bare ground plane at 300 GHz.	97
4.10	Comparison of simulated radiation patterns at various frequencies of interest for the three types of Bull’s Eye antennas. E -plane (a) lower -3 dB, (c) 0 dB, (e) upper -3 dB. H -plane (b) lower -3 dB, (d) 0 dB, (f) upper -3 dB.	98
4.11	Fabricated prototype of the tapered Bull’s Eye antenna at 300 GHz.	99
4.12	Measured S11 of the tapered Bull’s Eye antenna compared to simulated.	100
4.13	Measured realized gain of the tapered Bull’s Eye antenna compared to simulated.	100
4.14	Setup for radiation pattern measurement at 300 GHz.	101

4.15	Normalized H -plane measurements of the tapered Bull's Eye antenna compared to simulated, at (a) lower -3 dB, (b) 0 dB, (c) upper -3 dB.	102
5.1	1-D corrugated metallic antenna at 300 GHz (a) Front view of antenna (b) Unit cell.	107
5.2	Simulated effect of depth h on the 1-D corrugated antenna of Fig. 5.1 with (a) S11 (b) Directivity.	108
5.3	Schematic of the dual-depth Bull's Eye antenna with $N = 8$ (a) perspective (b) profile.	110
5.4	Simulated S11 of Bull's Eye antennas of $N = 10$ for different sets of h_1, h_2 (a) (0.14 mm, 0.18 mm), (b) (0.14 mm, 0.21 mm), (c) (0.14 mm, 0.24 mm), (d) (0.14 mm, 0.266 mm).	111
5.5	Simulated directivity of Bull's Eye antennas of $N = 10$ for different sets of h_1, h_2 (a) (0.14 mm, 0.18 mm), (b) (0.14 mm, 0.21 mm), (c) (0.14 mm, 0.24 mm), (d) (0.14 mm, 0.266 mm).	112
5.6	Simulated (a) S11 and (b) directivity of Bull's Eye antennas of $N = 10$ for ($h_1, h_2 = (0.24 \text{ mm}, 0.14 \text{ mm})$).	113
5.7	Comparison between three slot-fed Bull's Eye antennas (simulation results). The dual-depth antenna is compared with (a) the h_1 antenna and (b) the h_2 antenna.	115

5.8	Simulated E - and H - planes at the 3-dB spectrum of the dual-depth and the single depth antennas of the same maximum directivity. E -plane: (a) lower -3 dB, (c) 0 dB, (e) upper -3 dB. H -plane: (b) lower -3 dB, (d) 0 dB, (f) upper -3 dB.	116
5.9	Simulated S11 of waveguide-fed Bull's Eye antennas with $N=10$	118
5.10	Leaky-wave analysis of each single depth antenna (a) propagation constant and (b) attenuation constant.	120
5.11	Fabricated dual-depth antenna at 300 GHz.	123
5.12	Infrared scan of the fabricated dual-depth antenna at 300 GHz.	124
5.13	Measured versus simulated (a) S11 parameters and (b) Realized gain of the waveguide aperture fed Bull's Eye antenna. The simulated results refer to the redesigned antenna.	125
5.14	Normalized H -plane measurements at (a) 281.2 GHz, (b) 288.1 GHz, (c) 296 GHz, (d) 304.2 GHz.	126
5.15	Normalized E -plane measurements at (a) 281.2 GHz, (b) 284.2 GHz, (c) 296 GHz, (d) 304.2 GHz.	127
6.1	A comparative study between gap width w , peak realized gain and 3-dB gain bandwidth for a 2D corrugated antenna with six rings at around 15 GHz (simulation results).	131
6.2	Cross section of a metallic unit cell with perturbed corrugation (design details).	132

6.3	Perturbed Bull’s Eye antenna with 6 rings and waveguide aperture. (a) Front view, (b) Profile.	133
6.4	Simulation results for the Bull’s Eye antenna of Fig. 6.6 (a) $w = 4$ mm, (b) $w = 9$ mm, (c) $w = 12$ mm.	134
6.5	Cross section of corrugated metallic unit cell with double corrugation (design details).	135
6.6	Double corrugated Bull’s Eye antenna with 6 rings and waveguide aperture. (a) Front view. (b) Profile.	136
6.7	Simulation results for the Bull’s Eye antenna of Fig. 6.6 (a) $w = 4$ mm, (b) $w = 9$ mm, (c) $w = 12$ mm.	137
6.8	Cross section of corrugated metallic unit cell with hybrid corrugation (design details).	138
6.9	Hybrid corrugated Bull’s Eye antenna with 6 rings and waveguide aperture. (a) Front view. (b) Profile.	139
6.10	Simulation results of an optimized hybrid Bull’s Eye antenna with flat gain response and comparison with a standard Bull’s eye antenna with similar directivity/gain in (a) S11, (b) Directivity and realized gain.	140
6.11	Contribution of each corrugation type in the hybrid effect of the flat gain antenna.	141

6.12	Simulated radiation patterns of the hybrid antenna with flat gain and the standard antenna of the same maximum gain. <i>E</i> -plane: (a) lower -1 dB, (c) 0 dB, (e) upper -1 dB. <i>H</i> -plane: (b) lower -1 dB, (d) 0 dB, (f) upper -1 dB.	142
6.13	Simulated <i>E</i> -field magnitude of each corrugated unit cell case for $\beta=0$. . .	143
6.14	Simulation results of an optimized hybrid Bull's Eye antenna with enhanced 3-dB gain bandwidth response and comparison with a standard Bull's eye antenna with similar directivity/gain in (a) S11, (b) Directivity and realized gain.	145
6.15	Contribution of each corrugation in the hybrid effect of the antenna with enhanced 3-dB gain bandwidth.	146
6.16	Simulated radiation patterns of the hybrid antenna with enhanced 3-dB gain bandwidth and the standard antenna of the same maximum gain. <i>E</i> -plane: (a) lower -3 dB, (c) 0 dB, (e) upper -3 dB. <i>H</i> -plane: (b) lower -3 dB, (d) 0 dB, (f) upper -3 dB.	147
6.17	Comparison of the optimized hybrid Bull's Eye antenna with flat response with three different feeding techniques in simulated (a) S11, (b) realized Gain and (c) directivity.	150
A.1	Fabricated prototype of a 15 GHz standard Bull's Eye antenna.	159
A.2	Measured (a) S11 and (b) Realized Gain of the standard Bull's Eye antenna with tapered aperture compared to the simulated results.	160

A.3 Measured far-field radiation patterns of the tapered Bull’s Eye antenna at
12.5 GHz: (a) *H*-plane and (b) *E*-plane, 13.5 GHz: (c) *H*-plane and (d)
E-plane, and 14.7 GHz: (e) *H*-plane and (f) *E*-plane. 161

List of Tables

3.1	Numerical convergence at 14.2 GHz.	61
3.2	Matrix pencil extracted components of the 2D narrow gap antenna at 13 GHz.	68
3.3	Matrix pencil extracted components of the 2D wide gap antenna at 12.5 GHz.	68
3.4	Broadside range for the narrow gap antenna at 15 GHz.	77
3.5	Broadside range for the wide gap antenna at 15 GHz.	81
4.1	Far field performance comparison of the three antennas at 300 GHz.	96
5.1	Slot-fed dual-depth Bull's Eye antenna with N=8 at around 300 GHz.	114
5.2	Slot-fed dual-depth Bull's Eye antenna with N=10 at around 300 GHz.	114
5.3	Slot-fed dual-depth Bull's Eye antenna with N=12 at around 300 GHz.	114
5.4	Waveguide-fed dual-depth Bull's Eye antenna with N=10 at around 300 GHz.	118

List of Symbols and Abbreviations

α	Attenuation constant (leakage rate)
β	Phase (propagation) constant
c	Speed of light
k	Wavenumber
AF	Array factor
BW	Bandwidth
E	Electric field
H	Magnetic field
$GBWP$	Gain-bandwidth product
LW	Leaky wave
MPM	Matrix pencil method
PBC	Periodic boundary condition
PEC	Perfect electric conductor
SLL	Side lobe level

List of Publications

Journal Papers

- D. Kampouridou, A. Feresidis, "Leaky-wave Analysis and Radiation Patterns of 1-D Periodic Corrugated Metal Surfaces", *IEEE Antennas and Wireless Propagation Letters*, accepted subject to corrections.
- D. Kampouridou, A. Feresidis, "Broadband Low-THz All-metal Bull's Eye Antennas", submitted to *IEEE Transactions on Terahertz Science and Technology*, under review.
- D. Kampouridou, A. Feresidis, "Bandwidth Enhancement Technique for Complex Shaped Bull's Eye Antennas", in preparation for submission to *IEEE Access* or *Nature Scientific Reports*.
- D. Kampouridou, A. Feresidis, "Broadband Complex Shaped Bull's Eye Antenna", in preparation.

Conference Papers

- D. Kampouridou, A. Feresidis, "A New Design Technique for Broadband Bull's Eye Antennas at low THz", *2020 IEEE International Symposium on Antennas and Propagation (APS)*.

- D. Kampouridou, A. Feresidis, " Leaky Wave Analysis of Periodic Corrugated Metallic Plates with Complex Shapes", *2020 European Conference on Antennas and Propagation (EuCAP)*.
- D. Kampouridou, A. Feresidis, "A New Design Concept for Broadband Bull's Eye Antennas", *2020 International Workshop on Antenna Technology (iWAT)*.
- D. Kampouridou, A. Feresidis, "Dispersion Analysis of 1-D Periodic Corrugated Metallic Surface Antennas", *2019 European Conference on Antennas and Propagation (EuCAP)*.
- D. Kampouridou, A. Feresidis, 'Dispersion Analysis of Corrugated Ground-Plane Antenna', *2018 Loughborough Antennas and Propagation Conference (LAPC)*.
- D. Kampouridou, A. Feresidis, "Effects of the Feeding Structure on Low-THz Bull's Eye Antennas", *2018 European Conference on Antennas and Propagation (EuCAP)*.
- D. Kampouridou, A. Feresidis, "A new THz Corrugated-ground antenna", *2017 Loughborough Antennas and Propagation Conference (LAPC)*.
- D. Kampouridou, K. Konstantinidis, M. Mavridou, A. Feresidis, "An Improved Millimeter-Wave Bull's Eye Antenna", *2017 European Conference on Antennas and Propagation (EuCAP)*.

Chapter 1

Introduction

This Chapter presents a brief introduction of the background and motivation of the research work in this Thesis. A summary of leaky wave fundamental concepts is given. A special phenomenon known as enhanced transmission of light is described, which inspired many aspects of the present research. The Chapter concludes with the motivations and objectives of the thesis, along with the outline of Chapters.

1.1 Context of the Study

A class of antennas that has been of particular interest in recent decades is *leaky wave antennas*, which support a travelling wave on a guiding structure as the main radiating mechanism. Their main advantages are their typical high gain performance, beam scanning capability with frequency, low cost and simple design requirements [1].

The inherent beam-scanning capabilities and low profile structure of leaky wave antennas allow their easy integration with microwave and millimeter-wave systems and feeding networks. They can reduce the complexity of many systems that require high gain and low

cost beam-scanning mechanisms, such as automotive radar systems, multi-point communications (multi-beam requirements), and surveillance applications [2–4]. In particular, leaky wave antennas are suitable candidates for meeting the demands of modern and emerging mass mobile communications systems (5G) which typically require high gain, high antenna efficiency and dynamic coverage. Additionally, the easy incorporation of tuning technologies in the antenna design paves the way for the development of active beam-steerable leaky wave antennas for such mobile networks [5, 6].

With respect to their physics formalism, leaky wave antennas launch a wave that is characterized by a longitudinal complex wavenumber k_{LW} , with its phase constant β smaller than the free space wavenumber k_0 (characterized as *fast wave*) [1, 7, 8]. Leaky wave antennas can be classified either as one-dimensional (1D) or two-dimensional (2D), or characterized between uniform, quasi-uniform and periodic [1].

An open rectangular waveguide with a long slit across its length is an example of a *1D uniform* leaky wave antenna, which is the first known leaky wave antenna, introduced by Hansen in 1940 [9]. The term "uniform" is justified by the fact that the geometry is constant along the length of the structure. The fundamental mode is a fast wave ($\beta < k_0$) which radiates (leaks) in free space.

In *1D periodic* leaky wave antennas, a periodic modulation along the length of the structure was introduced. An example of such an antenna was the proposed by Hines and Upson "holey waveguide" filled with dielectric material, which was a replacement of the long longitudinal slit with closely spaced holes, achieving a narrow radiating beam [10]. The periodic discontinuities convert the slow guided mode, which is a non-radiating wave with $\beta > k_0$, into a radiating (leaky) mode. This guided mode consists of an infinite

number of n space harmonics, known as Floquet waves, one of which is designed to be a fast wave (usually the $n = -1$), while the fundamental mode ($n = 0$) is a non-radiating surface wave [11].

The case of the *1D quasi uniform* leaky wave antenna is similar to the uniform leaky wave antenna, except that it consists of a periodic modulation. Quasi-uniform leaky wave antennas support a fundamental mode which is a fast wave, in contrast to 1D periodic antennas. An example of such an antenna is the holey waveguide of [10], when the waveguide is air filled, therefore the fundamental TE_{10} mode is a fast, radiating wave.

Although 1D geometries have been initially studied for microwave frequencies, in recent years 2D implementations have gathered research interest that can reach up to optical frequencies. A 2D planar leaky wave antenna implementation is a very simple solution to the problem of radiation at broadside which exhibit most 1D implementations [1, 12, 13]. They can produce a pencil beam at broadside when the phase constant and the attenuation constant of the leaky mode are nearly equal, as further discussed in Chapter 2.

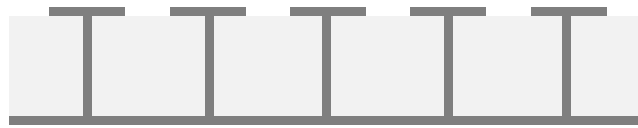
Leaky waves on periodic surfaces were first investigated by Oliner and Hessel on sinusoidally-modulated reactance surfaces [14]. Later, a 2D leaky wave antenna was investigated in [15], consisting of a high permittivity dielectric superstrate over a substrate and studied as a leaky wave antenna in [16]. The research on planar leaky wave antennas has been facilitated in the past decades due to the advent of metamaterial engineering technology [1, 4, 17].

1.1.1 Metamaterial-Based Leaky Wave Antennas

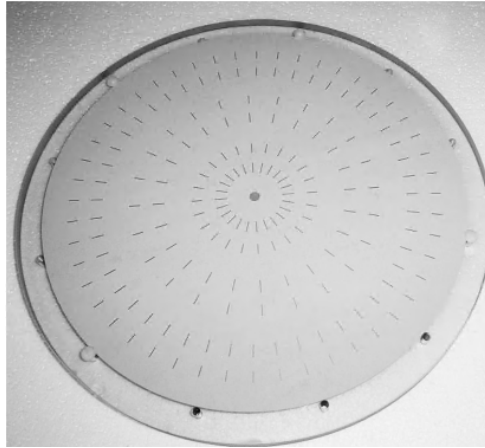
Metamaterials are artificial periodic electromagnetic structures that offer properties not found in nature. The size of their unit cell is usually subwavelength, and the desired properties can be obtained by engineering accordingly their shape, geometry, orientation and overall size [18]. The planarized version of metamaterials forms periodically modulated surfaces, known as *metasurfaces* [19, 20]. The investigation of such artificial materials has inspired a variety of applications on leaky wave antennas, with the advantages of low profile, ease of fabrication and clear design guidelines. Such developments have facilitated research in microwave and millimeter wave frequencies, as well as in optical frequencies (optical waveguides, optical antennas).

A recent development related to the concept of metasurface leaky wave antenna is that of a *high-impedance surface (HIS)*, proposed by Sievenpiper *et al.* in [21]. This surface typically consists of a periodic texture on a metallic surface behaving as an artificial magnetic conductor (AMC). A proposed design in [21] is the mushroom type HIS (Fig. 1.1.a). Based on the concept and special properties of HIS, several antennas have been proposed (static or reconfigurable), including reflectarrays [22], electronically tunable surfaces and leaky wave antennas [23–26]. The concept of holography, combined with the principle of high impedance surfaces, has produced high gain beam steerable leaky wave antennas with very low profile [27–29]. An example of a holographic antenna inspired structure can be viewed in Fig. 1.1.b.

Fabry-Perot (FP) cavity type antennas are another popular family of high gain planar leaky wave antennas (Fig. 1.2). Their principle of operation derives from the typical Fabry-Perot interferometer cavities, used in optical frequencies. An FP antenna typically



(a)



(b)

Figure 1.1: Examples of high impedance surface applications. (a) Schematic of the mushroom type HIS (cross-section). (b) Prototype of holographic antenna excited by a microstrip patch antenna (from [28]).

consists of a *Partially Reflective Surface (PRS)* placed at a distance h from a metallic or, as more recently presented, a High Impedance Surface. These antennas were initially investigated by von Trentini, who used a PRS over a ground plane [30], and proposed design guidelines for such antennas based on the phase profile of the PRS. In later research, the characteristics of PRSs were investigated towards the bandwidth enhancement of FP antennas by associating the PRS phase to linearly increase with frequency [31, 32], and multi-layer configurations were later proposed for this purpose [33–35]. FP cavity antennas have been studied as leaky wave antennas in recent work [36, 37], as they are capable of scanning the beam with frequency.

Other metamaterial-inspired leaky wave antennas include the application of composite right/left handed metamaterials (CRLH), first introduced in [38–40], that tackle the

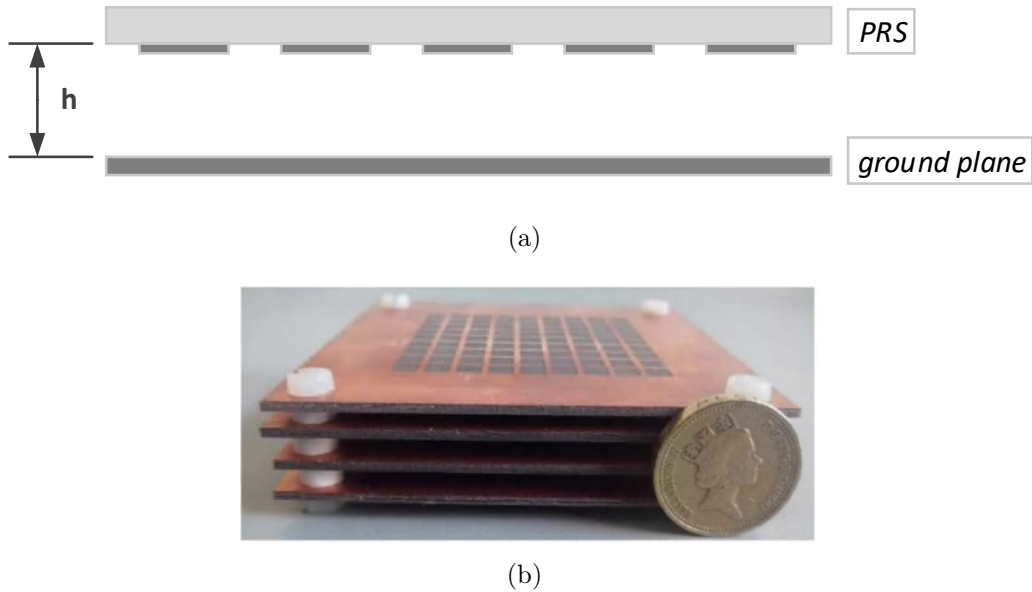


Figure 1.2: Fabry-Perot cavity antenna. (a) Schematic of single layer antenna. (b) Fabricated multi-layer prototype at 14 GHz (from [35]).

inherent incapability of leaky wave antennas of continuously scanning towards broadside without beam degradation [41]. The CRLH metamaterial design consists of a periodic arrangement of inductor and capacitor elements within a transmission line unit cell. Some implementations can be found in [42, 43], while tunable versions of CRLH leaky wave antennas are available [44].

1.1.2 Enhanced Transmission of Light

In the optics community, one of the most popular breakthrough in research in the past few decades has been the observation of extraordinary transmission of light through a subwavelength aperture on a metallic film, such as silver or gold [45, 46]. Early studies in the past had shown that the percentage of power transmitted through a hole on an infinite metallic film is usually very small, due to diffraction [47]. However, Ebbesen *et al.*

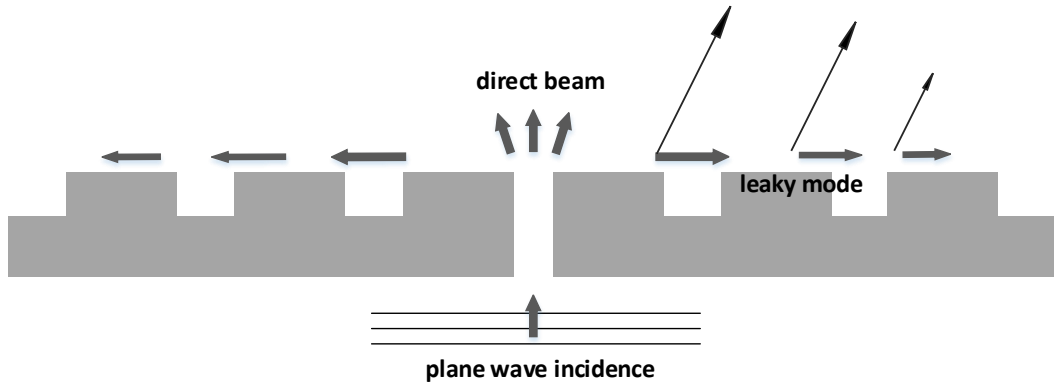


Figure 1.3: Corrugated metallic surface.

demonstrated experimentally that when an aperture is surrounded by a periodic array of corrugations on the exit face of the film, the power transmission is dramatically enhanced by several orders of magnitude [46, 48]. This effect, known as *enhanced transmission of light*, has been also observed for a periodic array of subwavelength holes [49–51].

At optical frequencies, a highly conducting metallic film (silver or gold) behaves like a plasmonic material, meaning that it is characterized by a dispersive permittivity with a negative real part and can be modeled by a lossless Drude equation. An air/metal interface at these frequencies supports a *TM* surface wave, known as *surface plasmon* [54], with direction normal to the interface and a longitudinal wavenumber k_p given by

$$k_p = k_0 \sqrt{\frac{\epsilon_r}{1 + \epsilon_r}} \quad (1.1)$$

where k_0 is the free space wavenumber and ϵ_r is the relative permittivity of the metal with Drude dispersion [55]. From (1.1), it is obvious that for any $\epsilon_r < -1$, the surface plasmon mode is a slow wave with $k_p > k_0$ and therefore does not radiate.

In later years, it has been demonstrated that this effect can be observed not only in optical frequencies but also in microwave and millimetre-wave frequencies [52, 53]. It was

discovered that a surface plasmon mode is responsible for the enhanced power transmission and the consequent directive beaming phenomenon. Leaky wave theory was then introduced by Oliner and Jackson for the explanation of the directive beaming effect [56–59].

In the context of leaky wave antennas, a periodic modulation on the metallic interface can convert the aforementioned surface plasmon (slow) mode into a leaky (fast) mode [1]. The surface mode consists of an infinite set of space harmonics (Floquet harmonics), only one of which is engineered to be a fast wave, therefore producing the leaky wave radiation [11]. Design guidelines can be deduced from the wavenumber of the leaky mode, such as the elevation angle of the main beam, the beamwidth and the size of the antenna [1].

An early 1D implementation with periodic narrow slits over a dielectric substrate was introduced in [60], inspired by the enhanced transmission of light phenomenon. A popular 2D implementation of a periodically corrugated metallic plane is the Bull’s Eye antenna [61]. It typically consists of a subwavelength aperture on a metallic film, surrounded by a number of rings etched off the film (Fig. 1.4). The rings are modulated with period d , at the order of the free space wavelength. The shape of corrugations can be the standard rectangular shape, or even wedge [62] or V-type [63]. Such antennas exhibit high gain and broadside radiation in the microwave and millimetre wave spectrum [64]. Reported antennas of this type can consist of sinusoidal corrugations [65], achieve off-axis beaming with the use of 3-D printing technology [66] and can also be used as feeders [67] or superimposed with dielectric layers for CubeSat applications [68]. Moreover, Bull’s Eye antennas in printed substrate technology have been introduced recently, which consist of annular metallic strips printed onto a dielectric substrate [69–71].

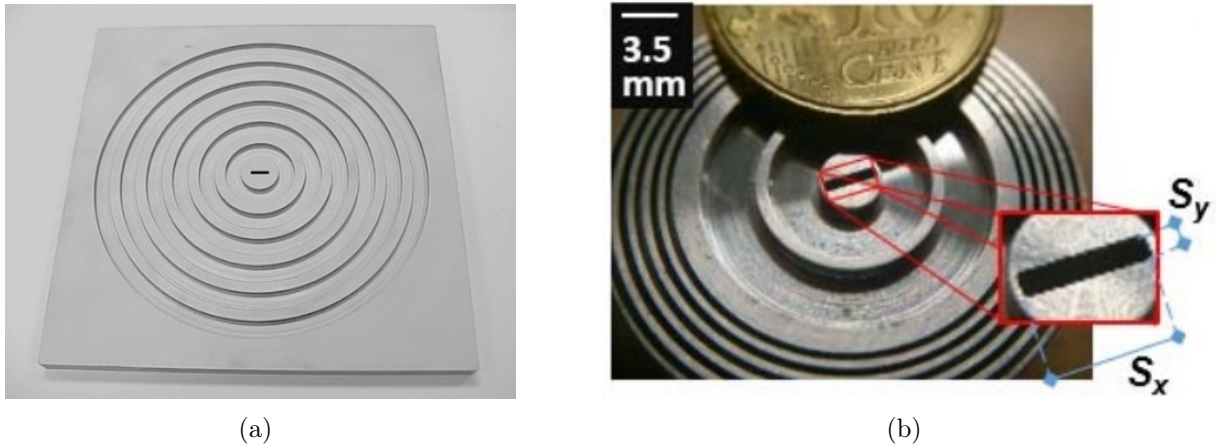


Figure 1.4: Popular corrugated antenna implementations (a) a 16 GHz Bull's Eye antenna (from [61]), (b) a 60 GHz Bull's Eye antenna with high aperture efficiency (from [64]).

The interesting performance features of corrugated antennas, which include higher gain radiation patterns and narrower beams compared to standard horn antennas, have attracted a variety of applications in communications and sensing. A mm-wave Bull's Eye antenna has been proposed in literature due its very low profile for integration into a CubeSat device, which is a small satellite to be used in swarms for point-to-point and multipoint-to-point communications [72]. Corrugated structures have also been used along with lenses in higher frequency (THz) applications, in particular, fiber coupling, imaging and laser collimation with improved signal-to-noise ratio [73].

Corrugated structures have been proposed in the field of renewable energies, as heat harvesting devices for the photosensitive cells arranged in photovoltaic panels [74]. Towards the visible and infrared spectrum, such structures have found application in multicolor sensing devices, due to their selective conversion between free-space waves and spatially confined modes [75].

1.2 Motivation and Contribution

Periodically corrugated low-profile antennas, in microwave and millimetre wave frequencies, have recently attracted significant research interest due to the simplicity of their design, simple feeding network and high gain performance. This dissertation is focused on the analysis of such periodic surfaces and antennas as leaky wave structures and introduces new techniques for the improvement of their performance.

The electromagnetic analysis of corrugated metallic surfaces has been a complex problem due to the strong mathematical background it involves. The study of such structures as leaky wave antennas and the extraction of their longitudinal complex wavenumber is available in classic electromagnetic books [76, 77], however it only involves structures composed of corrugations with narrow gaps compared to the resonant free space wavelength [76–78]. The associated analysis considers only the fundamental supported mode inside the gaps, while practical corrugated antennas with narrow gaps exhibit low realized gain. Although most published implementations use large gaps as a high gain prerequisite [61, 72], their dispersion analysis hasn't been realized so far.

In this thesis, the **first contribution** is the leaky wave analysis of periodically corrugated surfaces with both narrow *and* large gaps, with the use of novel analysis tools. These tools involve the solution of numerical equations based on transverse resonance techniques, reciprocity and eigenmode analysis. Also, an inspection of the electromagnetic fields in the near field of the antennas assists in the analytical calculation of the radiation patterns of the antenna.

The **second contribution** of this dissertation is to enhance the performance of the standard Bull's Eye antenna, in terms of input impedance matching performance. De-

spite the highly directive performance of antennas which use the typical subwavelength slot aperture, the matching bandwidth, and thus the achievable realized gain, is limited. A broadband performance in S11 is required for the improvement of gain and/or for situations where a superimposed dielectric layer would affect the matching. For this purpose, novel feeding techniques are proposed in this thesis which improve the antenna S11 parameters.

Another common problem met with Bull's Eye antennas is their typically limited 3-dB gain (or directivity) bandwidth. The **third contribution** of this work is to offer a novel design technique towards the gain bandwidth enhancement of corrugated antennas. A novel Bull's Eye antenna at low THz is introduced, that outperforms known realizations in this frequency spectrum. The antenna achieves a broadband performance while maintaining a high realized gain, and its operation is explained from leaky wave analysis.

The **fourth contribution** of this work is the development of novel types of complex-shape periodic corrugations that not only enhance the 3-dB gain bandwidth, but also achieve a nearly flat gain response with a broad 1-dB bandwidth. The operation of this design is also explained using leaky wave analysis. To the author's knowledge, this is the first time that optimised complex shaped corrugations achieve a significant improvement in the bandwidth of Bull's eye type antennas.

1.3 Outline of Chapters

The outline of this dissertation is briefly described in this Section. This Chapter is the first, introductory Chapter of the thesis, with the classification of leaky wave antennas along with recent implementations inspired by metamaterial concepts. Special focus is

given to the phenomenon of enhanced transmission of light, which led to the development of numerous high gain leaky wave antennas.

Chapter 2 offers the mathematical background of the dissertation. The mathematical formalization of leaky waves allows the comprehension of their radiation characteristics such as main beam angle, width and antenna size. Known dispersion analysis tools are described, including a Finite-Difference Time-Domain (FDTD) analysis for the full-wave calculation of the leaky mode from a setup of periodic unit cells and an eigenmode methodology of the near radiating fields of a finite size antenna. Special attention is given on the leaky wave analysis of periodically corrugated metal surfaces with narrow gaps, along with design guidelines for the corresponding 1D and 2D implementations.

Chapter 3 presents a novel analytical periodic method for the dispersion analysis of 1D periodically corrugated surfaces with large gaps. This method considers a higher order mode propagation inside the gaps. In addition, a full-wave dispersion analysis technique and a known eigenmode dispersion analysis technique are applied for the first time on this type of corrugated antennas. Results for optimized designs of both narrow and wide gaps are presented, and the accuracy of the three methods is discussed. The farfield behaviour of the infinite size symmetrically-fed antennas is then calculated with the array factor approach. An analytical investigation of the electric and magnetic fields near the corrugations assists towards this goal. The theoretically calculated radiation patterns of finite size antennas for both narrow and wide gap cases are compared with simulated models and a very good agreement is observed.

Chapter 4 discusses the effects of the feeding structure on Bull's Eye antennas. The typically limited matching performance of the feeding slot aperture is overcome via its

substitution by an open ended waveguide aperture. An even better matching performance is achieved with the outward tapering of the waveguide aperture. A prototype at a low-THz frequencies has been fabricated and measured results are available.

In Chapter 5, the problem of the limited 3-dB bandwidth of most Bull's Eye antennas is addressed. A design technique is proposed which exploits the depth qualities of the corrugations. The design process of a dual-depth corrugated antenna at 300 GHz is explained and a suitable leaky wave analysis gives further insight into the performance of such a design. The optimum model was fabricated and measured results are presented.

Chapter 6 offers another approach to the problem of limited 3-dB bandwidth of Bull's Eye antennas, by introducing novel types of complex shaped corrugations. These corrugations are applied directly on planar designs at microwave frequencies. For the optimum 2D model at 15 GHz, the 3-dB gain bandwidth is enhanced and a very large 1-dB gain bandwidth is observed (flat gain response). A leaky wave analysis reveals two existing leaky modes on this type of complex shaped antenna. A second optimum model is presented, which achieves a significant enhancement in 3-dB gain bandwidth, along with highly directive radiation patterns. The optimum prototype with flat gain response was fabricated, however measurements could not be performed due to restricted campus operations.

Chapter 7 is the conclusion of this work. The findings of this research are briefly discussed and guidelines for future work are suggested.

References

- [1] D. R. Jackson, A. A. Oliner, C. Balanis, "Leaky-wave antennas" in *Modern Antenna Handbook*, New York, NY, USA:Wiley, 2008.
- [2] D. K. Karmokar, K. P. Esselle, and S. G. Hay, "Fixed-Frequency Beam Steering of Microstrip Leaky-Wave Antennas using Binary Switches," in *IEEE Transactions on Antennas and Propagation*, vol. 64, no. 6, pp. 2146-54, 2016.
- [3] D. K. Karmokar, Y. J. Guo, P. Qin, K. P. Esselle and T. S. Bird, "Forward and Backward Beam-Scanning Tri-Band Leaky-Wave Antenna," in *IEEE Antennas and Wireless Propagation Letters*, vol. 16, pp. 1891-1894, 2017, doi: 10.1109/LAWP.2017.2685439.
- [4] F. Monticone and A. Alu, "Leaky-Wave Theory, Techniques, and Applications: From Microwaves to Visible Frequencies," *Proc. IEEE*, vol. 103, no. 5, pp. 793–821, 2015.
- [5] M. S. Rabbani, J. Churm and A. Feresidis, "Millimetre-wave beam steerable leaky-wave antenna for 5G systems," *12th European Conference on Antennas and Propagation (EuCAP 2018)*, London, 2018, pp. 1-4.
- [6] Y. El Gholb, M. Poveda-Garcia, J. L. G. Tornero, J. M. Molina-Garcia-Pardo and N. El Amrani El Idrissi, "A Mobile Terminal Leaky-Wave Antenna for Efficient 5G

- Communication," *2019 IEEE-APS Topical Conference on Antennas and Propagation in Wireless Communications (APWC)*, Granada, Spain, 2019, pp. 402-402.
- [7] A. Sutinjo, M. Okoniewski, and R. H. Johnston, "Radiation from fast and slow traveling waves," *IEEE Antennas Propag. Mag.*, vol. 50, no. 4, pp. 175–181, Aug. 2008.
- [8] C. Caloz, D. R. Jackson, and T. Itoh, "Leaky-wave antennas," in *Frontiers in Antennas: Next Generation Design Engineering*. New York: McGraw-Hill, Dec. 2011.
- [9] W. W. Hansen, "Radiating electromagnetic waveguide," U.S. Patent No. 2, 402, 622, 1940.
- [10] J. N. Hines and J. R. Upson, "A wide aperture tapered-depth scanning antenna," Ohio State Univ. Res. Found. p. 667, 1957.
- [11] A. Hessel, "General characteristics of traveling-wave antennas", in *Antenna Theory*, R. E. Collin and F. J. Zucker, Eds. New York: McGraw-Hill, pt. 2, ch. 19, 1969.
- [12] G. Lovat, P. Burghignoli, and D. R. Jackson, "Fundamental properties and optimization of broadside radiation from uniform leaky-wave antennas," *IEEE Trans. Antennas Propag.*, vol. 54, no. 5, pp. 1442–1452, May 2006.
- [13] P. Burghignoli, G. Lovat, and D. R. Jackson, "Analysis and optimization of leaky-wave radiation at broadside from a class of 1-D periodic structures," *IEEE Trans. Antennas Propag.*, vol. 54, no. 9, pp. 2593–2603, Sep. 2006.
- [14] A. A. Oliner and A. Hessel, "Guided waves on sinusoidally-modulated reactance surfaces," *IRE Trans. Antennas Propag.*, vol. 7, no. 5, pp. 201–208, Dec. 1959.

- [15] N. G. Alexopoulos and D. R. Jackson, "Fundamental superstrate (cover) effects on printed circuit antennas," *IEEE Trans. Antennas Propagat.*, vol. AP-32, pp. 807-816, Aug. 1984.
- [16] D. R. Jackson and N. G. Alexopoulos, "Gain enhancement methods for printed circuit antennas", *IEEE Trans. Antennas Propag.*, vol. AP-33, no. 9, pp. 976-987, Sep. 1985.
- [17] D. R. Jackson et al., "The fundamental physics of directive beaming at microwave and optical frequencies and the role of leaky waves," *Proc. IEEE*, vol. 99, no. 10, pp. 1780-1805, Oct. 2011.
- [18] N. Engheta and R. W. Ziolkowski, *Electromagnetic Metamaterials: Physics and Engineering Explorations*. New York, NY, USA: Wiley-IEEE, 2006.
- [19] A. V. Kildishev, A. Boltasseva, and V. M. Shalaev, "Planar photonics with metasurfaces," *Science*, vol. 339, no. 6125, p. 1232009, Mar. 2013.
- [20] N. Yu and F. Capasso, "Flat optics with designer metasurfaces," *Nat. Mater.*, vol. 13, no. 2, pp. 139-150, Feb. 2014.
- [21] D. Sievenpiper, R. F. J. Broas, N. G. Alexopoulos, and E. Yablonovitch, "High-impedance electromagnetic surfaces with a forbidden frequency band," *IEEE Trans. Microw. Theory Tech.*, vol. 47, no. 11, pp. 2059-2074, 1999.
- [22] J. Huang and J. A. Encinar, *Reflectarray antennas*. Hoboken, NJ: Wiley, 2008.
- [23] D. Sievenpiper, J. Schaffner, J. J. Lee, and S. Livingston, "A steerable leaky-wave antenna using a tunable impedance ground plane," *IEEE Antennas Wireless Propag. Lett.*, vol. 1, no. 1, pp. 179-182, 2002.

- [24] D. F. Sievenpiper, "Forward and backward leaky-wave radiation with large effective aperture from an electronically tunable textured surface," *IEEE Trans. Antennas Propag.*, vol. 53, no. 1, pp. 236–247, Jan. 2005.
- [25] M. Mavridou, K. Konstantinidis, and A. Feresidis, "Continuously tunable mm-wave high impedance surface," *IEEE Antennas Wireless Propag. Lett.* 15, 1390–1393, 2015.
- [26] M. Mavridou and A. P. Feresidis, "Dynamically reconfigurable high impedance and frequency selective metasurfaces using piezoelectric actuators," *IEEE Trans. Antennas Propag.*, vol. 64, no. 12, pp. 5190–5197, Dec. 2016.
- [27] D. Sievenpiper, J. Colburn, B. Fong, J. Ottusch, and J. Visher, "Holographic artificial impedance surfaces for conformal antennas," in *Proc. IEEE Antennas Propag. Soc. Int. Symp.*, 2005, vol. 1B, pp. 256–259.
- [28] A. Sutinjo, M. Okoniewski, and R. H. Johnston, "A holographic antenna approach for surface wave control in microstrip antenna applications," *IEEE Trans. Antennas Propag.*, vol. 58, no. 3, pp. 675–682, Mar. 2010.
- [29] B. H. Fong, J. S. Colburn, J. J. Ottusch, J. L. Visher, and D. F. Sievenpiper, "Scalar and tensor holographic artificial impedance surfaces," *IEEE Trans. Antennas Propag.*, vol. 58, no. 10, pp. 3212–3221, Oct. 2010.
- [30] G. von Trentini, "Partially reflecting sheet arrays," *IEEE Trans. Antennas Propag.*, vol. AP-4, no. 4, pp. 666–671, Oct. 1956.

- [31] A. P. Feresidis, J. C. Vardaxoglou, "High gain planar antenna using optimised partially reflective surfaces," *Inst. Electr. Eng. Proc.-Microw. Antennas Propag.*, vol. 148, pp. 345–350, Dec. 2001.
- [32] A.P. Feresidis, J.C. Vardaxoglou, "High gain planar antenna using optimised partially reflective surfaces," *IET Microw. Antennas Propag.*, 148, (6), pp. 345–350,2001.
- [33] G. Mateo-Segura, G. Goussetis, and A. P. Feresidis, "Subwavelength profile 2-D leaky-wave antennas with two periodic layers," *IEEE Trans. Antennas Propag.*, vol. 59, no. 2, pp. 416– 424, Feb. 2011.
- [34] K. Konstantinidis, A.P. Feresidis, and P.S. Hall, "Multilayer partially reflective surfaces for broadband Fabry-Perot cavity antennas," *IEEE Trans. Antennas Propag.*, 2014, 62, (7), pp. 3474–3481.
- [35] K. Konstantinidis, A. P. Feresidis and P. S. Hall, "Broadband Sub-Wavelength Profile High-Gain Antennas Based on Multi-Layer Metasurfaces," in *IEEE Transactions on Antennas and Propagation*, vol. 63, no. 1, pp. 423-427, Jan. 2015.
- [36] P. Kosmas, A. P. Feresidis, and G. Goussetis, "Periodic FDTD analysis of a 2-D leaky-wave planar antenna based on dipole frequency selective surfaces," *IEEE Trans. Antennas Propag.*, vol. 55, no. 7, pp. 2006–2012, Jul. 2007.
- [37] C. Mateo-Segura, M. Garcia-Vigueras, G. Goussetis, A. P. Feresidis, and J. L. Gomez-Tornero, "A simple technique for the dispersion analysis of Fabry-Perot cavity leaky-wave antennas," *IEEE Trans. Antennas Propag.*, vol. 60, no. 2, pp. 803–810, Feb. 2012.

- [38] C. Caloz, H. Okabe, T. Iwai, and T. Itoh, "Transmission line approach of left-handed (LH) materials," in *Proc. USNC/URSI Nat. Radio Sci. Meet.*, San Antonio, TX, USA, Jun. 16–21, 2002, vol. 1, p. 39.
- [39] A. Grbic and G. V. Eleftheriades, "A backward-wave antenna based on negative refractive index L-C networks," in *Proc. IEEE Intl. Symp. Antennas Propag.*, San Antonio, TX, USA, Jun. 16–21, 2002, vol. 4, pp. 340–343.
- [40] A. A. Oliner, "A periodic-structure negative refractive-index medium without resonant elements," in *Proc. USNC/URSI Nat. Radio Sci. Meet.*, San Antonio, TX, USA, Jun. 16–21, 2002, p. 41.
- [41] D. R. Jackson, C. Caloz, and T. Itoh, "Leaky-wave antennas," *Proc. IEEE*, vol. 100, no. 7, pp. 2194–2206, Jul. 2012.
- [42] C. Caloz, T. Itoh, and A. Rennings, "CRLH metamaterial leaky-wave and resonant antennas," *IEEE Antennas Propag. Mag.*, vol. 50, no. 5, pp. 25–39, Oct. 2008.
- [43] J. S. Gomez-Diaz, D. Canete-Rebenaque, and A. Alvarez-Melcon, "A simple CRLH LWA circuit condition for constant radiation rate," *IEEE Antennas Wireless Propag. Lett.*, vol. 10, pp. 29–32, 2011.
- [44] C. Caloz and T. Itoh, "Metamaterial-based electronically controlled transmission-line structure as a novel leaky-wave antenna with tunable radiation angle and beamwidth", *IEEE Trans. Microw. Theory Tech.*, vol. 53, no. 1, pp. 161–173, Jan. 2005.

- [45] T. Thio, K. M. Pellerin, R. A. Linke, H. J. Lezec, and T. W. Ebbesen, "Enhanced light transmission through a single subwavelength aperture", *Opt. Lett.*, vol. 26, pp. 1972–1974, 2001.
- [46] H. J. Lezec et al., "Beaming light from a subwavelength aperture," *Science*, vol. 297, no. 5582, pp. 820–822, Aug. 2002.
- [47] H. Bethe, "Theory of diffraction by small holes," *Phys. Rev.*, vol. 66, no. 7-8, pp. 163-182, Oct. 1944.
- [48] F. J. García-Vidal, H. J. Lezec, T. W. Ebbesen, and L. Martín-Moreno, "Multiple Paths to Enhance Optical Transmission through a Single Subwavelength Slit," *Phys. Rev. Lett.* 90(21), 213901 (2003).
- [49] T. W. Ebbesen, H. J. Lezec, H. F. Ghaemi, T. Thio, and P. A. Wolff, "Extraordinary optical transmission through sub-wavelength hole arrays," *Nature*, vol. 391, no. 6668, pp. 667–669, Feb. 1998.
- [50] L. Martin-Moreno, F. J. Garcia-Vidal, H. J. Lezec, K. M. Pellerin, T. Thio, J. B. Pendry, and T. W. Ebbesen, "Theory of extraordinary optical transmission through subwavelength hole arrays," *Phys. Rev. Lett.*, vol. 86, pp. 1114–1117, 2001.
- [51] C. Genet and T. W. Ebbesen, "Light in tiny holes", *Nature*, vol. 445, pp. 39–46, 2007.
- [52] M. Beruete, M. Sorolla, I. Campillo, J. S. Dolado, L. Martin-Moreno, J. Bravo-Abad, and F. J. García-Vidal, "Enhanced millimeter wave transmission through quasioptical subwavelength perforated plates," *IEEE Trans. Antennas Propag.*, vol. 53, no. 6, pp. 1897–1903, Jun. 2005.

- [53] M. Beruete, M. Sorolla, M. N. Cia, F. Falcone, I. Campillo, and V. Lomakin, "Extraordinary transmission and left-handed propagation in miniaturized stacks of doubly periodic subwavelength hole arrays", *Opt. Exp.*, vol. 15, no. 3, pp. 1107–1114, 2007.
- [54] A. D. Rakic, A. B. Djuricic, J. M. Elazar, and M. L. Majewski, "Optical properties of metallic films for vertical-cavity optoelectronic devices," *Appl. Opt.*, vol. 37, no. 22, pp. 5271–5283, 1998.
- [55] S. A. Maier, *Plasmonics: Fundamentals and Applications*. Berlin, Germany: Springer, 2007.
- [56] A. A. Oliner and D. R. Jackson, "Leaky surface-plasmon theory for dramatically enhanced transmission through a subwavelength aperture, Part I: Basic features," in *Proc. IEEE AP-S Symp. Radio Sci. Meet.*, Columbus, OH, USA, 2003, vol. 2, pp. 1091–1094.
- [57] D. R. Jackson, T. Zhao, J. T. Williams, and A. A. Oliner, "Leaky surface-plasmon theory for dramatically enhanced transmission through a sub-wavelength aperture, II: Leaky-wave antenna model," in *Proc. IEEE AP-S Symp. Radio Sci. Meet.*, Columbus, OH, USA, 2003, vol. 2, pp. 1095–1098.
- [58] D. R. Jackson, A. A. Oliner, T. Zhao and J. T. Williams, "Beaming of light at broadside through a subwavelength hole: Leaky wave model and open stopband effect," in *Radio Science*, vol. 40, no. 06, pp. 1-12, Dec. 2005.
- [59] D. R. Jackson, J. Chen, R. Qiang, F. Capolino, and A. A. Oliner, "The role of leaky plasmon waves in the directive beaming of light through a subwavelength aperture", *Opt. Exp.*, vol. 16, no. 26, pp. 21271–21281, Dec. 22, 2008.

- [60] J.A. Porto, F.J. Garcia-Vidal, J.B. Pendry, "Transmission resonances on metallic gratings with very narrow slits", *Phys. Rev. Lett.* 83, 2845-2848, 1999.
- [61] M. Beruete, I. Campillo, et.al. "Very low profile "Bull's Eye" feeder antenna", *IEEE Antennas Wireless Propag. Lett.*, vol. 4, pp. 365–368, 2005.
- [62] M. Beruete et al., "Terahertz corrugated and Bull's-Eye antennas," *IEEE Trans. Terahertz Sci. Technol.*, vol. 3, no. 6, pp. 740–747, Nov. 2013.
- [63] H. Lu, X. Lv, Z. Gao, Y. Liu, "Experimental radiation characteristics of micromachined terahertz low-profile corrugated horn antenna", *Microw. Opt. Technol. Lett.* 57, pp. 364–367 (2015).
- [64] U. Beaskoetxea and M. Beruete, "High aperture efficiency wide corrugations bull's-eye antenna working at 60 GHz," *IEEE Trans. Antennas Propag.*, vol. 65, no. 6, pp. 3226–3230, 2017.
- [65] U. Beaskoetxea et al., "77-GHz high-gain bull's-eye antenna with sinusoidal profile," *IEEE Antennas Wireless Propag. Lett.*, vol. 14, pp. 205–208, 2015.
- [66] U. Beaskoetxea, S. Maci, M. Navarro-Cia, and M. Beruete, "3-D-printed 96 GHz bull's-eye antenna with off-axis beaming," *IEEE Trans. Antennas Propag.*, vol. 65, no. 1, pp. 17–25, Jan. 2017
- [67] M. Beruete, I. Campillo, J. S. Dolado, J. E. Rodríguez-Seco, E. Perea, F. Falcone, and M. Sorolla, "Dual-band low-profile corrugated feeder antenna," *IEEE Trans. Antennas Propag.*, vol. 54, no. 2, pp. 340–350, Feb. 2006.

- [68] C. J. Vourch and T. D. Drysdale, "V-Band "Bull's Eye" Antenna for CubeSat Applications", *Antennas Wireless Propagation Letters*, vol. 13, 1092–1095, 2014.
- [69] P. Baccarelli, P. Burghignoli, G. Lovat, S. Paulotto, "A novel printed leaky-wave "bull-eye" antenna with suppressed surface-wave excitation," *IEEE Antennas and Propagation Society Symposium*, 2004. IEEE (2004), pp. 1078–1081.
- [70] S. K. Podilchak, P. Baccarelli, P. Burghignoli, A. P. Freundorfer, and Y. M. M. Antar, "Optimization of a planar "bull-eye" leaky-wave antenna fed by a printed surface-wave source," *IEEE Antennas and Wireless Propag. Lett.*, vol. 12, pp. 665–669, 2013.
- [71] S.K. Podilchak, P. Baccarelli, P. Burghignoli, A.P. Freundorfer, Y.M.M. Antar, "Analysis and design of annular microstrip-based planar periodic leaky-wave antennas", *IEEE Trans. Antennas Propag.* 62, 2978–2991,2014.
- [72] C. J. Vourch and T. D. Drysdale, "Directivity enhancement of V-band "Bull's eye" antenna with dielectric superstrate," *2014 Loughborough Antennas and Propagation Conference (LAPC)*, Loughborough, 2014, pp. 277–280.
- [73] S. Krishna, S.D. Gunapala, S.V. Bandara, C. Hill, D.Z. Ting, "Quantum dot based infrared focal plane arrays". *Proc. IEEE* 95, 1838–1852 (2007).
- [74] J.J. Greffet, R. Carminati, K. Joulain, J.P. Mulet, M. Stéphane, Y. Chen, "Coherent emission of light by thermal sources". *Lett. Nat.*, 416, 61–64 (2002).
- [75] T. Xu, Y.-K. Wu, X. Luo, L.J. Guo, "Plasmonic nanoresonators for high-resolution colour filtering and spectral imaging". *Nat. Commun.* 1, 59 (2010).

- [76] R.E. Collin, "Field Theory of Guided Waves", *New York: Wiley-Interscience*, 2001, ch.4.
- [77] R. E. Collin, "Foundations for Microwave Engineering", 2nd ed. *New York: McGraw-Hill*, 1992, ch. 8.
- [78] A. Sutinjo and M. Okoniewski, "A Simple Leaky-Wave Analysis of 1-D Grooved Metal Structure for Enhanced Microwave Radiation", *IEEE Transactions on Antennas and Propagation*, vol. 60, no. 6, pp. 2719-2726, June 2012.

Chapter 2

Theoretical Background

This chapter presents the theoretical background of the dissertation. The fundamentals of leaky wave physics and mathematic formulations are reported. These include the Floquet theory for one-dimensional periodic leaky wave antennas, the explanation of the basic properties of leaky wave antennas, and an array factor approach of the derivation of the far field patterns of such antennas. Section 2.2 describes a Finite-Difference Time-Domain (FDTD) dispersion analysis tool for a periodic structure terminated with periodic boundary conditions. This tool is implemented in the following Chapters on both novel and classic corrugated antenna designs. The matrix pencil method is briefly described in Section 2.3 for the approximation of the near field of an antenna by a sum of complex exponentials. The final Sections demonstrate the mathematical formalism of periodically corrugated metallic surfaces, along with design configurations for optimum transmission of power from such structures. An analytical dispersion analysis methodology for corrugated surfaces with narrow gaps is described, which inspires a novel algorithm to be presented in Chapter 3 for the leaky wave analysis of corrugated metallic surfaces with large gaps.

2.1 Fundamentals of Leaky Waves

Leaky wave antennas belong to a class of antennas that support a travelling wave on the guiding structure as the main radiating mechanism. The travelling wave is characterized by a complex longitudinal wavenumber $k_y = \beta - j\alpha$, where β is the propagation or phase constant and α is the attenuation constant, or leakage rate (Fig. 2.1). The leaky wave propagates (leaks) on the guiding structure, in contrast to slow-type antennas which are characterized by a surface wave that does not radiate until it reaches the end of the structure [1].

An infinite guiding structure on the xy plane is considered (Fig. 2.1), with the feeding source at the one end ($z = 0$) of the structure (unidirectional case). The structure supports a wave with a complex longitudinal wavenumber $k_y = \beta - j\alpha$. It is further assumed that the electromagnetic problem is invariant along x . The electric field distribution form on the structure is assumed as

$$E_x(y, 0) = Ce^{-jk_y y} \quad (2.1)$$

where C is a constant. The attenuation constant α refers to losses due to leakage of power along the structure, however if dielectric or conductor losses are present, then these losses must be included in the attenuation constant as well.

In the air region above the structure ($z > 0$), the electric field takes the form of

$$E_x(y, z) = Ce^{-jk_y y} e^{-jk_z z} \quad (2.2)$$

with the vertical wavenumber of the propagating wave k_z related to the longitudinal wavenumber k_y as

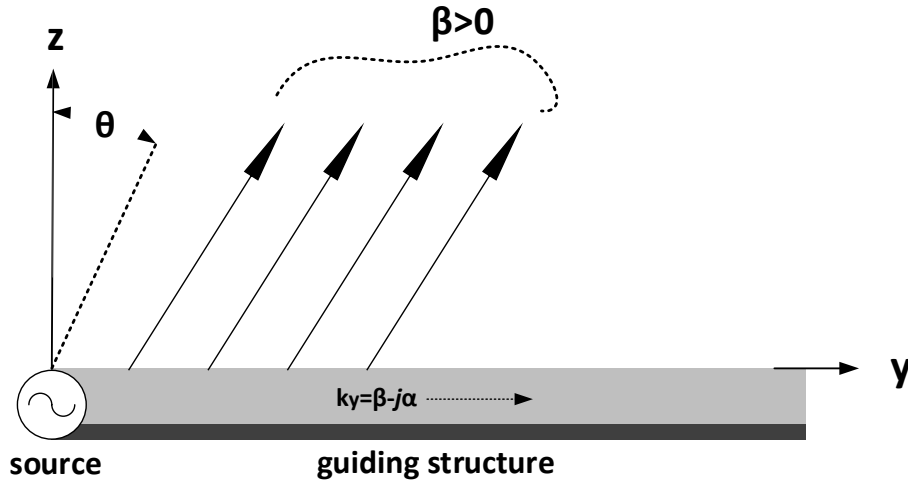


Figure 2.1: A unidirectional leaky wave antenna of infinite size on the xy plane.

$$k_z = \pm \sqrt{k_0^2 - k_y^2} = \beta_z - j\alpha_z \quad (2.3)$$

where k_0 is the free space wavenumber. As the structure is passive, for the leaky wave it is compulsory that $\alpha > 0$, meaning that the leaky wave should decay in the longitudinal y direction.

The nature of the wave propagation can be determined by the values of the phase constant β . When $|\beta| > k_0$, then the wave supported on the guiding structure is a surface wave, which does not radiate unless it reaches the end of the structure. Equivalently, the group velocity v_g is related to the speed of light c as $v_g < c$, which justifies the characterization of surface waves as *slow waves*. When $|\beta| < k_0$ (or $v_g > c$), the leaky wave phenomenon takes effect. A surface wave converts into a travelling (fast) wave as it propagates across the longitudinal direction of the structure. This wave is characterized as *leaky wave*.

When $0 < \beta < k_0$, the phase propagation is characterized as forward, flowing in the same direction as the power flow, therefore the leaky wave is classified as *forward* (as

in Fig. 2.1). The emerging main beam points at an angle θ_0 between 0° and 90° , with respect to the z axis. From (2.3) it is determined that $\alpha_z < 0$, which means that the wave in the air region is exponentially increasing (improper leaky wave). This initially looks like a paradox, since it violates the radiation condition at infinity for the Helmholtz equation. The explanation of this phenomenon lies in the fact that these findings refer to infinite size leaky wave antennas. In reality, a finite size leaky wave antenna launches a leaky mode that increases exponentially towards the z direction up to a boundary, and then decreases above this boundary.

In the case of $-k_0 < \beta < 0$ the leaky mode is characterized as *backward*, meaning that the phase constant and the power flow in opposite directions. The main beam scans between the angles -90° and 0° . In (2.3) it is indicated that $\alpha_z > 0$, thus the leaky wave decays properly towards infinity (proper leaky wave).

The exact numerical values of β and α of the longitudinal wavenumber k_y can determine the far field behaviour of most practical 1D leaky wave antennas. If the attenuation constant α is small and the structure can be considered sufficiently long, then β controls the radiation angle θ measured from $z = 0$ as

$$\theta = \sin^{-1} \frac{\beta}{k_0} \quad (2.4)$$

Eq. (2.4) demonstrates the beam-scanning capabilities of leaky wave antennas as a variation of phase constant with frequency. It is also evident that a unidirectional leaky-wave antenna can't scan too close to broadside, as for radiation at $\theta \approx 0$ an operation close to the cutoff frequency of the waveguide would be needed. This is an inherent problem of most unidirectional leaky wave antennas fed by a single source at their end.

The angular width of the main beam ABW pointing at an angle θ in the farfield is determined by the values the attenuation constant α with the approximate formula measured between half-power points as

$$ABW = 2csc(\theta) \frac{\alpha}{k_0} \quad (2.5)$$

A small attenuation constant α implies a narrow directive beam at the farfield (increased directivity), when the antenna is considered long enough. When α is fixed to a certain value, then the total length L of the unidirectional leaky wave antenna can be calculated, for a typically selected 90% transmission of radiated power

$$\frac{L}{\lambda_0} = \frac{0.18}{\alpha/k_0} \quad (2.6)$$

where λ_0 is the wavelength in free space. The formula (2.6), along with (2.4) and (2.5) can provide a rough estimation guide for the design of the practical leaky wave antennas, with respect to their scanning angle, beamwidth and size.

2.1.1 One-Dimensional Periodic Leaky Wave Antennas

A special class of leaky wave antennas are the one dimensional (1D) antennas which are periodically modulated with period d in the longitudinal y direction (Fig. 2.2). Such periodic structures can be studied with Floquet theory, by considering the formation of a Bloch wave while it propagates on the periodic structure [2].

Let's consider a Bloch wave with complex longitudinal wavenumber $k_y = \beta + j\alpha$ while it propagates on a periodic structure. The vector field values (\mathbf{E} , \mathbf{H}) of this wave



Figure 2.2: One-dimensional periodic leaky wave antenna.

have exactly the same values at every point of each unit cell except for an exponential propagation factor $e^{-k_y d}$. Therefore, within a unit cell $0 < y < d$ the values of the electric and magnetic field can be written as [2, 3]

$$\begin{aligned}\mathbf{E}(x, y, z) &= e^{-k_y d} \mathbf{E}_p(x, y, z) \\ \mathbf{H}(x, y, z) &= e^{-k_y d} \mathbf{H}_p(x, y, z)\end{aligned}\tag{2.7}$$

where the vectors \mathbf{E}_p and \mathbf{H}_p are periodic functions of y with period d

$$\begin{aligned}\mathbf{E}_p(x, y + kd, z) &= \mathbf{E}_p(x, y, z) \\ \mathbf{H}_p(x, y + kd, z) &= \mathbf{H}_p(x, y, z)\end{aligned}\tag{2.8}$$

where k is an integer. This expression of fields in a periodic structure is often referred to as *Floquet theorem*.

In addition, any periodic function of \mathbf{E}_p , \mathbf{H}_p , can be expanded into infinite Fourier series as

$$\begin{aligned}\mathbf{E}_p(x, y, z) &= \sum_{k=-\infty}^{\infty} \mathbf{E}_{pk}(x, z) e^{-j 2 k \pi y/d} dy \\ \mathbf{H}_p(x, y, z) &= \sum_{k=-\infty}^{\infty} \mathbf{H}_{pk}(x, z) e^{-j 2 k \pi y/d} dy\end{aligned}\tag{2.9}$$

where \mathbf{E}_{pk} , \mathbf{H}_{pk} are vector functions of x and z . Integration within the boundaries of a

unit cell $0 \leq y \leq d$ gives

$$\begin{aligned}\mathbf{E}_{pm}(x, z) &= \frac{1}{d} \int_0^d \mathbf{E}_p(x, y, z) e^{-j 2 m \pi y/d} dy \\ \mathbf{H}_{pm}(x, z) &= \frac{1}{d} \int_0^d \mathbf{H}_p(x, y, z) e^{-j 2 m \pi y/d} dy\end{aligned}\tag{2.10}$$

with m an integer, which leads to the expression for the field in the periodic structure

$$\begin{aligned}\mathbf{E}(x, y, z) &= \int_{k=-\infty}^{\infty} \mathbf{E}_{pk}(x, z) e^{-\alpha y - j(\beta + 2k\pi/d)} dy \\ \mathbf{H}(x, y, z) &= \int_{k=-\infty}^{\infty} \mathbf{H}_{pk}(x, z) e^{-\alpha y - j(\beta + 2k\pi/d)} dy\end{aligned}\tag{2.11}$$

where the phase constant can be written as $\beta_k = \beta + 2k\pi/d$. Each term in this expansion is called a *space harmonic*. While the propagation constant β consists of an infinite number of space harmonics, the attenuation constant α is the same for the harmonics of the Bloch wave.

The longitudinal complex wavenumber of the guided mode can therefore be written as a sum of infinite n space harmonics according to [1]

$$k_{y,n} = k_{y,0} + 2\pi n/d\tag{2.12}$$

where $k_{y,0}$ is the wavenumber of the fundamental Floquet mode. The fundamental Floquet mode $k_{y,0}$ is a slow wave, however one of the space harmonics (usually the $n = -1$) is designed to be a fast (leaky) wave. In some practical implementations, higher order harmonics may be engineered to radiate efficiently with significant contribution to the overall antenna radiation.

2.1.2 The Problem of Radiation at Broadside

The problem of leaky wave radiation at broadside ($\theta = 0$) has been a traditional problem for unidirectional 1-D leaky wave antennas, uniform and periodic. From the standard leaky wave formula (2.4), the beam cannot be scanned too close to broadside, since radiation is subject to limitations from the pattern of the feeding source (e.g. operation close to the cut-off of the waveguide).

The problem of broadside radiation in periodic leaky wave antennas is associated with the presence of an open stopband at the immediate vicinity of $\theta = 0$. For a fundamentally slow leaky wave antenna, this is encountered when the phase constant of the fast space harmonic is zero, but then, equally, the attenuation constant drops to zero as well. This results in a severe degradation when the antenna radiates at broadside [5].

The incapability of broadside radiation of uniform 1D or 2D unidirectional leaky wave antennas has been discussed in [3]. For a 1D periodic leaky wave structure it has been found in [4] that a main beam pointing at $\theta = 0$ is achievable by symmetrically feeding the antenna with a source in the middle of the structure, or with two sources at both ends, with the first realization being the most popular (Fig. 2.3). The bidirectional antenna produces two conical beams, pointing at angles $\pm\theta$.

For a 1D bidirectional infinite size (uniform or periodic) leaky wave antenna with complex wavenumber $k_y = \beta - j\alpha$, the optimum condition to obtain maximum power density radiated at broadside is $|\beta| = \alpha$. This is also the beam-splitting condition between two maxima off broadside for the radiation pattern of the antenna. Moreover, the two conical beams merge into a single beam pointing at broadside when $|\beta| < \alpha$ (or $|\beta_n| < \alpha$ for the case of a periodic antenna). Whenever $|\beta| > \alpha$, a split beam radiation pattern

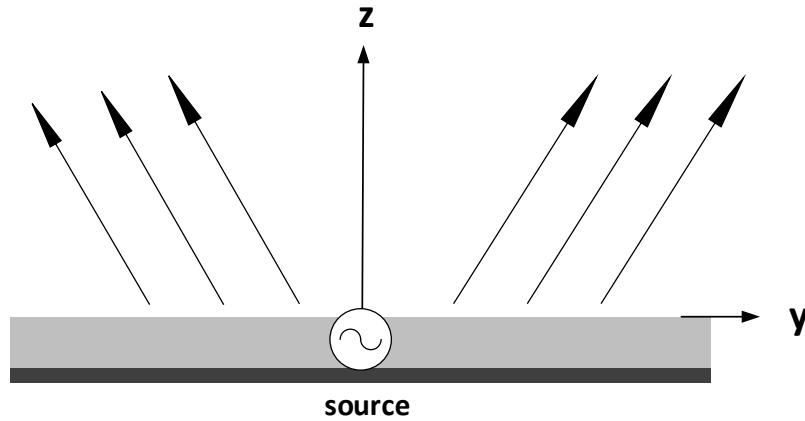


Figure 2.3: Bidirectional (symmetrically-fed) leaky wave antenna.

is expected, with each beam deriving from the corresponding half of the structure. For a finite size leaky wave antenna, this beam-splitting condition can be further relaxed to $|\beta| < n_s \alpha$, where n_s is a constant related to the percentage of power radiated by the finite structure [5]. Radiation at broadside is possible, by operating close to the open stopband frequency (where $\beta \approx 0$). In this case, the beams emerging from each half of the structure are combined into a symmetrical broadside beam.

These findings can also apply to 2D bidirectional leaky wave antennas with homogeneous or quasi-homogeneous geometry, which can produce a directive pencil beam at broadside, given that $|\beta| = \alpha$ [4].

2.1.3 Array Factor Approach

The farfield radiation characteristics of a leaky wave antenna can be approximately calculated via an array factor approach (Fig. 2.4). If the antenna can be considered as an array of radiating elements, then the array factor is a function of antenna element geometry and their excitation phase. From known antenna theory [6] the total radiation pattern can be found by multiplying the array factor by the element factor (the pattern produced

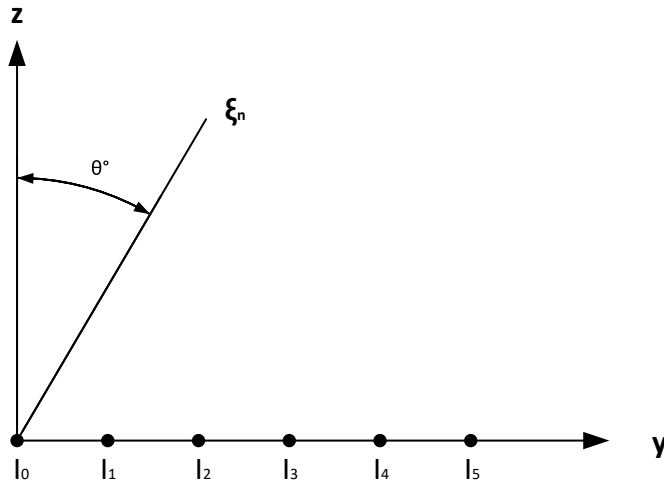


Figure 2.4: Array factor of a unidirectional leaky wave antenna.

by a single element of the array).

A leaky wave antenna with a longitudinal complex wavenumber $k_{y,n} = \beta_n - j\alpha$ can be approached as a phased array antenna with a periodic spacing d of m elements very closely spaced to $d \rightarrow 0$. Each element is fed discretely by a phase function $\xi_m(\theta_0)$, where θ_0 is the radiation angle, and an exponential magnitude function $I(y) = I_0 e^{-\alpha y}$. The radiation angle θ_0 is calculated by (2.4). Only the n^{th} fast space harmonic of the propagation constant is considered for the analysis below.

When the medium can be considered effective, then the condition $d \rightarrow 0$ is satisfied. The phase and magnitude functions can then be discretized as [7]

$$\begin{aligned} \xi_m &= -(m-1) k_0 d \sin \theta_0 \\ I_n &= I_0 e^{-\alpha(m-1)d} \end{aligned} \tag{2.13}$$

where k_0 is the free space wavenumber. Since $d \rightarrow 0$, each element can be considered an isotropic radiator, therefore the total radiation pattern $R(\theta)$ of the leaky wave antenna can be approximated by a array factor function

$$R(\theta) = AF(\theta) = \sum_{m=1}^M I_0 e^{j(m-1)k_0 d \sin\theta + j\xi_m} \quad (2.14)$$

where M is the total number of periodically spaced elements in the one-dimensional antenna.

For a two-dimensional antenna in the xy plane, the total radiation pattern is determined by the radiation angle θ in each azimuth direction ϕ as

$$R(\theta, \phi) = AF(\theta, \phi) = \left[\sum_{m=1}^M I_{m1} e^{j(m-1)k_0 d_y \sin\theta \cos\phi + j\xi_{y,m}} \right] \left[\sum_{l=1}^L I_{l1} e^{j l k_0 d_x \sin\theta \sin\phi + j\xi_{x,l}} \right] \quad (2.15)$$

where d_y , d_x are the periods of a total of M and L spaced elements along the y and x directions accordingly.

2.2 Periodic Full-Wave Analysis

In this Section, a rigorous full-wave periodic analysis tool is described for the dispersion characterisation of a periodic structure. The method was first introduced in [10], [13] based on a Finite-Difference Time-Domain (FDTD) analysis of the unit cell and proposes the implementation of periodic boundary conditions in the time-domain. However, other full-wave techniques for simulating the unit cell can be employed together with this method. Here, a brief overview of the method is given and its application on several antenna designs is presented in the following Chapters.

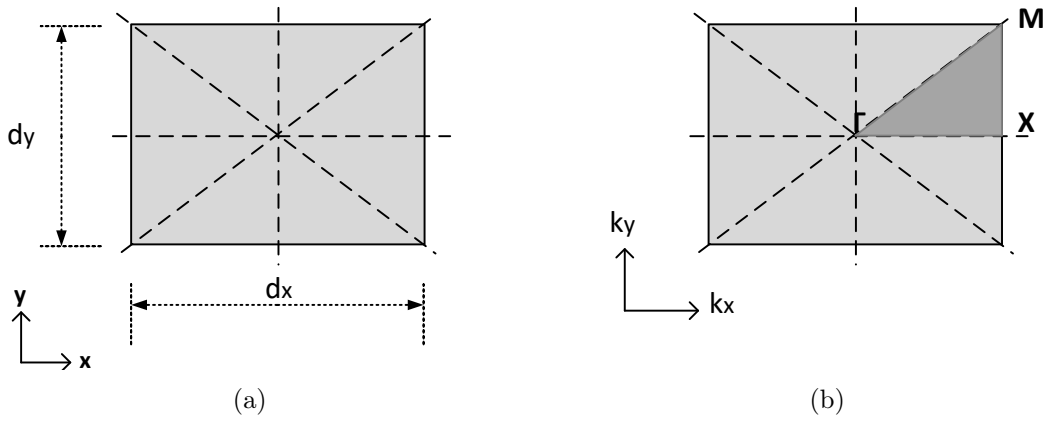


Figure 2.5: A periodic unit cell (a) 2-D lattice (b) corresponding Brillouin zone.

A 2-D periodic structure (unit cell) of periodicities d_x and d_y is considered, along x and y respectively (Fig. 2.5.a). Periodic boundary conditions (PBCs) are employed across the x and y boundaries of the unit cells, achieving a reasonable computational time. The electromagnetic field components are tracked at sample points spaced a period apart, and differ only by an exponential term $e^{-jk_x d_x}$, $e^{-jk_y d_y}$, where $k_x = \beta_x \tilde{x} + \alpha_x \tilde{y}$ and $k_y = \beta_y \tilde{x} + \alpha_y \tilde{y}$ are the corresponding complex wavenumbers across x, y [10, 12].

The lattice vector can be determined as $\bar{p} = d_x \tilde{x} + d_y \tilde{y}$ and the lattice wave vector is $\bar{k}_p = k_x \tilde{x} + k_y \tilde{y}$. Floquet's conditions on electric and magnetic field phasors $\tilde{\vec{E}}$ and $\tilde{\vec{H}}$ can be written as

$$\begin{aligned}\tilde{\vec{E}}(\bar{r} + \bar{p}) &= \tilde{\vec{E}}(\bar{r}) e^{-j \bar{k}_p \bar{p}} \\ \tilde{\vec{H}}(\bar{r} + \bar{p}) &= \tilde{\vec{H}}(\bar{r}) e^{-j \bar{k}_p \bar{p}}\end{aligned}\tag{2.16}$$

where \bar{r} is the radial vector. The transformation of (2.16) from the frequency domain to the time domain is then derived as

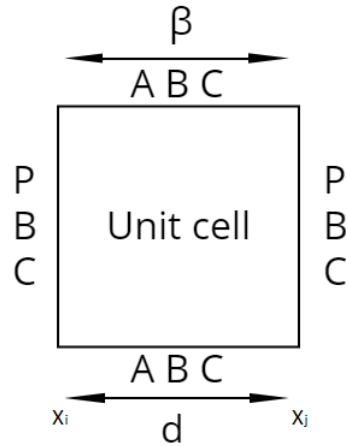


Figure 2.6: Setup of field sampling points for the calculation of the complex wavenumber.

$$\begin{aligned}\overline{E}_s(\bar{r} + \bar{p}, t) &= \overline{E}_s(\bar{r}, t)\cos(\bar{k}_p \bar{p}) - \overline{E}_c(\bar{r}, t)\sin(\bar{k}_p \bar{p}) \\ \overline{E}_c(\bar{r} + \bar{p}, t) &= \overline{E}_s(\bar{r}, t)\sin(\bar{k}_p \bar{p}) + \overline{E}_c(\bar{r}, t)\cos(\bar{k}_p \bar{p})\end{aligned}\quad (2.17)$$

The complex propagation constants k_x and k_y correspond to a point on the $\Gamma - X - X - M - X - \Gamma$ axis of the Brillouin diagram (Fig. 2.5.b). For each such point, the time-domain waveforms of fields are sampled within the unit cells. Therefore, the resonances that represent the modal frequencies $\omega(k_x, k_y)$ are revealed by the Fourier transform of these waveforms from the time domain to the frequency domain.

The above analysis is usually implemented for the extraction of the phase constant β of a unit cell, by assuming the above wavenumbers k_x and k_y as real [10]. If the structure exhibits leaky wave behaviour, there is the need to calculate the attenuation constant α as well.

For this purpose, a unit cell of the structure is considered terminated with PBCs (Fig. 2.6) and absorbing boundary conditions (ABCs) for the calculation of the complex wavenumber. The phase constant β is the longitudinal x component of the leaky mode. If $w(t, x)$ is the waveform of an E - or H - component sampled at two chosen points x_i

and x_j along the axis of periodicity, then the complex propagation constant $k = k_x$ can be calculated as

$$k(\omega) = j \frac{1}{x_j - x_i} \ln \frac{\mathcal{F}[w(t, x_i)]}{\mathcal{F}[w(t, x_j)]} \quad (2.18)$$

where \mathcal{F} stands for a Fourier transform. The imaginary part of (2.18) is the attenuation constant of the leaky mode [13].

The effective complex propagation constant within a unit cell can be determined by fixing the distance between the selected sample points x_i and x_j in (2.18) as close to one period d as possible. The periodicity of the unit cell along x can be denoted as Δx . Then, the maximum distance between two nonboundary sample points within the domain of one unit cell is equal to $d - 2\Delta x$. This distance tends to d as the unit cell size Δx tends to zero.

A more popular alternative approach is the extension of the computational FDTD domain to include two unit cells as in Fig. 2.7. A double phase difference 2β per unit cell is imposed at the x - periodic boundaries boundaries, due to the fact that the wave travels twice the distance. The previously discussed problem of locating the sample points within the limited space of one unit cell is tackled by choosing the two points exactly one period apart. With this approach, a significant reduction in the computational time is achieved, while maintaining the accuracy.

The major disadvantage of this method for the calculation of α is the failure of the methodology when large values of the leakage rate are expected. This is due to the large and fast spatial decay of the propagating signal and the fact that two spatial samples that are spaced a period apart are required for the calculation of the complex wavenumber. It has been reported that for normalized values of leakage rate to free space wavenumber up

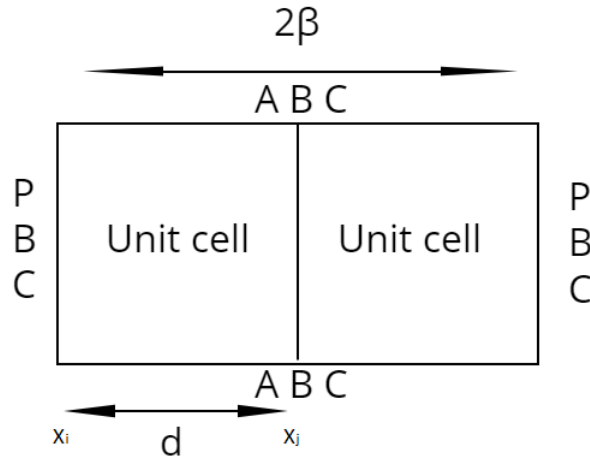


Figure 2.7: Alternative setup of field sampling points for the calculation of the complex wavenumber.

to 10^{-1} in a lossy medium, the error rate is smaller than 2% [11].

2.3 The Matrix Pencil Method

The matrix pencil method (or generalized pencil-of-function GPOF) is a known linear one-step methodology that approximates a function by a sum of complex exponentials [14].

A generalized eigenvalue problem is solved to find the unknown complex propagation constants for a given total field sampled at constant intervals δx as

$$H_x(n \delta x) = \sum_{m=1}^M A_m e^{jk_{y,m} n \delta x} \quad n = 1, 2, \dots, N \quad (2.19)$$

where N is the number of samples, M is the number of components and A_m and $k_{y,m}$ are the complex amplitude and phase factors for the m^{th} components. The total field at the n^{th} sampling point can be written as

$$H_x(x_n) = \sum_{m=1}^M A_m z_m^n \quad n = 1, 2, \dots, N \quad (2.20)$$

where $z_m = e^{jk_y m n \delta x}$ and $x_n = x_o + n \delta x$. Following the procedure for the MPM extractions as described in [15, 16] and by using the field samples, two matrices are defined as

$$\mathbf{G}_1 = (\tilde{y}_1 \ \tilde{y}_2 \ \tilde{y}_3 \ \dots \ \tilde{y}_P) \quad (2.21)$$

$$\mathbf{G}_2 = (\tilde{y}_2 \ \tilde{y}_3 \ \tilde{y}_4 \ \dots \ \tilde{y}_{P+1}) \quad (2.22)$$

with column vectors as

$$\tilde{y}_i = (H_i \ H_{i+1} \ H_{i+2} \ \dots \ H_{(N-P)+i-1})^T \quad (2.23)$$

where H_i are field sample points, \mathbf{G}_1 and \mathbf{G}_2 are $(N - P) \times P$ matrices and P is the pencil parameter used to obtain column vectors by windowing the field samples with the window length $N - P$.

By using (2.21) and (2.22) it can be shown that the poles z_m are the eigenvalues of the generalized eigenvalue problem

$$\mathbf{G}_2 \bar{e}_m = z_m \mathbf{G}_1 \bar{e}_m \quad (2.24)$$

where \bar{e}_m are the generalized eigenvectors of the pencil $(\mathbf{G}_2 - z_m \mathbf{G}_1)$. Using singular value decomposition [17] for \mathbf{G}_1 , it can be expressed as

$$\mathbf{G}_1 = \mathbf{U} \mathbf{D} \mathbf{V}^H \quad (2.25)$$

where \mathbf{U} and \mathbf{V}^H are unitary matrices associated with left and right singular vectors

respectively.

Here, \mathbf{H} denotes the conjugate transpose and \mathbf{D} is a diagonal matrix with singular values of \mathbf{G}_1 on the diagonal in descending order. \mathbf{U} , \mathbf{D} and $\mathbf{V}^{\mathbf{H}}$ are $(N - P) \times (N - P)$, $(N - P) \times P$ and $P \times P$ respectively. The largest M singular values and the associated left and right singular vectors are chosen in (2.25). By multiplying the left of (2.24) by $\mathbf{V} \mathbf{V}^{\mathbf{H}}$ and substituting in (2.25), the generalized eigenvalue problem reduces to a square matrix

$$\mathbf{D}_{(M \times M)}^{-1} \mathbf{U}_{(M \times N-P)}^{\mathbf{H}} \mathbf{G}_{2(N-P \times P)} \mathbf{V}_{(P \times M)} \mathbf{V}^{\mathbf{H}} \mathbf{e}_m^- = z_m \mathbf{V}_{(P \times M)} \mathbf{V}^{\mathbf{H}} \mathbf{e}_m^- \quad (2.26)$$

Therefore, z_m are the eigenvalues of the $M \times M$ matrix in (2.26). Once z_m are calculated, the complex propagation factors can be obtained by using

$$k_{y,m} = -\frac{\ln z_m}{\delta x}, \quad m = 1, 2, \dots, M \quad (2.27)$$

The complex amplitude components A_m can be obtained by using z_m in (2.20) and solving the resulting overdetermined linear system of equations by using a least-squares fit. Once the unknown complex amplitude and phase factors are obtained, the original near field behavior can be reconstructed.

2.4 Periodically Corrugated Metallic Surfaces

In this Section, the classical electromagnetic analysis of periodically corrugated surfaces is summarized. This methodology will be later used in the leaky wave analysis of such structures.

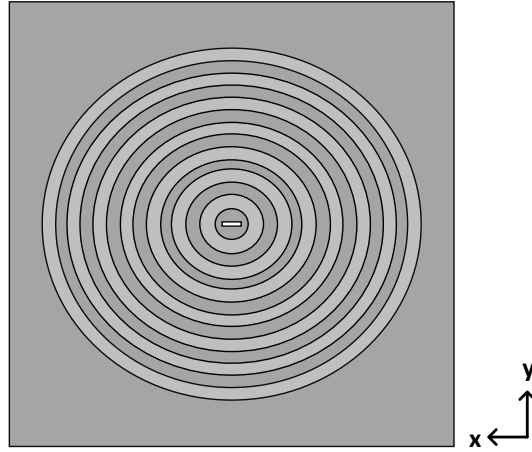


Figure 2.8: Front view of a standard Bull's Eye antenna with a subwavelength slot aperture.

2.4.1 Bull's Eye Antennas Design Configurations

A perfectly conducting metallic plane with a subwavelength aperture in its middle is considered. As explained in the introductory Chapter, the transmission of light through the aperture is significantly enhanced by several orders of magnitude when the metallic plane is surrounded by a set of concentric periodic rings (Fig. 2.8). Although this enhanced transmission of power was initially observed in optical frequencies, the same behaviour of the periodic structure under such conditions was observed in the microwave frequencies as well.

Theoretical research at optical frequencies available in [18, 19] extracted the design parameters for a periodically corrugated metal with respect to the free space wavelength λ_0 as

$$\begin{aligned}
 s_x &\ll \lambda_0 \\
 t &\approx \frac{n\lambda_0}{2} \\
 d &\approx \lambda_0 \\
 h &\approx \frac{(2n+1)\lambda_0}{4}
 \end{aligned} \tag{2.28}$$

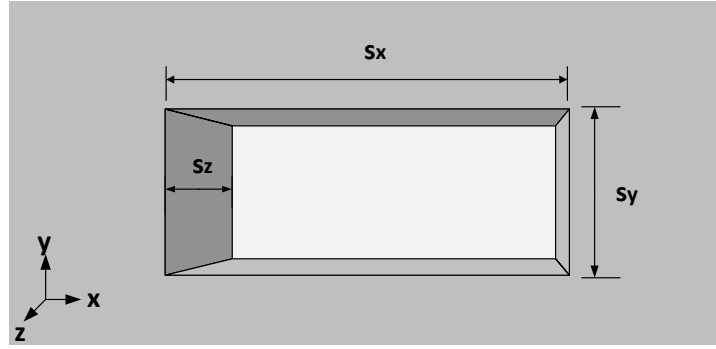


Figure 2.9: A subwavelength resonant slot on an infinite ground plane.

where n is a non negative integer. The parameters s_x , h , d and w refer to Figs. 2.8-2.10 and are subject to optimization for best performance. A proper excitation of the leaky mode across the corrugations requires the polarization of the excitation wave parallel to the corrugations (along y) [20]. The radiation is re-emitted in phase for $\lambda_0 \sim d$. The two joint mechanisms (gap cavity mode and in-phase gap re-emission) cause the extraordinary peak in transmittance [19].

The feeding slot design process should ensure a good matching between the feeding waveguide and the antenna (Fig. 4.3). Typically, its parameters are as

$$\begin{aligned}
 s_x &\sim \lambda_0/2 \\
 s_y &\ll \lambda_0 \\
 s_z &\sim \lambda_0/2
 \end{aligned}
 \tag{2.29}$$

where s_x and s_z (or, metal plate thickness t) control the longitudinal and transverse resonance [21].

2.4.2 Leaky Wave Analysis of 1-D Corrugated Metallic Surfaces with Narrow Gaps

An infinitely long corrugated plane as in Fig. 2.10 is considered, periodic along y with period d and uniform along x . The plane is perfectly conducting and its design details have been engineered via the specifications set in Section 2.4.1. The classic electromagnetic analysis of corrugated slabs with narrow gaps ([2, 22, 23]) suggest that the surface of Fig. 2.10 can be viewed as an infinite array of parallel plate waveguides mounted on a ground plane. From the same analysis, it is obligatory that $h < \lambda_0/4$ so that the wave above the metal is a TM wave [22]. This analytical periodic method refers only to designs with gap widths smaller than $w < \lambda_0/2$.

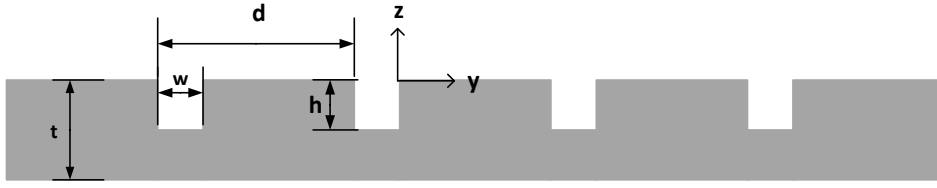
The periodic modulation of the metallic surface allows the expression of the E and H components with the use of Floquet's theorem, discussed in Section 2.1.1

$$E(y, z) = e^{-jk_y y} E^p(y, z) \quad (2.30)$$

where k_y is the fundamental longitudinal wavenumber along the y direction, $E^p(y, z) = E^p(y + nd, z)$ is a periodic function and n is a non-negative integer. For the unit cell of Fig. 2.10, it is assumed that the TEM field distribution (H_x, E_y) exists inside the gap due to $w < \lambda_0/2$, following the assumptions in [2, 22].

The input admittance Y_{in} looking into the gap ($-z$) can be written as a function of the periodic fields (E_y^p, H_x^p) as

$$\begin{aligned} E_y^{gap} &= V_0 \\ H_x^{gap} &= Y_{in} V_0 \end{aligned} \quad (2.31)$$

Figure 2.10: 1-D infinite size corrugated metallic plane with $w < \lambda_0/2$.

and since we are interested in an eigenvalue problem, $V_0 = 1$ is set.

In the region over the surface of the corrugations ($z > 0$), a *TM* surface plasmon mode propagates along z in high frequencies, supported by the interface between the metallic plane and the air. Due to the periodic texture, Floquet theory suggests that the guided wave towards y consists of an infinite number n of space harmonics as

$$\begin{aligned} k_{yn} &= k_y + 2\pi n/d = \beta_n - j\alpha \\ k_{zn} &= \pm \sqrt{(k_0^2 - k_{yn}^2)} \end{aligned} \quad (2.32)$$

where k_0 is the free space wavenumber, β_n is the phase or propagation constant of the n -th harmonic, α is the attenuation constant or leakage rate. Since $d \approx \lambda_0$, only the $n = -1$ space harmonic lies within the fast wave region ($|\beta_{-1}| < k_0$), producing the leaky wave radiation.

The magnetic vector potential A_z for the *TM* mode over the surface can be written as

$$A_z(y, z) = e^{-j k_y y} A_z^p(y, z) = e^{-j k_y y} \sum_{n=-\infty}^{\infty} C_n e^{-j \frac{2\pi n}{d} y} e^{-j k_{zn} z} \quad (2.33)$$

where C_n is an unknown constant. An analytical expression of E and H fields for $z > 0$ is

$$\begin{aligned}
 E_y(y, z) &= \frac{-1}{j\omega \epsilon_0} \sum_{n=-\infty}^{\infty} k_{yn} k_{zn} C_n e^{-j k_{zn} z} e^{-j k_{yn} y} \\
 H_x(y, z) &= \sum_{n=-\infty}^{\infty} -j k_{yn} C_n e^{-j k_{zn} z} e^{-j k_{yn} y}
 \end{aligned} \tag{2.34}$$

The expression of C_n can be found by forcing continuity of E_y at the level of the gap openings $z = 0$ and letting it vanish on the sides of corrugations as

$$E_y^p\left(-\frac{w}{2} < y - nd < \frac{w}{2}, 0\right) = E_y^{gap} \tag{2.35}$$

therefore we can write C_n as

$$C_n = \frac{-j \omega \epsilon_0 \sin(\pi n w/d)}{k_{yn} k_{zn} \pi n} \tag{2.36}$$

The next step is to determine the values of k_y by forcing the continuity of H_x at the level of the gap openings as

$$\int_{-w/2}^{w/2} E_y^{gap} H_x^{gap} = \int_{-w/2}^{w/2} E_y^{gap} H_x^p(y, 0) dy \tag{2.37}$$

which after some simplification leads to

$$Y_{in} w = -d\omega\epsilon_0 \sum_{-\infty}^{\infty} \frac{1}{k_{zn}} \frac{\sin^2(\pi n w/d)}{(\pi n)^2} \tag{2.38}$$

where Y_{in} is the input admittance looking into the gap ($-z$ direction) for a *TEM* shorted stub as $Y_{in} = -j Y_0 \cot(k_0 h)$, with Y_0 the free space admittance [24].

The right hand of equation (2.38) is proven to be the admittance Y_a looking out of the

gap by examining the power transmitted by the gap per unit length (in x direction). For our set of periodic field components inside the gap (H_x^p, E_y^p), the total transmitted power per unit length will be the contribution of the E_y^p component. Using Floquet theory it can similarly be written as in (2.31)

$$\begin{aligned} E_y^a &= 1 \\ H_x^a &= -Y_a \end{aligned} \tag{2.39}$$

where the negative sign is intended to give the impedance looking out of the aperture, and from the eigenvalue problem it is set $E_y^a = 1$.

Using the Parseval's theorem, the power transmitted is expressed as

$$P = - \int_{-d/2}^{d/2} E_y^p(y, 0) H_x^{p*}(y, 0) dy = |E_y^a|^2 w Y_a^* \tag{2.40}$$

or $Y_a = P^*/w$. Therefore Parseval's theorem can be written as

$$P = - \sum_{n=-\infty}^{\infty} E_y^p(y, 0) H_x^{p*}(y, 0) dy = |E_y^a|^2 w Y_a^* \tag{2.41}$$

which leads to the expression for Y_a as

$$Y_a = \frac{d}{w} \omega \epsilon_0 \sum_{n=-\infty}^{\infty} \frac{1}{k_{zn}} \frac{\sin^2(\pi n w/d)}{(\pi n)^2} \tag{2.42}$$

In conclusion, for the calculation of the fundamental wavenumber k_y of the leaky mode, the solution ends up in a transverse resonance equation at the level of the gap openings,

as

$$Y_{in} + Y_a(k_y) = 0 \quad (2.43)$$

The calculation of the complex wavenumber k_y derives from the numerical solution of equation (2.43). The solution of (2.43) can be found after considering some specializations that derive from the Floquet harmonics theory discussed in the previous Sections.

It is expected that the fundamental wave is slow ($\beta > k_0$), however only slightly smaller than the free space wavenumber ($\beta \approx k_0$). Also, since the structure is periodically modulated with $d \approx \lambda_0$ it is expected that only the $n = -1, -2$ harmonics are fast.

However, k_y is double valued, as it can be seen from (2.32). From leaky wave physics, described in Section 2.1, when $n = -1$ harmonic is fast ($|\beta_{-1}| < k_0$) then the leaky wave can be either forward ($\beta_{-1} > 0, \alpha_{z,n=-1} < 0$) or backward ($\beta_{-1} < 0, \alpha_{z,n=-1} > 0$). For the $n = -2$ harmonic, if it exists, it is limited that it is backward wave, therefore it is selected $\alpha_{z,n=-2} > 0$.

The authors of this method used the Secant method for the numerical solution of (2.43) with convergence met when the initial values of k_y are set slightly bigger than the free space wavenumber [25].

2.5 Commercial Electromagnetic Solver

The full-wave analysis of the electromagnetic problems of this dissertation has been realized via CST Microwave Studio TM. It is a very popular 3-D commercial tool, which offers a variety of specialized solvers depending on the nature of the electromagnetic problem [26]. In this thesis, three of its available solvers have been used, reported below.

CST offers a finite-integral time domain solver, which is suitable for most high frequency applications such as connectors, transmission lines, filters, antennas etc. and can obtain the entire broadband frequency behavior of the simulated device from a single calculation run. It is also efficient for periodic unit cell analysis by employing electric (magnetic) boundary conditions.

However, the time-domain solver can not be used when a fixed phase shift other than zero is required. This is a common requirement when studying obliquely incident plane waves or calculating the dispersion diagram of a periodic structure. For this purpose, the frequency domain solver must be used. This is a solver suitable for highly resonant structures. It also allows the imposition of periodic boundary conditions with arbitrary phase shift values. Finally, the eigenmode solver of CST is recommended for the eigenmode analysis of a closed structure, with no excitation source. Open boundaries are not supported by this solver, hence the obtained dispersion diagrams refer only to the phase constant, since an attenuation constant calculation would require open boundary conditions.

References

- [1] D. R. Jackson, A. A. Oliner, C. Balanis, "Leaky-wave antennas" in *Modern Antenna Handbook*, New York, NY, USA:Wiley, 2008.
- [2] G. Floquet, "Sur les quations Diffrentielles Linaires Coefficients Priodiques," *Annales de l'Ecole Normale Suprieur*, vol. 12, pp. 47–89, 1883
- [3] R. E. Collin, "Foundations for Microwave Engineering", 2nd ed. *New York: McGraw-Hill*, 1992, ch. 8.
- [4] G. Lovat, P. Burghignoli, D. R. Jackson, "Fundamental properties and optimization of broadside radiation from uniform leaky-wave antennas", *IEEE Trans. Antennas Propag.*, vol. 54, pp. 1442-1452, May 2006.
- [5] D. R. Jackson, A. A. Oliner, T. Zhao, and J. T. Williams, "Beaming of light at broadside through a subwavelength hole: Leaky-wave model and open stopband effect," *Radio Science*, vol. 40, no. 6, Dec. 2005.
- [6] P. Burghignoli, G. Lovat, D. R. Jackson, "Analysis and optimization of leaky-wave radiation at broadside from a class of 1-D periodic structures", *IEEE Trans. Antennas Propag.*, vol. 54, no. 9, pp. 2593-2604, Sep. 2006.

- [7] A. Sutinjo, M. Okoniewski, R.H. Johnston, "Beam-splitting condition in a broadside symmetric leaky wave antenna of finite length", *IEEE Antennas Wireless Propag. Lett.*, vol. 7, pp. 608-611, 2008.
- [8] C. A. Balanis, *Antenna Theory: Analysis and Design*, 2nd ed., *New York: Wiley*, 1997.
- [9] C. Caloz and T. Itoh, "Array factor approach of leaky-wave antennas and application to 1-D/2-D composite right/left-handed (CRLH) structures", *IEEE Microw. Wireless Compon. Lett.*, vol. 14, no. 6, pp. 274-276, Jun. 2004.
- [10] T. Kokkinos, C. D. Sarris, and G. V. Eleftheriades, "Periodic finite-difference time-domain analysis of loaded transmission-line negativerefractive-index metamaterials," *IEEE Trans. Microw. Theory Tech.*, vol. 53, no. 4, pp. 1488-1495, Apr. 2005.
- [11] T. Kokkinos, C. D. Sarris, G. V. Eleftheriades, "Periodic FDTD analysis of leaky-wave structures and applications to the analysis of negative-refractive-index leaky-wave antennas", *IEEE Trans. Microw. Theory Tech.*, vol. 54, no. 4, pp. 1619-1630, Apr. 2006.
- [12] P. Harms, R. Mittra, and W. Ko, "Implementation of the periodic boundary condition in the finite-difference time-domain algorithm for FSS structures," *IEEE Trans. Antennas Propag.*, vol. 42, no. 9, pp. 1317-1324, Sep. 1994.
- [13] T. Kokkinos, "Analysis and design of metamaterial-inspired microwave structures and antenna applications", PhD thesis, Loughborough University, UK.
- [14] T. K. Sarkar, O. Pereira, "Using the matrix pencil method to estimate the parameters of a sum of complex exponentials", *IEEE Antennas and Propagations Magazine*, vol. 37, 1995.

- [15] A. K. Ozturk and R. Paknys, "Analysis of Propagation Between Rows of Conducting Cylinders That Model Solid Surfaces Using the Same Surface Area Rule", *IEEE Trans. Antennas Propagat.*, vol. 60, no. 5, 2012.
- [16] Y. Hua, T. K. Sarkar, "Matrix pencil method for estimating parameters of exponentially damped/undamped sinusoids in noise", *IEEE Trans. Acoust. Speech Signal Process*, vol. 38, no. 5, pp. 814-824, 1990.
- [17] W. H. Press, B. P. Flannery, S. A. Teukolsky, and W. T. Vetterling, *Numerical Recipes*. Cambridge: Cambridge Univ. Press, 1986
- [18] L. Martín-Moreno, F. J. García-Vidal, H. J. Lezec, A. Degiron, and T. W. Ebbesen, "Theory of highly directional emission from a single subwavelength aperture surrounded by surface corrugations," *Phys. Rev. Lett.*, vol. 90, p. 167 401, Apr. 2003.
- [19] F. J-García-Vidal, H. J. Lezec, T. W. Ebbesen, and L. Martín-Moreno, "Multiple paths to enhance optical transmission through a single subwavelength slit," *Phys. Rev. Lett.*, vol. 90, p. 213901, May 2003.
- [20] M. Beruete, I. Campillo, J. S. Dolado, J. E. Rodríguez-Seco, E. Perea, and M. Sorolla, "Enhanced microwave transmission and beaming using a subwavelength slot in corrugated plane," *IEEE Antennas Wireless Propag. Lett.*, vol. 3, pp. 328–331, Dec. 2004.
- [21] M. Beruete, U. Beaskoetxea, T. Akalin, "Flat Corrugated and Bull's Eye antennas", in *Aperture Antennas for Millimeter and Sub-Millimeter Wave Applications*, Springer International Publishing AG, 2018, pp. 111-141.

- [22] R. E. Collin, "Field Theory of Guided Waves", *New York: Wiley-Interscience*, 2001, ch.4.
- [23] R. F. Harrington, *Time-Harmonic Electromagnetic Fields*, Hoboken, NJ: Wiley-Interscience, 2001, ch. 3.
- [24] D. M. Pozar, "Microwave Engineering", Hoboken, NJ :Wiley, 2012.
- [25] Kaw, Autar, Kalu, Egwu, "Numerical Methods with Applications" (1st ed.), 2008.
- [26] <https://www.3ds.com/products-services/simulia/products/cst-studio-suite/>

Chapter 3

Leaky Wave Analysis of Periodically Corrugated Metallic Surfaces

The analytical leaky wave analysis of a one dimensional periodically corrugated design with gap widths smaller than $\lambda_0/2$ (the upper limit where the *TEM* mode is supported inside the gaps) is available from the periodic method demonstrated in Section 2.4.2. For gap widths beyond this limit, this method ceases to give logical solutions, since higher order modes are expected to emerge and are not taken into account in the calculation. Corrugated designs with gaps larger than $\lambda_0/2$ have been encountered in several popular implementations ([1, 2]), since they form a prerequisite for high gain performance, while narrow-gap corrugated antennas achieve a low gain. Their leaky wave properties, therefore, are the key towards the comprehension of their far field performance. A rigorous methodology of the latter has not been available so far.

In this Chapter, a novel analytical periodic method is presented for the leaky wave analysis of 1D periodically corrugated structures with gaps larger than $\lambda_0/2$. This method

consists in the numerical solution of a transverse resonance equation that involves the gap admittance at the level of the gap openings. The results verify that gaps with width larger than $\lambda_0/2$ operate with the TM_1 mode of the considered parallel-plate waveguide. Furthermore, a full-wave dispersion analysis of a corrugated unit cell (of either narrow or wide gap compared to $\lambda_0/2$) is presented via a unit cell analysis tool, the fundamentals of which have been described in Section 2.2. It is the first time that this method is applied on a corrugated unit cell. The results of the two proposed novel leaky wave analysis techniques are compared against the well known but significantly slower matrix pencil method, also briefly described in Chapter 2. It is, also, the first time that the matrix pencil method is implemented for the leaky wave analysis of periodically corrugated antennas. Numerical results for the complex propagation constant of the leaky modes are extracted from the aforementioned methodologies for both types of corrugated designs, and their accuracy is discussed. The three aforementioned leaky wave analysis methodologies will be later used in Chapters 5 and 6, for the estimation of the leaky wave characteristics of the proposed novel corrugated antennas.

Finally, an analytical calculation of the radiation patterns of the aforementioned structures based on the extracted complex leaky wave propagation constant is developed via the array factor approach discussed in Section 2.1.3. This final step produces for the first time a complete methodology for the prediction of the radiation performance of periodic corrugated metal structures. Each gap case is examined separately and theoretical results are compared with simulations for various frequencies of interest.

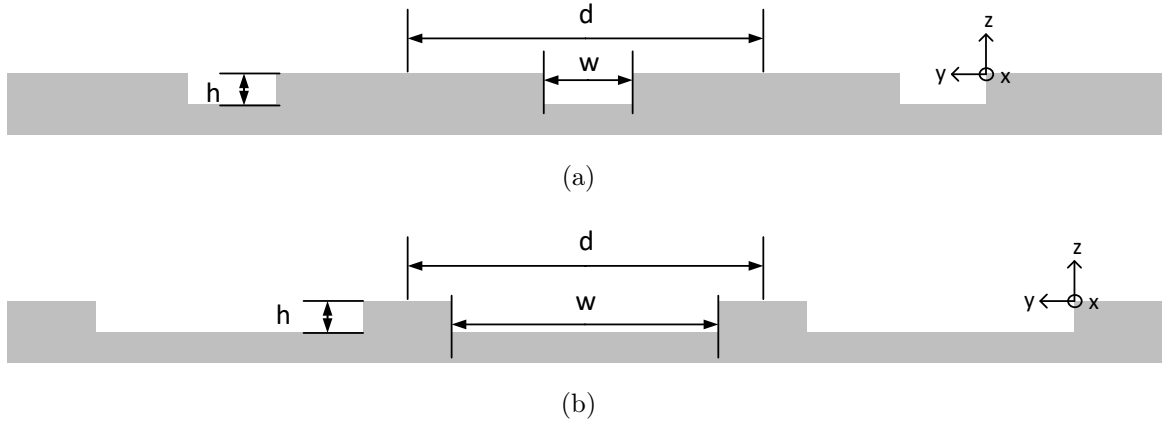


Figure 3.1: 1-D periodically corrugated structure with $d \sim \lambda_0$, $h \sim \lambda_0/4$ and (a) $w < \lambda_0/2$ and (b) $w > \lambda_0/2$.

3.1 Corrugated Metallic Antennas at 15 GHz

The design process of two periodically corrugated metallic antennas with period $d \sim \lambda_0$ is briefly described here, one that is characterized by $w < \lambda_0/2$ and one with $w > \lambda_0/2$ (as in Fig. 3.1). These antennas will be used as the reference models for the application of the leaky wave methodologies. They are considered of infinite size, meaning that they consist of a large number of unit cells, enough so that the launched leaky wave attenuates significantly when it reaches the end of the structure and reflections are avoided.

The design parameters are selected for optimum performance at 15 GHz, following the guidelines of Section 2.4.1. After an optimization process in CST Microwave StudioTM with the goal of maximum transmission at around 15 GHz, the unit cell dimensions for each gap case are defined as: periodicity $d = 19.62$ mm, height of corrugations $h = 3.31$ mm, gap width $w = 2.62$ mm for the narrow gap case (Fig. 3.1.a) and $w = 13.32$ mm for the wide gap case (Fig. 3.1.b). Throughout this Chapter, all the produced numerical results refer to these two designs.

3.2 Analytical Periodic Method for Corrugated Surfaces with Large Gaps

In this Section, a novel analytical periodic method is introduced for the calculation of the emerging leaky mode from corrugated designs with gaps larger than $\lambda_0/2$. An infinitely long perfectly conducting corrugated plane as in Fig. 3.1.b is considered, periodic along y and invariant towards x . The periodicity d is fixed close to the free space wavelength λ_0 . The height of the corrugations h should be smaller than $\lambda_0/4$ so that the surface impedance is inductive and a TM surface wave assumption is valid [3]. From the analysis in Section 2.4.2, the corrugated plane can be viewed as an infinite array of parallel plate waveguides mounted on a ground plane [3, 4].

The following analytical periodic method refers strictly to periodic corrugated planes with gap widths w larger than $\lambda_0/2$. The gap width w of the unit cell of Fig.3.1.b is large enough so that a TM_1 field distribution (H_x, E_y, E_z) can be assumed inside the gap. Using Floquet's theorem, we can write any E or H field component as [4]

$$\begin{aligned} E(y, z) &= e^{-jk_y y} E^p(y, z) \\ H(y, z) &= e^{-jk_y y} H^p(y, z) \end{aligned} \tag{3.1}$$

where k_y is the fundamental longitudinal wavenumber along y , and E^p , H^p are periodic functions with period d as

$$\begin{aligned} E^p(y + nd, z) &= E^p(y, z) \\ H^p(y + nd, z) &= H^p(y, z) \end{aligned} \tag{3.2}$$

where n is an integer. A transverse equivalent network at the level of the gap openings

($z = 0$) is employed below.

The input admittance Y_{in} looking into the gap ($z < 0$) can be written as a function of the periodic fields (E_y^p, H_x^p) as

$$\begin{aligned} E_{y,gap} &= V_0 \\ H_{x,gap} &= Y_{in} V_0 \end{aligned} \tag{3.3}$$

and since we are interested in an eigenvalue problem, $V_0 = 1$ is set [5].

In the air region over the level of the corrugations ($z > 0$), a *TM* surface plasmon mode propagates due to $h < \lambda_0/4$, supported by the interface between the metallic plane and the air. Since the structure is periodic with period d , Floquet's theorem suggests that the guided wave towards y consists of an infinite number n of space harmonics as [5]

$$\begin{aligned} k_{yn} &= k_y + 2\pi n/d = \beta_n - j\alpha \\ k_{zn} &= \pm \sqrt{(k_0^2 - k_{yn}^2)} \end{aligned} \tag{3.4}$$

where k_0 is the free space wavenumber, β_n is the phase or propagation constant of the n -th harmonic, α is the attenuation constant or leakage rate. Since the period d of the structure is fixed close to λ_0 , only the $n = -1$ space harmonic lies within the fast wave region ($|\beta_{-1}| < k_0$), producing the leaky wave radiation [6]. It should be noted that the phase constant β_n is defined for each n -harmonic, while α is the same for all harmonics.

An analytical expression for the fields in the region $z > 0$ can be produced. The

H_x, E_y, E_z components of the surface TM mode can be written as [4]

$$\begin{aligned} H_x &= \sum_{n=-\infty}^{\infty} -jk_{yn}A_n e^{-jk_{yn}y} e^{-jk_{zn}z} \\ E_y &= j \frac{1}{\omega\epsilon_0} \frac{\partial H_x}{\partial z} \\ E_z &= -j \frac{1}{\omega\epsilon_0} \frac{\partial H_x}{\partial y} \end{aligned} \quad (3.5)$$

where A_n is an unknown constant. The boundary conditions at the interface between the metallic surface and the air ($z = 0$) requires continuity of the tangential electric and magnetic fields and the tangential electric field to vanish everywhere else. Regarding the boundary conditions for E_y , the constant A_n is calculated as

$$A_n = \frac{-j\omega\epsilon_0 \sin(\pi n w/d)}{k_{yn}k_{zn} \pi n} \quad (3.6)$$

Inside the gap of the unit cell, where $0 \leq y \leq w$, the requirement of continuity for H_x , multiplied by $E_{y,gap} = V_0$ leads to the expression of the input admittance Y_{in} from (3.3) and, consequently, to the calculation of leaky mode wavenumber k_y as

$$Y_{in}w = -d\omega\epsilon_0 \sum_{n=-\infty}^{\infty} \frac{1}{k_{zn}} \frac{\sin^2(\pi n w/d)}{(\pi n)^2} \quad (3.7)$$

where Y_{in} is also the input admittance looking into the gap ($-z$ direction) for a TM shorted stub as

$$\begin{aligned} Y_{TM} &= Y_0 k_0 / \sqrt{k_0^2 - k_c^2} \\ Y_{in, TM} &= -j Y_{TM} \cot(h \sqrt{k_0^2 - k_c^2}) \end{aligned} \quad (3.8)$$

where $k_c = \pi/w$ is the cutoff wavenumber of the TM_1 mode [7].

The right hand of (3.7) is here proven to be the admittance Y_a looking out of the gap (towards $+z$) by examining the power transmitted by the gap per unit length (in x direction). For the periodic field components inside the gap (H_x^p, E_y^p, E_z^p), correspondent to the assumed TM_1 mode, the total transmitted power per unit length is the contribution only of the E_y^p component, since the Poynting vector of the E_z^p component is directed towards y (thus not in the required direction towards the aperture). Using Parseval's theorem, the power transmitted by the fields inside the gap can be expressed as [5]

$$P = - \int_{-d/2}^{d/2} E_y^p(y, 0) H_x^{p*}(y, 0) dy = |E_y^a|^2 w Y_a^* \quad (3.9)$$

and from the eigenvalue problem, $E_a = 1$ is set, therefore leading to an expression for Y_a as

$$Y_a = \frac{d}{w} \omega \epsilon_0 \sum_{n=-\infty}^{\infty} \frac{1}{k_{zn}} \frac{\sin^2(\pi n w/d)}{(\pi n)^2} \quad (3.10)$$

exactly as the narrow-gap case.

Returning to (3.7), for the calculation of the wavenumber k_y of the leaky mode, the solution can be reduced to a transverse resonance equation at the level of the gap openings ($z = 0$), as

$$Y_{in, TM} + Y_a(k_y) = 0 \quad (3.11)$$

The calculation of the complex wavenumber k_y stems from the numerical solution of (3.11), which is solved with the Secant method [8, 10]. Initial assumptions regarding the proper selection of the roots and convergence criteria for the Secant method are explained briefly below.

From Floquet's theory, it is expected that only the fundamental wave is slow $|\beta| > k_0$

Table 3.1: Numerical convergence at 14.2 GHz.

$\pm m$	β_{-1}/k_0	α/k_0
3	-0.0332	0.0041
8	-0.033	0.0041
11	-0.0329	0.0041
15	-0.0329	0.0041

and close to the free-space wavenumber, $\beta \approx k_0$. The periodicity of the structure fixed close to the free-space wavelength ($d \approx \lambda_0$) allows only the $n = -1$ harmonic to be fast, or even the -2 at some cases.

Second, since k_y is double valued (from (3.4)), it is determined that when the $n = -1$ harmonic is fast ($|\beta_{-1}| < k_0$) then the leaky wave can be either forward ($\beta_{-1} > 0, \alpha_{z,n=-1} < 0$) or backward ($\beta_{-1} > 0, \alpha_{z,n=-1} > 0$). If the $n = -2$ harmonic exists, then it should be a backward wave, therefore it is selected that $\alpha_{z,n=-2} > 0$.

Convergence is met with initial values $k_y \approx k_0$. The number of harmonics ($\pm m$) included in the execution of the Secant method determines the convergence criterion at ± 11 harmonics at 14.2 GHz, as it can be seen in Table 3.1 for the design of Fig. 3.1.b. Compared to the convergence table found in [9] for *TEM* mode assumption, the results of Table 3.1 demonstrate a much faster convergence, as even with $m = \pm 3$ harmonics the solution is quite accurate.

3.3 Unit Cell Periodic Method

In this Section, a full-wave dispersion analysis technique, the fundamentals of which have been described in Section 2.2, is applied for the first time on a corrugated unit cell. Simulations are performed with the Time and the Frequency Domain Solver of CST. This technique can be used for any unit cell geometry, regardless of its complexity. Also, only

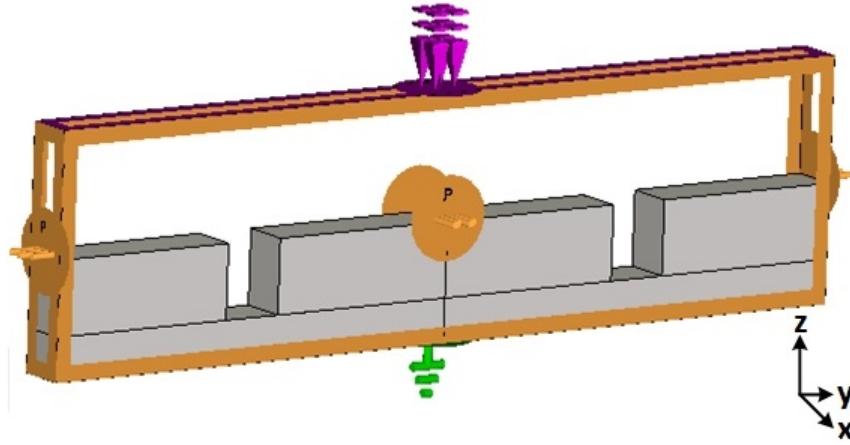


Figure 3.2: Boundary conditions for the implementation of the unit cell periodic method in CST. Periodic boundary conditions are imposed at x, y axes, open boundary is chosen along $+z$ and PEC is chosen along $-z$ axis.

two unit cells are needed for the leaky wave analysis in contrast to other known full-wave methods (for example, the matrix pencil method), offering the significant advantage of simplicity and reduced computational time.

Fig. 3.2 shows periodic boundary conditions imposed along x and y on a unit cell in CST environment, open boundary along $+z$ and PEC along $-z$. The electromagnetic problem for both gap cases is considered invariant towards x , same as in the analytical periodic methods of Sections 2.4.2 and 3.2.

The propagation constant β_{-1} of the leaky mode along the y axis is calculated by the observation of the maximum generated electric field strength at resonant frequencies after fixing the phase difference ξ between the longitudinal y -boundaries of the unit cell. The excitation is a small ideal dipole source. The maximum of the electric field component E is tracked at resonant frequencies f_r which are dependent on the corresponding phase shift ξ , according to

$$\beta_{-1} = k_0(f_r)d \quad (3.12)$$

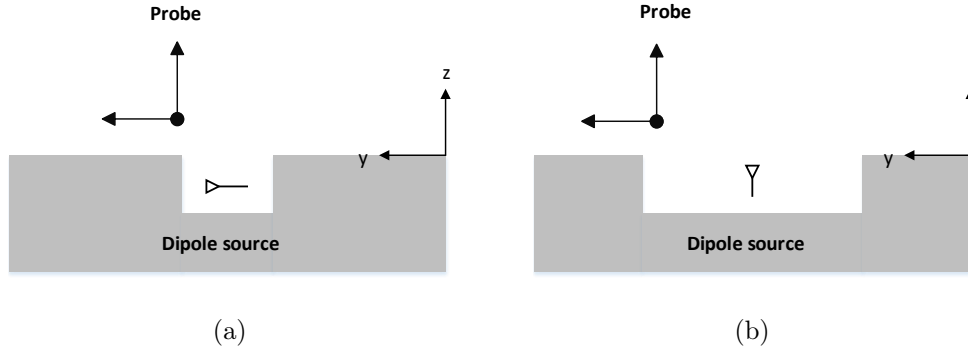


Figure 3.3: Unit cell setup for the calculation of β_{-1} (a) case of $w < \lambda_0/2$ and (b) case of $w > \lambda_0/2$.

The angle ξ is scanned from 0° to 180° with a step of 5° . From the known leaky wave formula, the radiation angle θ of the emerging beam is associated with the propagation constant β_{-1} as

$$\theta = \sin^{-1}(\beta_{-1}/k_0) \quad (3.13)$$

The simulation setup for β_{-1} of the corrugated unit cells of both gap cases can be viewed at Fig. 3.3. For the narrow gap case, the dipole is y -oriented in order to excite the E_y component of the assumed TEM mode. For the wide gap case, with the present higher order mode, the dipole is z -oriented so as to distinguish between the TEM and the TM_1 mode, since the E_z part exists only in the latter. The y component of the electric field across the direction of the emerging leaky wave is tracked with suitably placed probes. The simulated electric field distribution of Fig. 3.4 determines the probe position above the internal corners of corrugations, where the area of maximum E field concentration is. With respect to the source position, the small gap of the unit cell of Fig. 3.3.a doesn't allow much freedom, in contrast to the unit cell of 3.3.b where simulations showed that small variations of the port position inside the gap do not affect significantly the produced

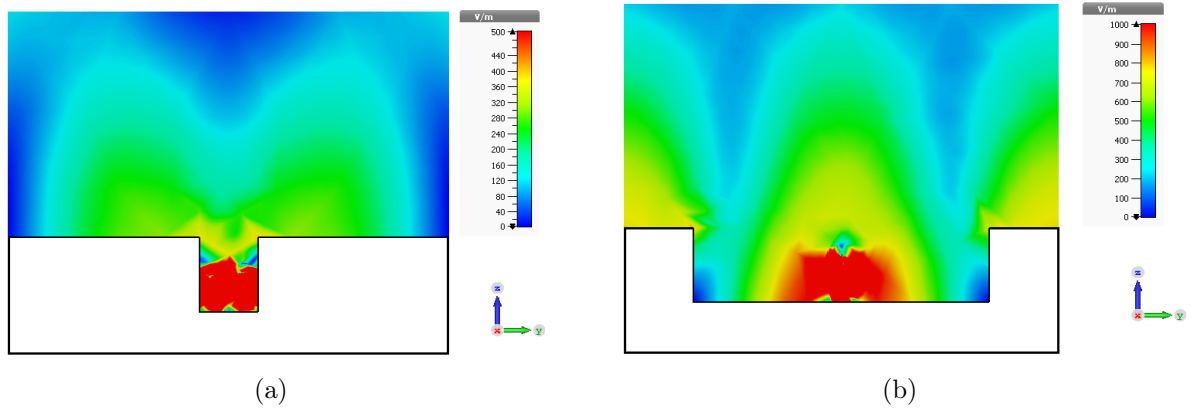


Figure 3.4: Simulated E -field of a corrugated unit cell at 15 GHz with (a) $w < \lambda_0/2$ and (b) $w > \lambda_0/2$.

E -field, provided that there is enough open space above the corrugations.

The attenuation constant α of the leaky mode is calculated by the excitation of two consecutive unit cells terminated with periodic boundary conditions (Fig. 3.5). One unit cell is fed with a small dipole source. A double longitudinal phase shift 2ξ is imposed towards the y boundaries, as the total distance of the travelling wave is $2d$. The maxima of the E_y components are tracked at sampling points that are spaced one period apart. The maximum electric fields E_0 and E_1 of the first and the second unit cell with respect to the source position are measured at carefully located probes, at the near field of the unit cell where the maximum E -field strength is expected (inner corners of corrugations). Within a period d , the electric field is exponentially attenuated by a factor of $e^{-\alpha d}$. This decay of the electric field between the two measurement points leads to the calculation of the leakage rate

$$\alpha = -\frac{1}{d} \ln \frac{E_1}{E_0} \quad (3.14)$$

What should be noted is that this methodology for the calculation of α is valid only for

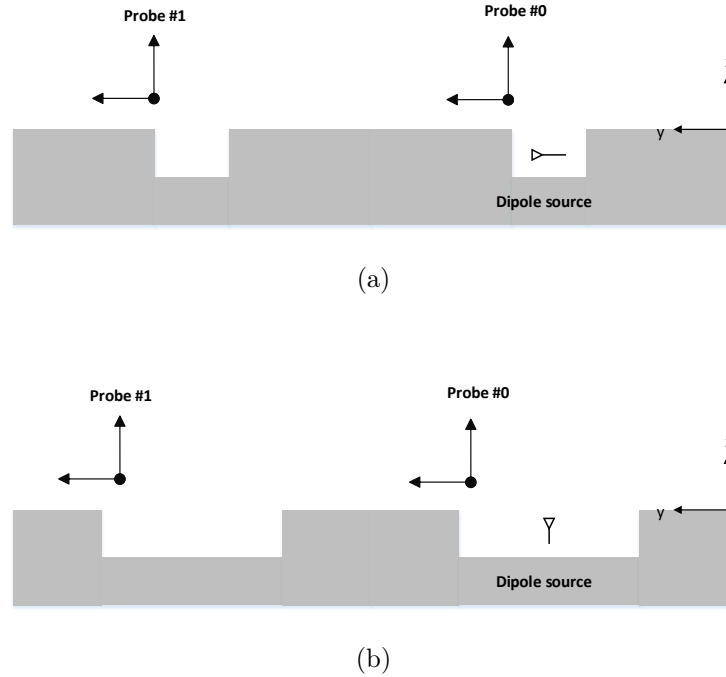


Figure 3.5: Unit cell setup for the calculation of α (a) case of $w < \lambda_0/2$ and (b) case of $w > \lambda_0/2$.

small expected values of attenuation, as a high error rate has been reported for higher magnitudes of α [11].

3.4 The Application of Matrix Pencil Method on Corrugated Antennas

The matrix pencil method, explained in detail in Chapter 2, is used here for comparison purposes for the leaky wave analysis of corrugated antennas. For each unit cell of Fig. 3.1, an antenna of sufficiently large size (approaching the infinite size assumption) is simulated. The antenna length towards y is 38 unit cells so as to attenuate significantly the travelling wave once it reaches the end of the antenna (Fig. 3.6). The problem is invariant towards x , in accordance with the analysis of the previous Sections. The feeding of the antennas

is via an open-ended waveguide aperture at the edge of the antenna.

The size of the simulated model makes this technique a lot slower than the much faster and efficient analytical and unit cell based techniques presented in the previous Sections. However, it is the only other available technique in order to calculate the complex propagation constant of the leaky modes and compare the results of our new proposed methods. The matrix pencil method in our case requires approximately 16 minutes on an Intel(R) Core(TM) processor simulation PC with 8 GB RAM. In contrast, the simulation time for our unit-cell full-wave method is just under 1 minute, making it around 16 times faster.

In order to avoid unwanted reflections that could disturb the computation of the leaky mode, the sampling field domain is set as in Fig. 3.6. The two unit cells closer to the radiating source are excluded from the sampling field monitor (in blue color), due the strong expected fields generated from the direct aperture beaming. The x -boundaries are terminated with periodic boundary conditions in order to make the antenna infinite towards x and avoid reflections. This also reduces the computational problem to a 2D topology. Additionally, a distance approximate to two unit cells at the edge of the antenna is excluded from the sampling domain, so as to minimize the effect of the wave impedance mismatch between the antenna and the surrounding air.

The analysis of Sections 3.2 and 3.3 makes the H_x component suitable for sampling, as it exists in both implementations (dominant TEM and TM_1 modes inside the gaps for the narrow and wide gap case respectively). Specifically, the complex aperture H_x -field is sampled at constant intervals δx just above the level of corrugations ($z = 0$) and it can be approximated as a sum of M exponential components

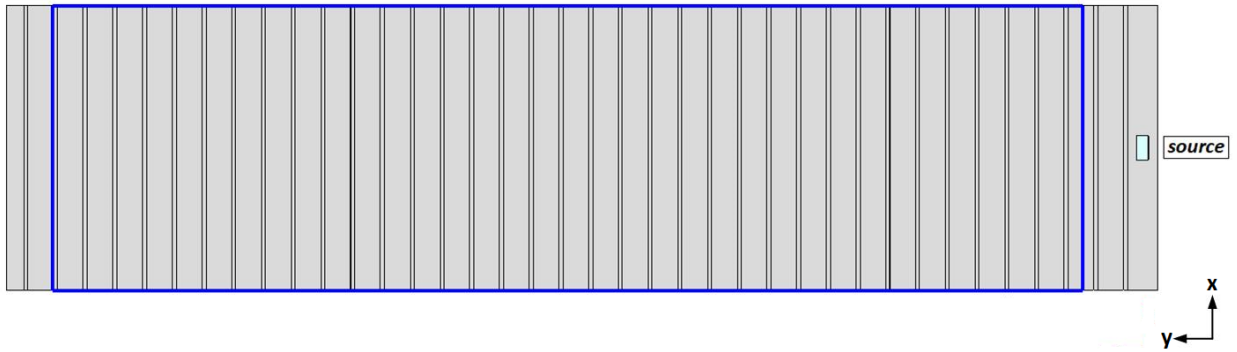


Figure 3.6: Front view of the 2D corrugated antenna geometry. The blue rectangular defines the sampling domain for the H_x component to be approximated by the matrix pencil method, just above the level of corrugations.

$$H_x(n \delta x) = \sum_{m=1}^M A_m e^{jk_{y,m} n \delta x} \quad (3.15)$$

where n is an integer, $k_{y,m} = \alpha_m + j\beta_m$ is the complex wavenumber of the m component along y and A_m is the complex magnitude of the correspondent mode. This arbitrary number of exponential components M is then summed to reconstruct the radiation pattern of the antenna. The dominant leaky mode ($|\beta| < k_0$) can be tracked by the its corresponding field strength A_m of each m component with complex wavenumber $k_{y,m}$. It should be reminded that the structure supports an infinite number of n space harmonics, according to Floquet theory, of which the fundamental mode is a slow wave ($|\beta| > k_0$) and the -1 harmonic is designed to be a fast leaky wave.

For the narrow gap antenna, where the TEM mode dominates inside the gaps, results from the extracted matrix pencil components are in Table 3.2. At 13 GHz, the harmonic $m = 1$ is a slow travelling wave ($|\beta| > k_0$) travelling towards the negative direction $-y$ and harmonics $m = 2, 3$ seem like surface waves due to $\beta \approx 1$. All harmonics decay exponentially towards $+y$ due to $\alpha_m < 0$. The dominant leaky mode, corresponding to the -1 Floquet harmonic is the $m = 6$ due to its strongest complex amplitude A_m . The

Table 3.2: Matrix pencil extracted components of the 2D narrow gap antenna at 13 GHz.

Prop.	m	$jk_{y,m}/k_0 = \alpha_m + j\beta_m$	$A_m(A/mm)$
-y	1	$-0.0029 + j1.0316$	$0.0728 - j0.0222$
-y	2	$-0.0020 - j0.8863$	$-0.0022 + j0.1059$
-y	3	$-0.0019 + j0.7141$	$-0.1120 + j0.0394$
-y	4	$-0.0019 + j0.3942$	$0.1557 - j0.0000$
-y	5	$-0.0019 - j0.5662$	$-0.0518 - j0.1336$
-y	6	$-0.0020 - j0.2463$	$0.1106 + j0.1267$
-y	7	$-0.0020 + j0.0739$	$-0.1534 - j0.0747$
-y	8	$-0.0075 + j0.0026$	$-0.0251 - j0.0710$

Table 3.3: Matrix pencil extracted components of the 2D wide gap antenna at 12.5 GHz.

Prop.	m	$jk_{y,m}/k_0 = \alpha_m + j\beta_m$	$A_m(A/mm)$
-y	1	$-0.0051 - j0.5563$	$0.0066 + j0.0878$
-y	2	$-0.0056 + j0.4061$	$0.0729 + j0.1758$
-y	3	$-0.0055 + j0.3722$	$0.1259 + j0.0835$
-y	4	$-0.0052 - j0.2335$	$-0.0995 + j0.3878$
-y	5	$-0.0046 - j0.2675$	$0.0613 + j0.2312$
-y	6	$-0.0032 - j0.0750$	$0.0637 - j0.0775$
-y	7	$-0.0059 + j0.0860$	$-0.0886 + j0.1840$
-y	8	$-0.0076 + j0.0508$	$0.0168 + j0.1494$

corresponding slow Floquet harmonic $n = 0$ should be the $m = 1$. Table 3.3 shows the matrix pencil results for the wide gap antenna. The dominant -1 Floquet harmonic of the TM_1 mode should be the $m = 4$ component, due to its strongest amplitude $A_{m=4}$.

For more accurate results, the final dispersion diagrams produced by the matrix pencil technique were executed for a larger number of M components, and the dominant leaky mode was tracked with its corresponding A_m amplitude for each frequency point.

3.5 Dispersion Analysis: Numerical Results

The leaky wave analysis of each unit cell case is presented and discussed separately. The significance of this analysis lies in the prediction of the far field patterns of the corresponding infinite size antennas. Therefore, antenna design configurations can be set,

based only on the knowledge of the leaky mode wavenumber distribution.

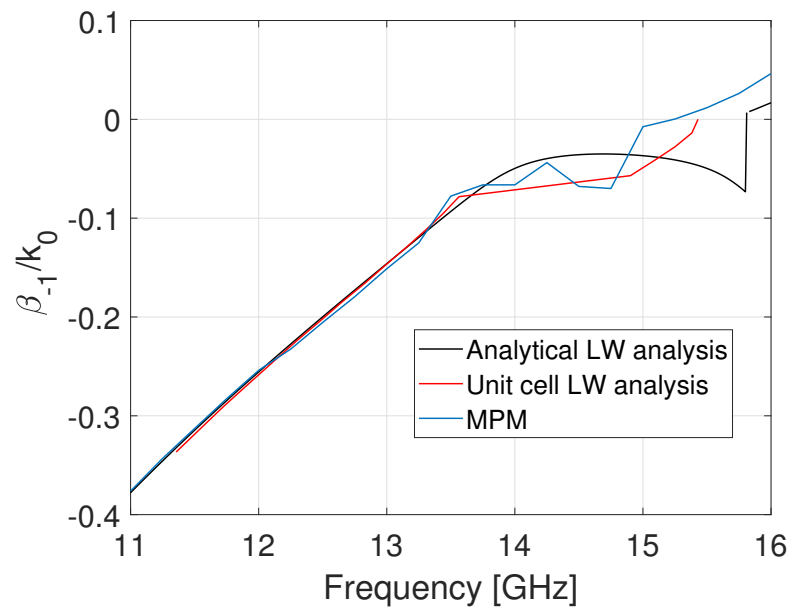
3.5.1 Case of $w < \lambda_0/2$

Fig. 3.7 shows the complex wavenumber distribution normalized to the free space wavenumber k_0 . The analytical periodic method results refer to the methodology of Section 2.4.2. Only the -1 harmonic of the dominant *TEM* mode is depicted for the phase constant, as only this is expected to propagate due to $d \sim \lambda_0$.

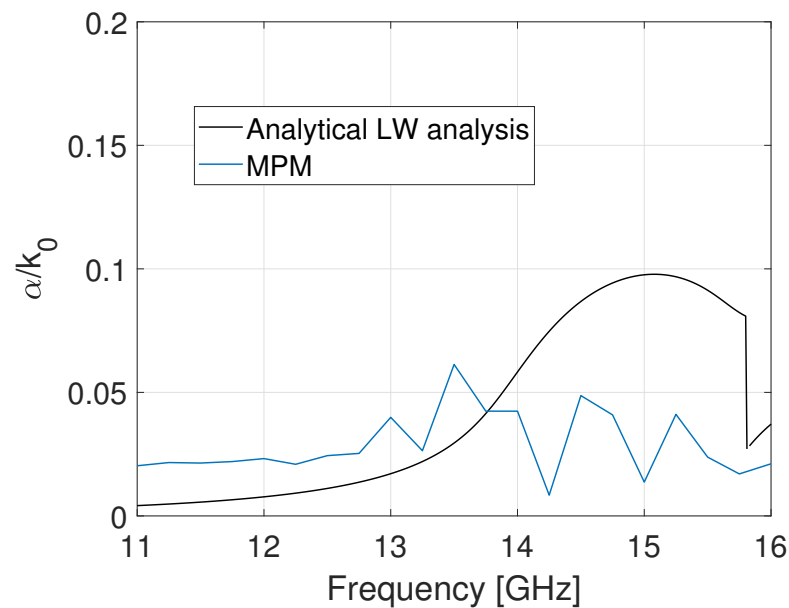
The calculated solution is a complex fast wave in all the frequency band examined ($|\beta_{-1}/k_0| < 1$). Radiation close to broadside (from $\beta \approx 0$) for the unidirectionally-fed structure is expected at 15.2 GHz according to the matrix pencil method, 15.4 GHz according to the analytical periodic method and 15.8 GHz according to the full-wave method. It is also obvious from the distribution of β_{-1} and α that the analytical method crashes after the frequency where $\beta \approx 0$, beyond which the method ceases to give logical solutions. This defect has already been reported by the authors of [9] and is possibly associated with the weak transmission of the leaky wave to the next neighboring cell (complex wave no longer supported).

The main radiating beam scans with frequency from the backward quadrant (when $\beta_{-1} < 0$) to the positive ($\beta_{-1} > 0$). The condition $|\beta_{-1}| < \alpha$ for a directive beam at broadside for the symmetrically-fed antenna of infinite size [12], determine that such a radiation is expected between 13.8 GHz and 16 GHz, based on the analytical periodic method results. A nearly identical distribution of phase constant is calculated from all methods, confirming their accuracy.

Fig 3.7.b shows the leakage rate α predicted by the analytical periodic method and the



(a)



(b)

Figure 3.7: Complex wavenumber distribution of k_{y-1} for the narrow gap case (a) phase constant β_{-1} and (b) attenuation constant α .

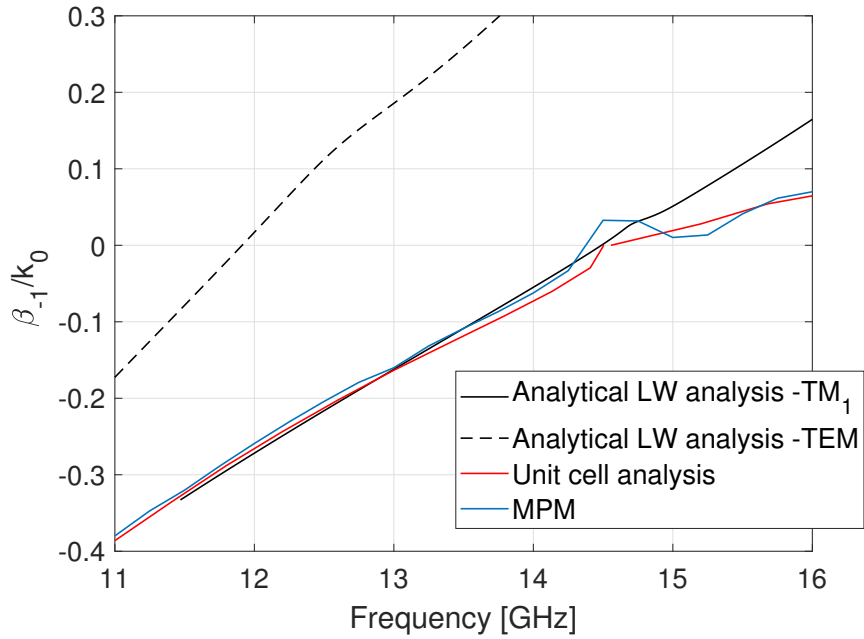
matrix pencil. A high similarity can be observed between the two methods as a increases with frequency up to 14 GHz (matrix pencil) or 15 GHz (analytical periodic), and after that, a drop is observed. The application of the unit cell method on this narrow gap unit

cell fails to give logical results. This is due to the fact that the high simulated values of the electric fields around the corrugations led to an unstable calculation of α from (3.14). Also, the exact values of the electric field were very sensitive with respect to the position of the probes. Actually, the failure of the unit cell method for this case is expected due to the relatively large α predicted by the other two methods, as for a large α the unit cell periodic method produces a high error rate, as has been reported for this technique applied to different types of leaky wave antennas [11].

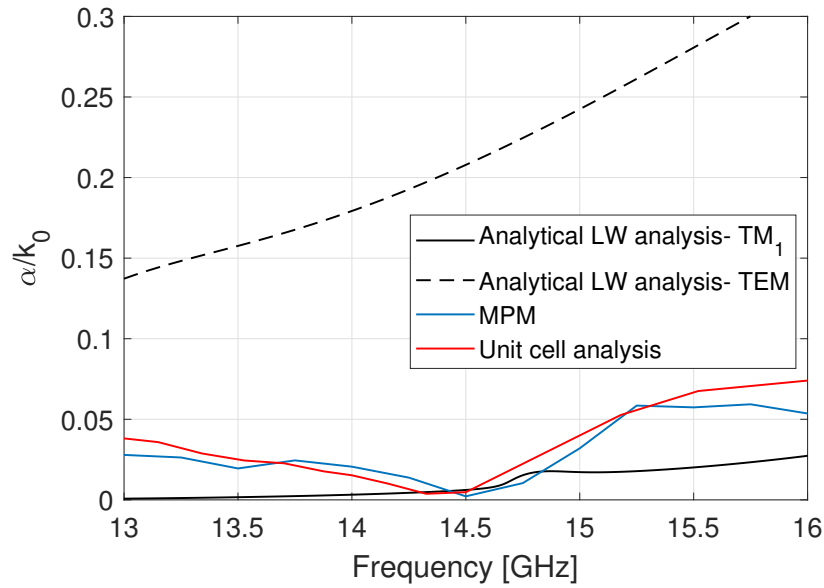
3.5.2 Case of $w > \lambda_0/2$

The dispersion analysis of the wide gap case is implemented, using the analytical periodic methods of Sections 2.4.2 and 3.2, the unit cell method of Section 3.3 and the matrix pencil method. It is expected that the TM_1 mode mainly excites the leaky mode, however it is interesting to examine the percentage of the attenuated TEM mode that is still present. For the calculation of the latter, the method of Section 2.4.2 is applied. All results are concentrated in Fig. 3.8. The accuracy of all methods with respect to the calculation of the β_{-1} of the dominant mode (TM_1) is evident with the highly similar distribution of β_{-1} , which confirms the propagation of a fast leaky wave along the entire frequency band examined ($|\beta_{-1}| < k_0$).

The frequency where radiation close to broadside is expected (for the unidirectionally-fed antenna) in this case is predicted by all methods at around 14.2 GHz. Below this frequency, the phase constant obtains negative values which means that the beam of the infinite size antenna scans towards the negative quadrant. From the condition $|\beta_{-1}| < \alpha$, a broadside radiation for the symmetrically-fed infinite size antenna is expected in the



(a)



(b)

Figure 3.8: Complex wavenumber distribution of k_{y-1} for the wide gap case (a) phase constant β_{-1} and (b) attenuation constant α .

frequency band between 14.15 GHz and 14.34 GHz for an infinite size antenna (the analytical periodic method for the TM_1 mode). The TEM mode is significantly attenuated,

especially at the frequencies over 14 GHz, where the antenna is designed to operate. Its contribution is expected only with side lobes, and its normalized attenuation constant is about an order of magnitude higher than the one of the TM_1 mode.

The values of normalized leakage rate α for the TM_1 mode are similar from all methods (less than 10^{-1}). Compared to the narrow gap case, the attenuation constant for the wide gap case is on average much smaller. The simulated E fields of Fig. 3.4 confirm this theoretical result, since for the wide gap unit cell the E -field strength is by several orders of magnitude larger than the E -field of the narrow gap unit cell. The highly directive performance of most cited Bull's Eye antennas, which typically consist of wide gaps, is justified from the low leakage rate α predicted by this analysis. It is also implied that a corrugated antenna of wide gaps would need a large overall size for a typical 90% transmission of power, from the condition $L = 0.18\lambda_0/\alpha$. Antennas with narrow gaps have not been preferred in literature due to their high leakage rate (which leads to lower realized gain).

3.6 Far Field Pattern Calculation

This Section offers the analytical calculation of the radiation patterns of one-dimensional symmetrically-fed corrugated structures of finite size (Fig. 3.9). For this calculation, the values of $k_{y,-1}$ are considered known from the previous dispersion analysis, although they refer to infinite size antennas.

The feeding of these antennas is via a subwavelength slot aperture of dimensions ($s_x, s_y=13.89$ mm, 2.438 mm) in their middle (Fig. 3.10), with its E field parallel to the corrugations (along y), and an equal number N of unit cells at each side of the aperture

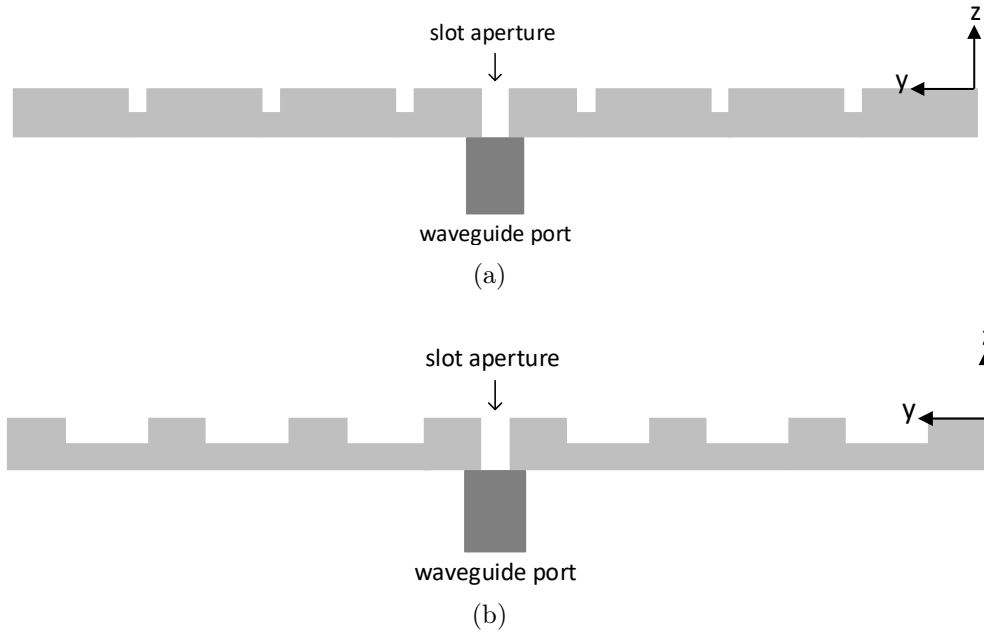


Figure 3.9: Symmetrically-fed corrugated antennas (a) narrow gap case and (b) wide gap case.

(Fig. 3.9). From antenna theory, the total radiation pattern is the linear superposition of the slot radiation pattern and the leaky wave radiation pattern produced by the wave propagation across the corrugations.

From [13], the electromagnetic field radiated by a slot aperture mounted on an infinite ground plane can be approximated by its dominant TE_{10} mode (Fig. 3.10). An analytical expression of fields for the E -plane of the aperture leads to

$$E_{\theta,slot} = E_0 \operatorname{sinc}\left(\frac{k_0 s_y \sin\theta}{2}\right) \quad (3.16)$$

where θ is the radiating angle measured from broadside.

The leaky wave radiation pattern is approximated by the array factor (AF) approach presented in Section 2.1.3. Any leaky wave antenna of Fig. 3.9 can be considered as a symmetrically-fed phased-array antenna, with inter-element spacing d of N point radiators. For the plane on the right side of the slot, the antenna is considered to be fed with

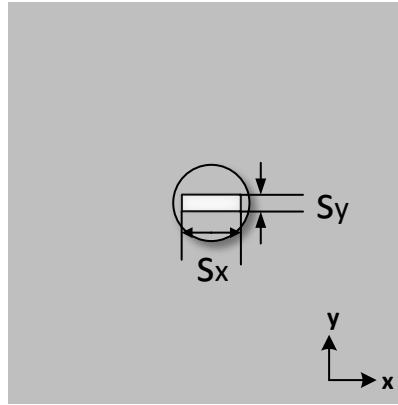


Figure 3.10: Radiating slot aperture on an infinite ground plane surrounded by one corrugated ring.

a phase function $\xi(\theta_0)$ along y and an exponential magnitude function $I(y) = I_0 e^{-\alpha y}$ set as

$$\xi_n = -(n-1) k_0 d \sin \theta_0 \quad (3.17)$$

$$I_n = I_0 e^{-\alpha(n-1)d}$$

where θ_0 is the radiation angle measured from broadside.

Since we have a bidirectional (symmetrical) antenna, the lower limit of the AF is modified accordingly to $-N$ in order to include the point radiators placed at the other side of the feed. The AF of the 1-D antenna is given by

$$AF = \sum_{n=-N}^N I_n e^{j(n-1)k_0 d \sin \theta + j \xi_n} \quad (3.18)$$

In the calculation of this AF , the right spacing of radiators is a challenging problem. The maximum E_y distribution along the longitudinal plane of a finite size corrugated antenna assists in the determination of radiators. Specifically, the E_y values around the inner corner of a unit cell of Fig. 3.2 correspond to the magnitude I_0 of the array factor. Overall, the ratio of E_0/I_0 is an approximate estimation of the side lobe level of the radiation pattern.

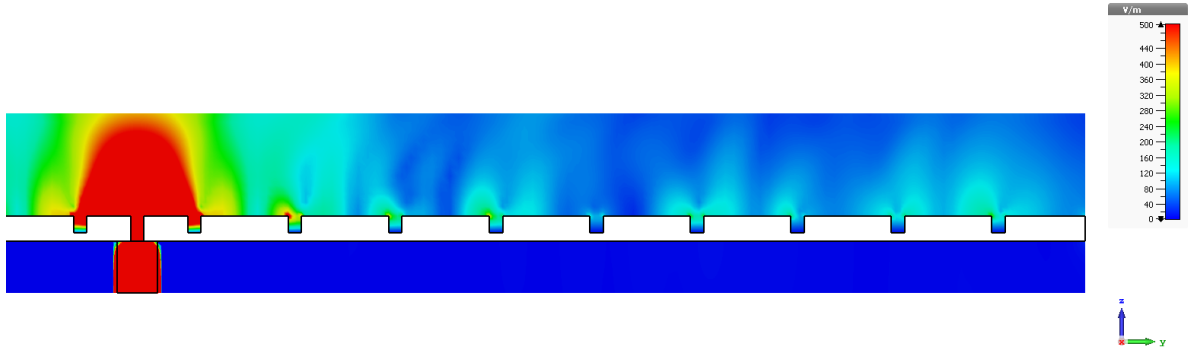


Figure 3.11: Simulated (maximum) E -field at 14.8 GHz for the narrow gap antenna.

Regarding the determination of the element factor EF , each gap can be considered as an aperture in free space with uniform distribution along the y -dimension. The equivalent problem can be formed according to Love's Equivalence Principle and image theory [13]. Therefore, the element factor of each radiating gap can be expressed as

$$EF = I_0 \cos\theta \operatorname{sinc}\left(k_0 w_y \frac{\sin\theta}{2}\right) \quad (3.19)$$

where w_y is the considered width of the aperture. The radiation pattern of the leaky wave antenna is then calculated as

$$AF * EF + E_{\theta,slot} \quad (3.20)$$

Each gap case is examined below separately.

3.6.1 Case of $w < \lambda_0/2$

Consider a bidirectional finite-size antenna, fed in the middle by a subwavelength slot (s_x, s_y) of Fig. 3.10 and the unit cell of Fig. 3.1.a. Fig. 3.11 depicts the maximum electric field distribution (along y) at 14.8 GHz, which is a frequency where maximum (broadside) radiation is expected ($\beta_{-1} \approx 0$ from the leaky wave analysis). A variation of fields with

Table 3.4: Broadside range for the narrow gap antenna at 15 GHz.

<i>Unit cells</i>	Simulated broadside range [GHz]	Predicted broadside range [GHz]
10	13.4-16.2	13.8-16
14	13.6-15.9	
18	13.8-16	

time, as obtained from full-wave simulations, shows that each gap can be considered as a radiating resonant slot. Therefore, the element factor of (3.19) can be used with $w_y = w$, the actual width of the unit cell gap.

For comparison purposes, several antennas of different sizes were simulated in CST Microwave Studio. A summary of the radiation pattern characteristics of the simulated bidirectional narrow-gap antenna is shown in Table 3.4, compared with the analytical results of the leaky-wave analysis. The predicted broadside range is from $|\beta_{-1}| < \alpha$, based on the dispersion results of the analytical periodic method. The infinitely long antenna assumption is met with 18 unit cells, as the broadside frequency range of the simulated antenna is precisely the frequency range predicted by the theoretical analysis. The rather small number of unit cells required to meet the infinitely long antenna assumption can be attributed to the large values of α , that is associated with the size L of the antenna required for a 90% transmission of power.

A comparison between the theoretically calculated radiation patterns and the simulated in CST at frequencies of interest can be seen in Fig. 3.12. The theoretical radiation patterns use the complex wavenumber of the analytical periodic method and the matrix pencil method. At 14.8 GHz, where $\beta_1 \approx 0$ (Fig. 3.7) the antenna radiates at broadside, where at 13 GHz a split beam pattern is expected. Overall, a very good agreement between theoretical calculations and simulation is observed. The radiating angle θ and the width of the main beam are nearly identical with the simulated plot, which verifies the

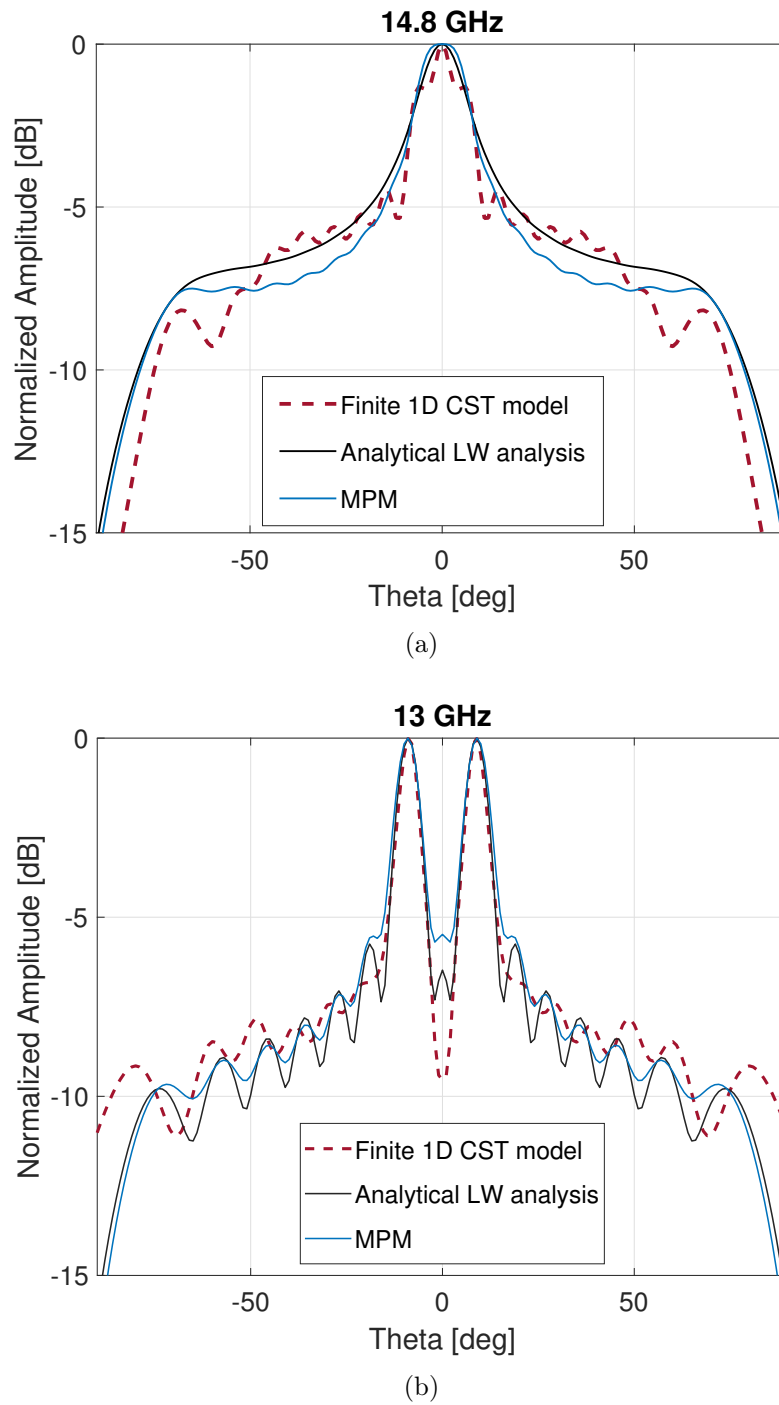


Figure 3.12: Normalized radiation patterns of the 18-unit cell narrow gap antenna at (a) 14.8 GHz, (b) 13 GHz.

accurate leaky wave results of both methodologies.

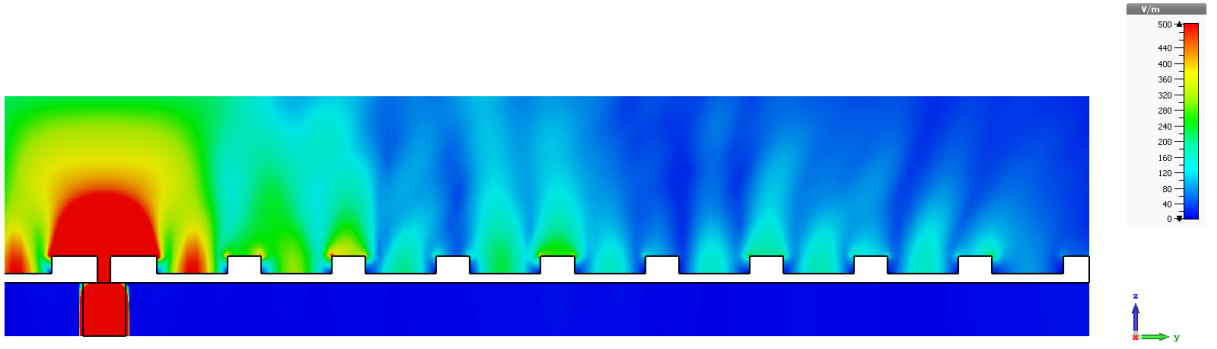


Figure 3.13: Simulated E_y -field (maximum) at 14.2 GHz for the wide gap antenna.

3.6.2 Case of $w > \lambda_0/2$

The discussion for the radiation patterns for the case of $w > \lambda_0/2$ is more complicated due to the assumption of the higher order mode TM_1 inside the gap. The simulated E_y field of a finite size antenna of 18 unit cells at 14.2 GHz is in Fig. 3.13, which is the expected frequency of maximum radiation (from the leaky wave analysis). A closer inspection is available at Fig. 3.14. The phase animation of E_y in Fig. 3.14 shows that the corners of the gap radiate in turn every phase change of $\pi/2$. This is the TM_1 mode of the parallel plate waveguide that begins to form within the corrugations [7].

The initial attempt in forming the array factor for this case was to consider as element factor the E_θ component of this TM_1 mode. The far field patterns, however, were distorted. This was probably due to the depth of the corrugations h which is so small that doesn't allow the full formation of the mode inside the gap. In addition there is significant scattering of the field from the top right angle corners of the corrugations.

After extensive investigation, the most accurate approach of the point radiator spacing was found to be at the left corner of each corrugation (a total of N radiators spaced a period apart). At this corner, an aperture in free space is considered, with width w_y

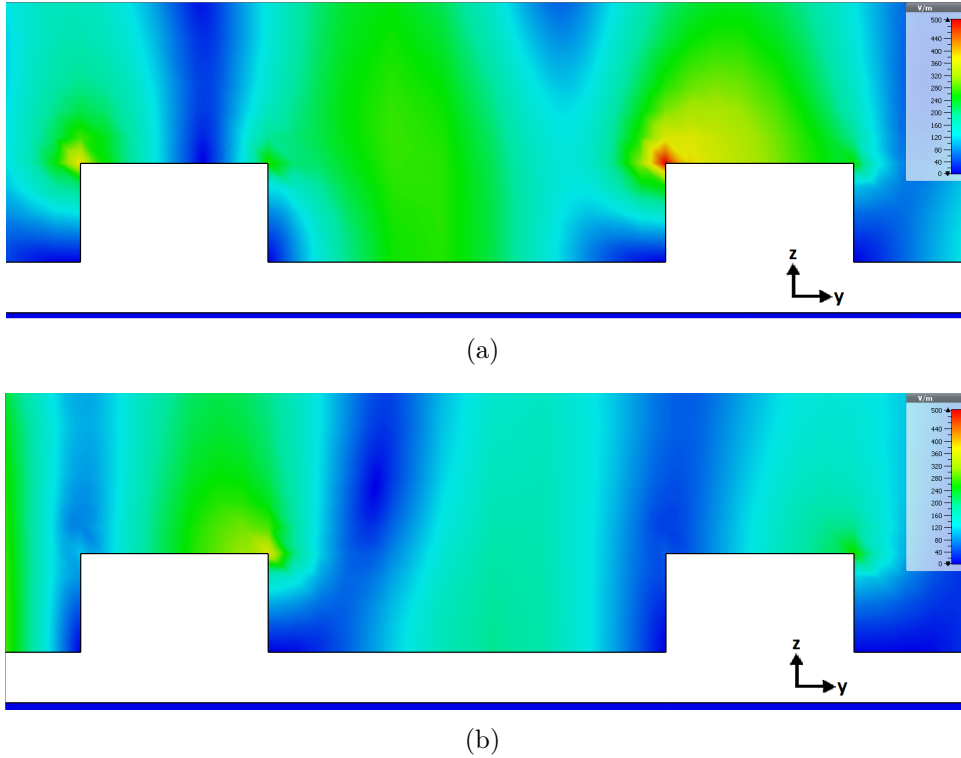


Figure 3.14: Phase animation of the simulated E_y -field at 14.2 GHz (a) 0° (b) 90° .

approximating zero $w_y \approx 0$ (3.19). It is evident in Figs. 3.13 and 3.14 that the wavefront emerges from the left corner of each corrugation, where the E -field is stronger, therefore this assumption is expected to be quite accurate.

Since the leakage rate α is low from the leaky wave analysis comparatively to the narrow gap antenna, the infinite size assumption is expected to be satisfied with a large number of unit cells N . Symmetrical antennas of sizes from 10 to 26 unit cells were simulated and their far field behaviour is summarized in Table 3.5. The predicted values refer to the TM_1 mode only, based on the leaky wave analysis of the analytical periodic method. For the 26-unit cell antenna, simulations exhibit a broadside radiation in the frequencies between 14.05 GHz and 14.4 GHz, which is very close to the predicted broadside range of the leaky wave analysis. The infinite size assumption is met with an even bigger number of unit cells for the wide gap antenna, however such simulations were not

Table 3.5: Broadside range for the wide gap antenna at 15 GHz.

<i>Unit cells</i>	Simulated broadside range [GHz]	Predicted broadside range [GHz]
10	13.4-15.6	14.15-14.34
14	13.8-15.1	
18	14-15	
26	14.05-14.4	

performed due to large computational time.

The theoretically calculated radiation patterns of a wide gap antenna of 26 unit cells are depicted in Fig. 3.15. The patterns that correspond to the analytical methodology, have taken into account the existence of both TM_1 and TEM modes. The agreement between theoretical calculations and measurements with respect to the main beam angle, width and side lobe level is considered satisfactory.

In this case of wide gaps, however, initial calculations of the radiation patterns did not match in main beam angle and width with the simulated at the exact same frequency. The depicted patterns that stem from the leaky wave analysis are actually for higher frequencies, by approximately 0.2 GHz (a shift of 1.5%). This shift is a common issue with leaky wave antennas, as for antennas of moderate size with low α , edge effects and reflections of the surface wave due to impedance mismatch between air and metal disturb the main radiating mode [14, 15].

The effect of the TEM mode on the far field patterns of the wide gap antenna can be seen in Fig. 3.16 for the antenna of 26 unit cells. The comparative results of this Figure refer to the analytical periodic method only, as the unit cell method and the matrix pencil method incorporate all the radiating fields. Although the patterns look quite similar, with the same beam angle, width and side lobe level, the consideration of the TEM mode affects the position of nulls generated by the array factor. The difference

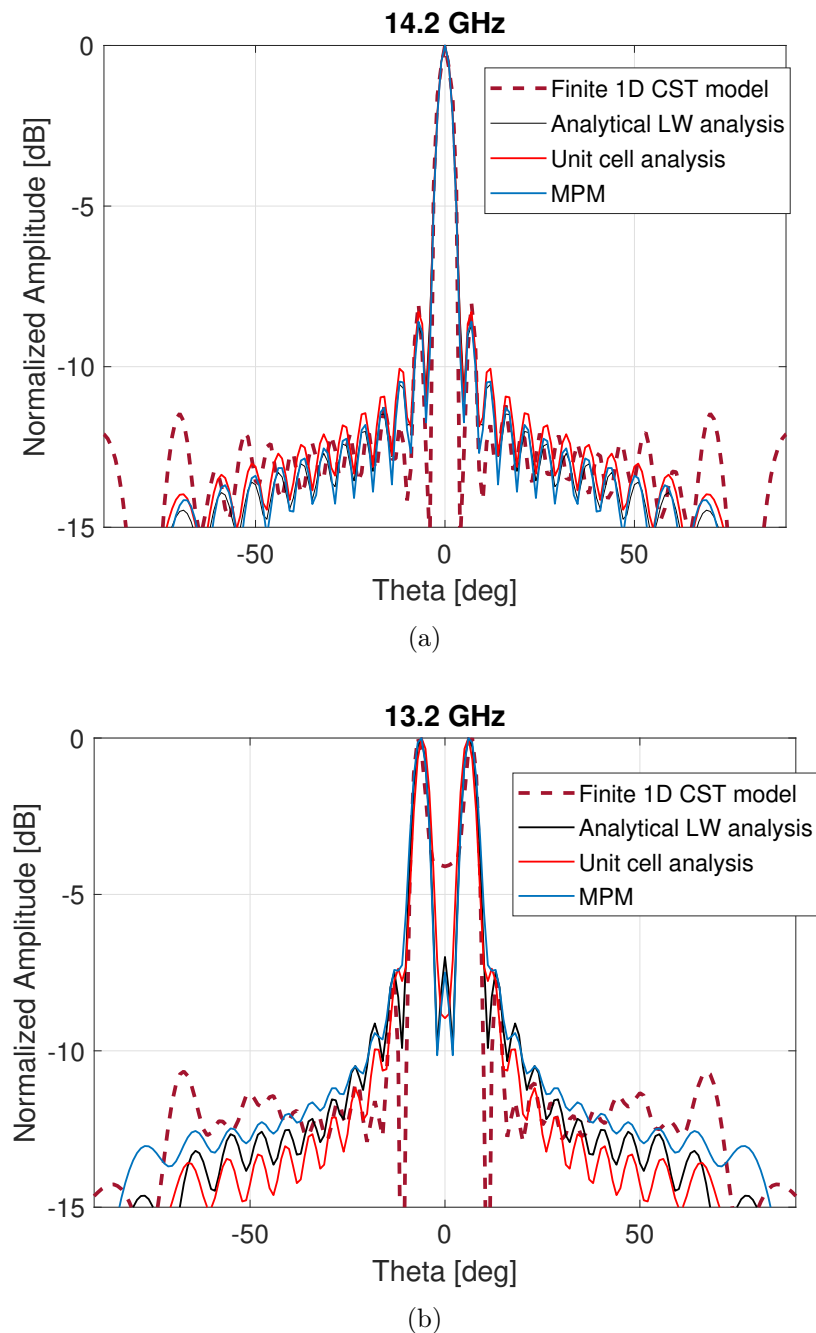


Figure 3.15: Normalized radiation patterns of the 26-unit cell wide gap antenna at (a) 14.2 GHz, (b) 13.2 GHz.

in the position of the nulls is more evident in the pattern of lower frequency (Fig. 3.16.b), where the TEM mode is still of moderate α . For the pattern of Fig. 3.16.a, the radiation is almost entirely the contribution of the TM_1 , as expected from the leaky wave analysis.

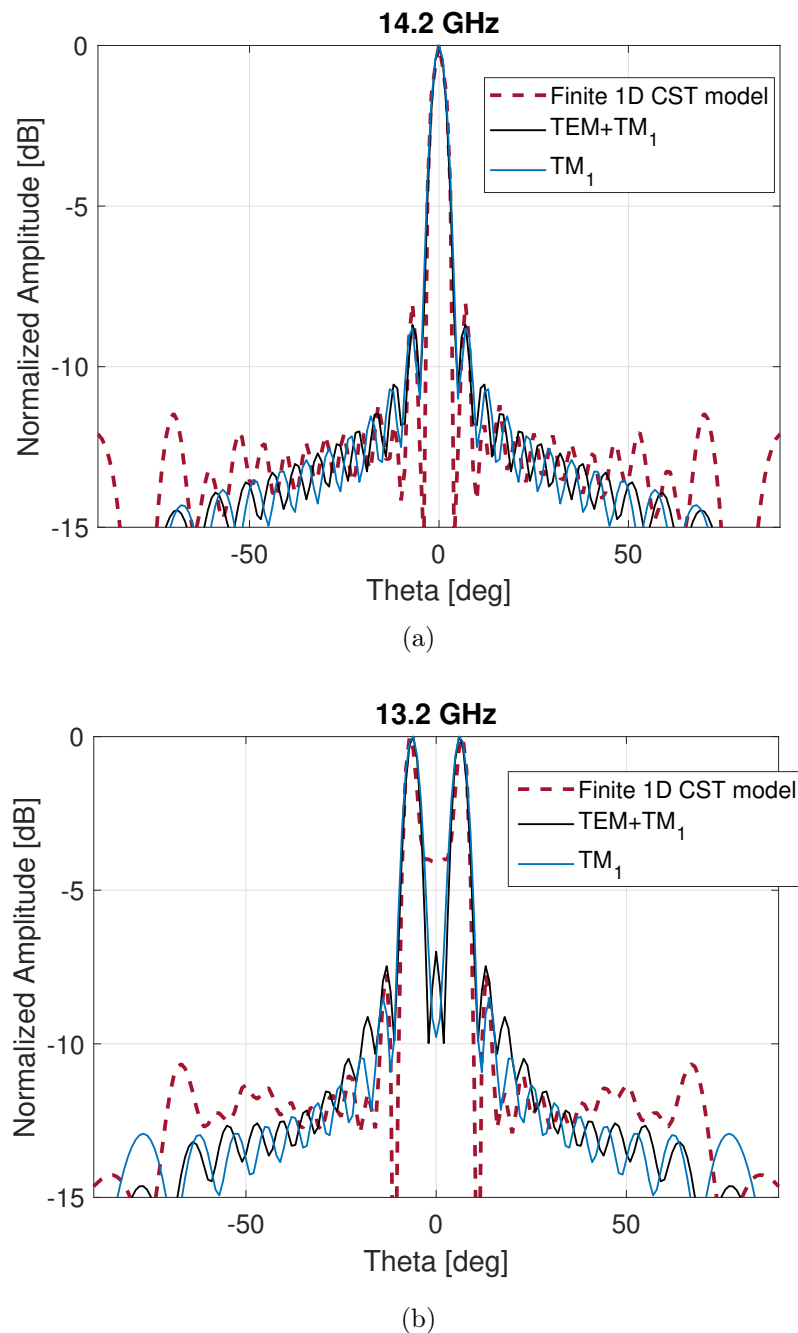


Figure 3.16: Effect of the TEM mode on the radiation patterns of the 26-unit cell wide gap antenna at (a) 14.2 GHz, (b) 13.2 GHz.

3.7 Conclusion

A complete dispersion analysis of 1D periodically corrugated metal surfaces has been presented in this Chapter. The novel analytical periodic method for corrugated surfaces

with large gaps consists in a simple transverse resonance equation at the level of the gap openings, with the assumption of a higher order mode propagation inside the gaps.

A full-wave periodic unit cell method, has been applied for the first time on periodic corrugated metal antennas and has been proven accurate. Additionally, the application of the known matrix pencil method on this type of antennas was performed and its results validate the previous leaky wave analysis techniques. Finally, for the first time a radiation pattern calculation is available for this type of corrugated metal surfaces, after an extensive investigation of the near field distribution.

Very good agreement is achieved between the results predicted using our leaky wave analysis methods and the simulations of a finite size antenna in CST. Slight disagreements in the results can be attributed to the infinite antenna size assumption of the leaky wave analysis, while the CST software analyzes finite size models. It should also be reminded that the array factor approach considers point radiators and is more accurate for a very close spacing of leaky wave radiators, while in our case the radiators are spaced nearly a wavelength apart. What is more, a part of the surface plasmon mode is reflected back to the structure once it reaches the edge of the antenna, due to the impedance mismatch between the metal and the air. These reflections have not been taken in to consideration in our analysis. It should also be mentioned that an alternative approach for the calculation of the radiation patterns that involves the radiation integral calculation has been examined, with less successful results.

Overall, the application of the matrix pencil method requires simulations of very large antennas at the expense of computational time. On the other hand, the analytical method provides quick convergence with satisfactorily accurate results and the unit cell method

requires only two unit cells for the dispersion analysis. In particular, the full-wave unit cell method is about 16 times faster in computational time than the execution of the matrix pencil method, while the analytical periodic method is executed within seconds.

The leaky wave analysis methodologies (novel and existing) explained in this Chapter are very useful for the next Chapters, where the far field performance of the introduced novel corrugated designs can be predicted only by the knowledge of the dominant leaky mode.

References

- [1] M. Beruete, I. Campillo, J. S. Dolado, J. E. Rodríguez-Seco, E. Perea, F. Falcone, and M. Sorolla, "Very low profile "Bull's Eye" feeder antenna", *IEEE Antennas Wireless Propag. Lett.*, vol. 4, pp. 365–368, 2005.
- [2] C. J. Vourch, T. D. Drysdale, "V-band Bull's eye Antenna for CubeSat Applications," *IEEE Ant. Wireless Prop. Lett.*, Vol 13, pp. 1092 – 1095, 2014
- [3] R.E. Collin, "Field Theory of Guided Waves", *New York: Wiley-Interscience*, 2001, ch.4.
- [4] R. E. Collin, "Foundations for Microwave Engineering", 2nd ed. *New York: McGraw-Hill*, 1992, ch. 8.
- [5] R. F. Harrington, Time-Harmonic Electromagnetic Fields. Hoboken, *NJ: Wiley-Interscience*, 2001, ch. 3.
- [6] D. R. Jackson, A. A. Oliner, C. Balanis, "Leaky-wave antennas" in *Modern Antenna Handbook*, New York, NY, USA:Wiley, 2008.
- [7] Pozar, David M., "Microwave Engineering", Hoboken, NJ :Wiley, 2012. Print.
- [8] Kaw, Autar, Kalu, Egwu, "Numerical Methods with Applications" (1st ed.),2008.

- [9] A. Sutinjo and M. Okoniewski, "A Simple Leaky-Wave Analysis of 1-D Grooved Metal Structure for Enhanced Microwave Radiation", *IEEE Transactions on Antennas and Propagation*, vol. 60, no. 6, pp. 2719-2726, June 2012.
- [10] J. H. Richmond, N. N. Wang, and H. B. Tran, "Propagation of surface waves on buried coaxial with periodic slots," *IEEE Trans. Electromagn. Compat.*, vol. EMC-23, no. 3, pp. 139–145, Aug. 1981
- [11] T. Kokkinos, "Analysis and design of metamaterial-inspired microwave structures and antenna applications", PhD thesis, Loughborough University, UK.
- [12] P. Burghignoli, G. Lovat, D. R. Jackson, "Analysis and optimization of leaky-wave radiation at broadside from a class of 1-D periodic structures", *IEEE Trans. Antennas Propag.*, vol. 54, no. 9, pp. 2593-2604, Sep. 2006.
- [13] C. A. Balanis, *Antenna Theory: Analysis and Design*, 2nd ed., New York: Wiley, 1997.
- [14] P. Kosmas, A. P. Feresidis and G. Goussetis, "Periodic FDTD Analysis of a 2-D Leaky-Wave Planar Antenna Based on Dipole Frequency Selective Surfaces," in *IEEE Transactions on Antennas and Propagation*, vol. 55, no. 7, pp. 2006-2012, July 2007.
- [15] C. Mateo-Segura, G. Goussetis and A. P. Feresidis, "Sub-Wavelength Profile 2-D Leaky-Wave Antennas With Two Periodic Layers," in *IEEE Transactions on Antennas and Propagation*, vol. 59, no. 2, pp. 416-424, Feb. 2011.

Chapter 4

Effects of the Feeding Structure on Planar Corrugated Metal Antennas

This Chapter is focused on practical implementations of the feeding structure of periodic corrugated metallic antennas. As described in Chapters 1 and 2, a family of planar antennas, known as Bull's Eye antennas, has been developed in recent decades. These antennas normally consist of a set of corrugated rings on a metallic plane that surrounds a subwavelength radiating aperture. All of the cited implementations thus far typically use a half-wavelength thin slot as a feeding radiating aperture at the cost of a limited matching bandwidth, along with narrow gain bandwidth.

In this Chapter novel feeding mechanisms are proposed in order to tackle the problem of narrowband matching performance. These techniques have been applied on a Bull's Eye antenna at around 300 GHz, where the fabrication is more challenging in order to demonstrate the viability of the proposed design at such high frequencies. The simulated results confirm a very broadband matching performance and can be quite important in

practical scenarios where the antenna should be integrated with superimposed radomes or packaging materials that normally affect the input matching performance. Furthermore, as it will be demonstrated in Chapter 5 a broadband matching is needed in applications where a wide antenna gain-bandwidth is expected with the introduction with novel corrugations designs, therefore a good input performance is required. The simulated results of this Chapter have been validated with a measured fabricated prototype.

4.1 A Bull's Eye Antenna at low THz

In this Section, a Bull's Eye antenna that is excited via a subwavelength slot is compared with two identical antennas of the same type that use two novel feeding techniques; the open-ended waveguide aperture and the tapered waveguide aperture.

4.1.1 The Subwavelength Slot Aperture

A Bull's Eye antenna is designed for operation at around 300 GHz. Following the guidelines of Section 2.4.1, a corrugated metallic antenna of 11 rings is designed as in Fig. 4.1. The periodicity of the structure is at the order of a free space wavelength $d = 0.961$ mm. The rest of the dimensions are: gap width $w = 0.611$ mm, height of corrugations $h = 0.164$ mm, total plate height $h_p = 0.911$ mm, central ring radius at 1.3 mm, and overall antenna size 26.5×26.5 mm². The antenna radiates via a subwavelength slot aperture, with dimensions $s_x = 0.583$ mm and $s_y = 0.159$ mm, optimized in CST Microwave Studio (Fig. 4.1.b). The feeding is with a WR-3 waveguide at the rear side of the plate.

This number of rings was selected after a parametric study on the optimum number of rings for maximum directivity, reasonable computational time and overall antenna size.

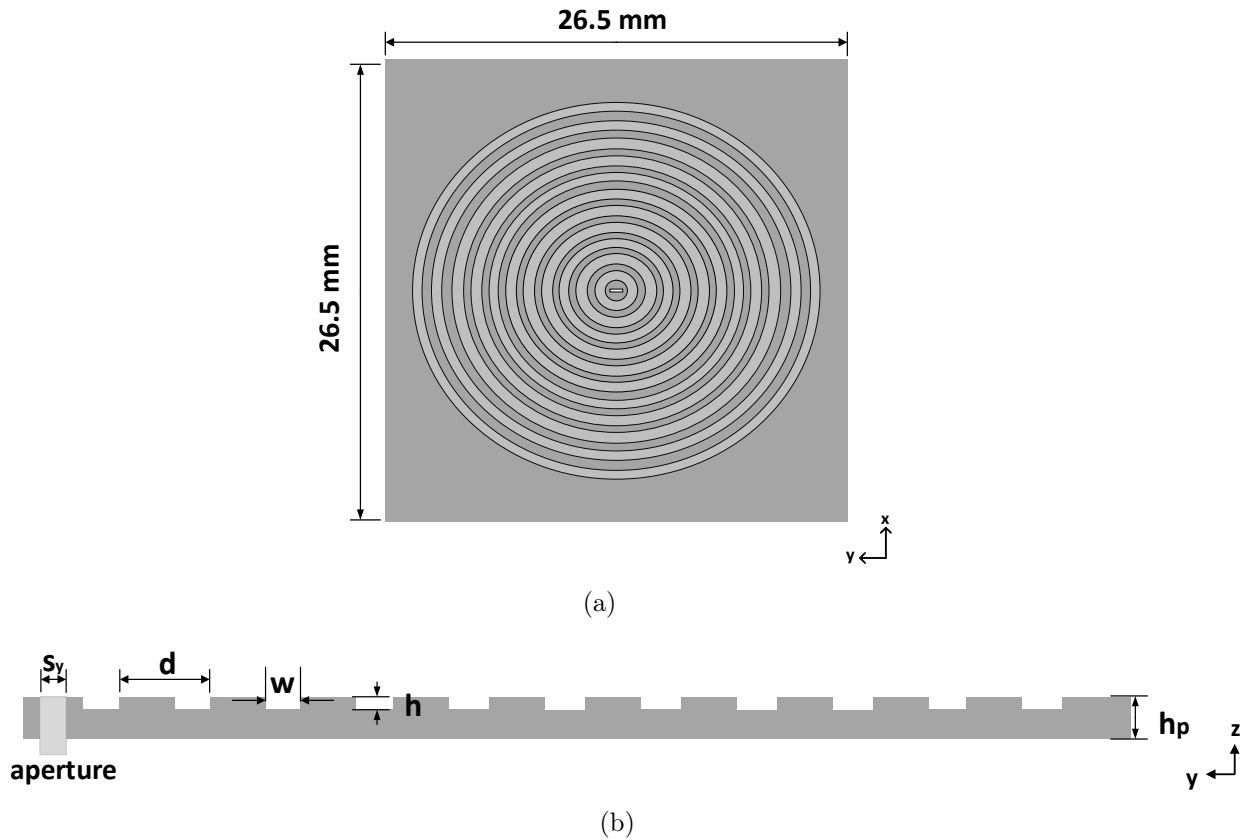


Figure 4.1: Bull's Eye antenna with slot aperture (a) Front view (b) Side view.

Fig. 4.2 demonstrates a simulated study for the antenna of Fig. 4.1 with varying number of rings. A significant enhancement in directivity is observed for a number of rings up to 12. After this size, the maximum achievable directivity reaches a saturation point, while the simulation time rises significantly. Therefore, 11 rings were chosen as a compromise between maximum directivity and minimum computational time.

The simulated matching performance, directivity and realized gain for the slot-fed antenna can be seen in Fig. 4.3. Although the performance is highly directive (23 dBi at 293 GHz), the maximum gain is 22 dBi at that frequency, and significantly smaller at slightly higher frequencies (by 2 to 5 dBi). This is attributed to the narrowband input matching, which is lower than -10 dB only in the frequency band between 273 GHz and 297 GHz. Ideally, the desired antenna performance would require a satisfactory matching

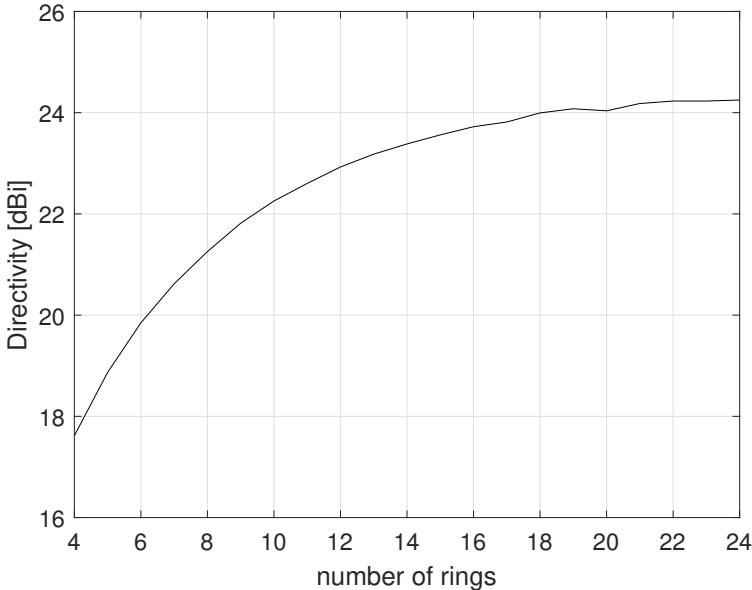


Figure 4.2: Simulation study for number of rings vs maximum directivity at around 300 GHz (feeding via a subwavelength slot).

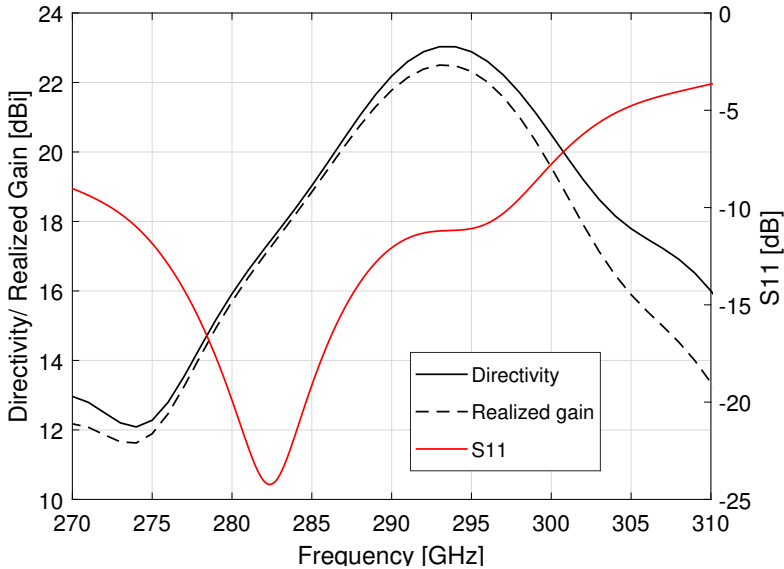


Figure 4.3: Simulated performance of Bull’s Eye antenna with slot aperture at around 300 GHz.

at the frequencies of maximum directivity.

Apart from the narrowband performance, the main drawbacks of a slot aperture are: (a) its dimensions always require a further optimization process in order to match the minimum S11 to the maximum directivity as close as possible and (b) due to its narrow width the fabrication can be very challenging at higher frequencies due to limitations of the fabrication tools. In order to enhance the input matching bandwidth and overcome the aforementioned problems, two novel aperture types are introduced in the following subsections.

4.1.2 The Open-Ended Waveguide Aperture

A novel open-ended waveguide aperture is examined as an alternative to the typical slot aperture. Its dimensions are the same as with the feeding waveguide (Fig. 4.4). For this particular application, it is w_{g_x} and w_{g_y} , same with the corresponding WR-3 waveguide dimensions. All other antenna dimensions and size remain the same as in Fig. 4.1.b.

The simulated performance of the waveguide-aperture antenna can be seen in Fig. 4.5. A waveguide aperture achieves a good input matching, below -10 dB, at all the frequencies between 270 GHz and 310 GHz. The maximum realized gain is 22.5 dBi at 294 GHz, same as the maximum directivity. This is due to the very broadband matching, which minimizes the input losses that are associated with gain. Also, due to the wider aperture dimensions, the fabrication process is much easier at high frequencies.

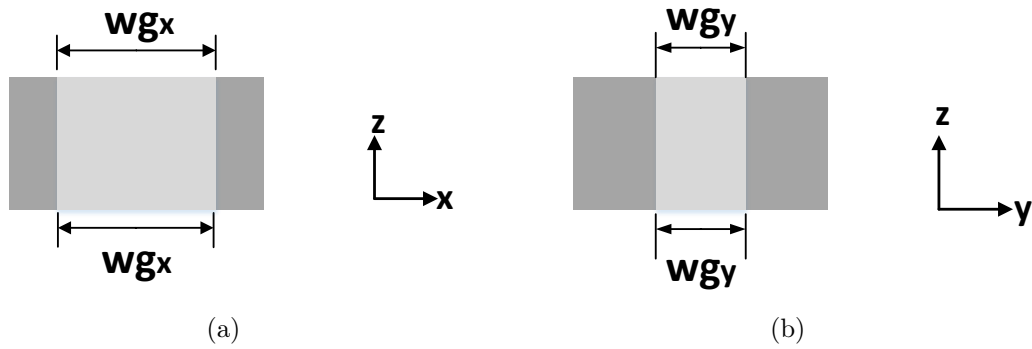
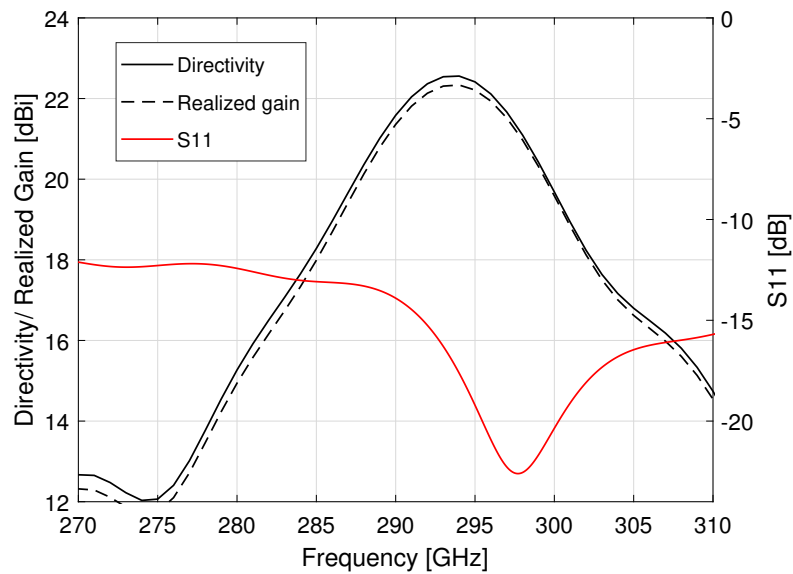

 Figure 4.4: Open-ended waveguide aperture design (a) xz plane, (b) yz plane.


Figure 4.5: Simulated performance of Bull's Eye antenna with open-ended waveguide aperture at around 300 GHz.

4.1.3 The Tapered Waveguide Aperture

A further improvement of the matching performance can be achieved via an outward tapering of the open-ended waveguide aperture of the previous Section. The aperture dimensions t_x and t_y are larger than the corresponding waveguide dimensions w_{gx} and w_{gy} by a factor r (Fig. 4.6). For this implementation $r = 1.3$ is set, or $t_x = 1.123$ mm and $t_y = 0.56$ mm.

The S11 parameters, directivity and realized gain of this antenna can be seen in Fig.

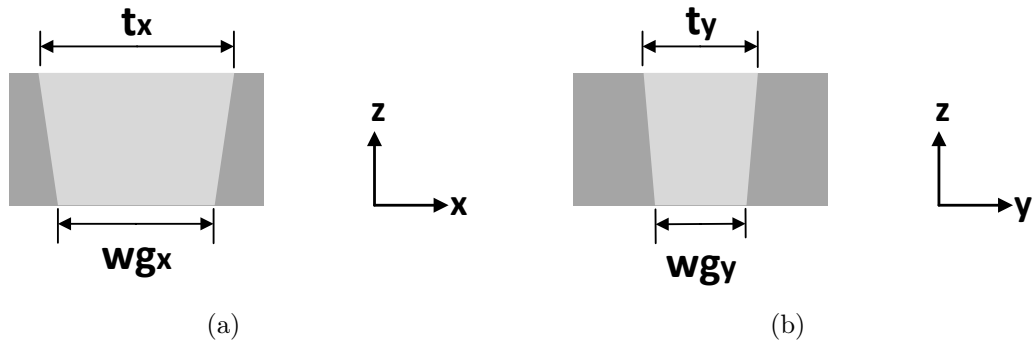


Figure 4.6: Tapered waveguide aperture design (a) xz plane, (b) yz plane.

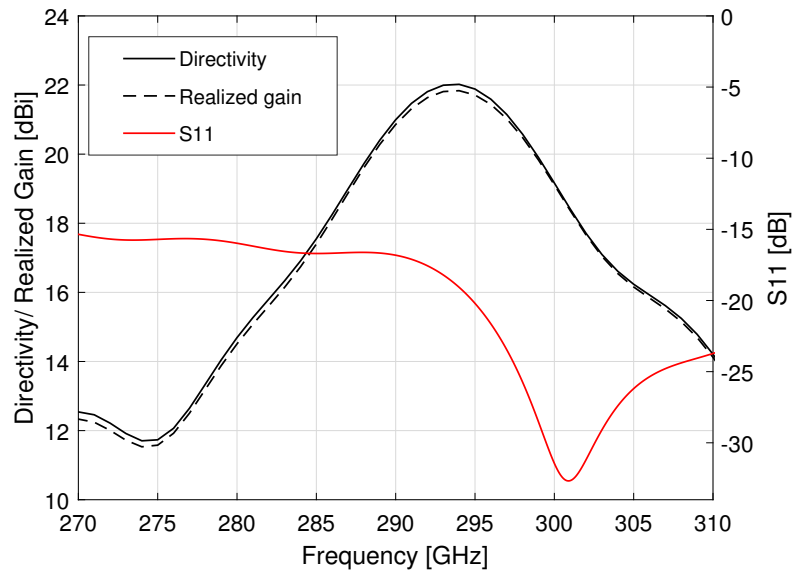


Figure 4.7: Simulated performance of Bull's Eye antenna with tapered waveguide aperture at around 300 GHz.

4.7. The tapered aperture provides an even better input matching performance (below -14 dB), while the nearly identical gain and directivity plots achieve a highly satisfactory performance. The peak values of directivity and gain are 22 dBi.

4.1.4 Comparison Between the Three Feeding Techniques

A comparison between three Bull's Eye antennas with the three different feeding techniques described earlier is presented below. The S11 performance of the three antennas

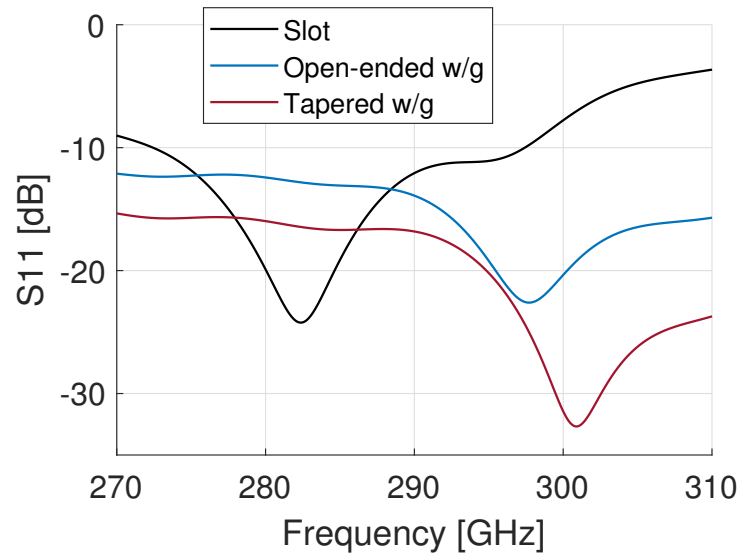


Figure 4.8: Simulated S11 comparison between three feeding aperture types on a bare ground plane at around 300 GHz.

of this Chapter is compared in Fig. 4.8. The tapered aperture antenna outperforms the other two in terms of matching bandwidth, at the cost of lower directivity and realized gain. The radiation characteristics of each antenna are summarized in Table 4.1. It seems that a reasonable compromise between a good input matching performance and a high gain can be achieved with a waveguide aperture implementation. The 3-dB gain bandwidth is similar in percentage for all feeding implementations. However, the broadband directivity antenna designs in later Chapters will require the broadband input matching feeding mechanisms developed in this Chapter.

The improvement in the S11 parameters is responsible for the nearly identical values of directivity and realized gain (Figs. 4.5 and 4.7), as well as the achievement of their peak value at the same frequency. The difference between maximum gain and maximum directivity is up to 0.7 dBi in the slot aperture realization 4.3, which is attributed to the borderline satisfactory S11 performance at the frequency of the maximum gain (around -10 dB) that decreases the realized gain.

Table 4.1: Far field performance comparison of the three antennas at 300 GHz.

	Max. directivity [dBi]	Max. realized gain [dBi]	3-dB gain bandwidth
Slot	23	22.5	4.78 %
Open-ended w/g	22.5	22.3	4.42 %
Tapered w/g	22	21.8	4.42 %

The main disadvantage of the tapered waveguide aperture is that it requires a large central ring. In most implementations, the diameter of the central ring is usually set at around λ_0 [1, 2]. A larger central ring reduces the achievable maximum directivity, therefore there are limitations in the outward tapering factor of the waveguide.

The previously presented results can be better understood if we take into account the directivity of each single aperture alone on a ground plane, without the corrugated texture (Fig. 4.9). The single tapered aperture directivity is about 1.5 dBi higher than the open ended waveguide directivity which in turn is higher than the slot directivity. It is evident that a small part of this difference in the directivity and gain of the primary feeds is maintained in the overall Bull's eye antenna directivity values.

The radiation patterns for the H - and E -planes of the antenna are shown in Fig. 4.10, for the three feeding cases. The comparison is at the selected frequency points that define the 3-dB gain bandwidth of each antenna.

E -planes exhibit a more directive main lobe compared to the H -plane radiation patterns, but with more rippled side lobes. Referring to the H -plane at the frequency of maximum gain (Fig. 4.10.d), the slot aperture antenna has about 3.5 dBi lower side lobes than the tapered aperture antenna at angles around $\pm 20^\circ$, and only 2 dBi lower side lobe level than the waveguide aperture antenna. At the upper frequency of the 3-dB spectrum, the difference between the slot aperture and the tapered aperture is only 2.5

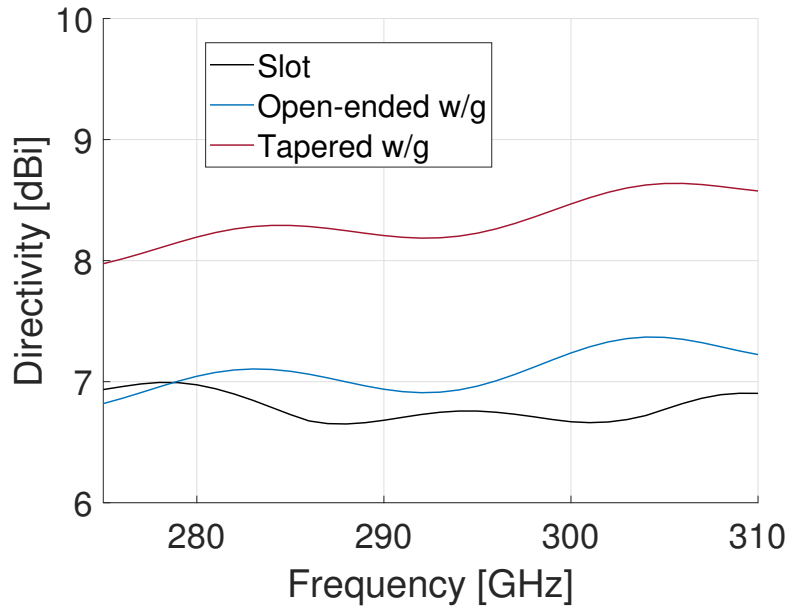


Figure 4.9: Simulated directivity comparison between three feeding aperture types on a bare ground plane at 300 GHz.

dBi around $\pm 20^\circ$, regarding the H -plane (Fig. 4.10.f). At angles $\pm 60^\circ$ at H -plane, the tapered aperture antenna performs better. All three antennas exhibit identical E -plane radiation patterns at angles larger than than 60° . At the frequency limits of the 3-dB gain bandwidth, the side lobes become higher in magnitude in both planes, as expected.

As verified from leaky wave theory, at frequencies inside the 3-dB gain spectrum, the radiation patterns exhibit a single directive beam, which is the superposition of two beams, each one deriving in phase from each half of the periodic structure (around the central aperture). At frequencies outside the 3-dB spectrum, where the operating wavelength becomes significantly smaller or bigger than the periodicity, the radiation patterns consist of two beams (split-beam effect).

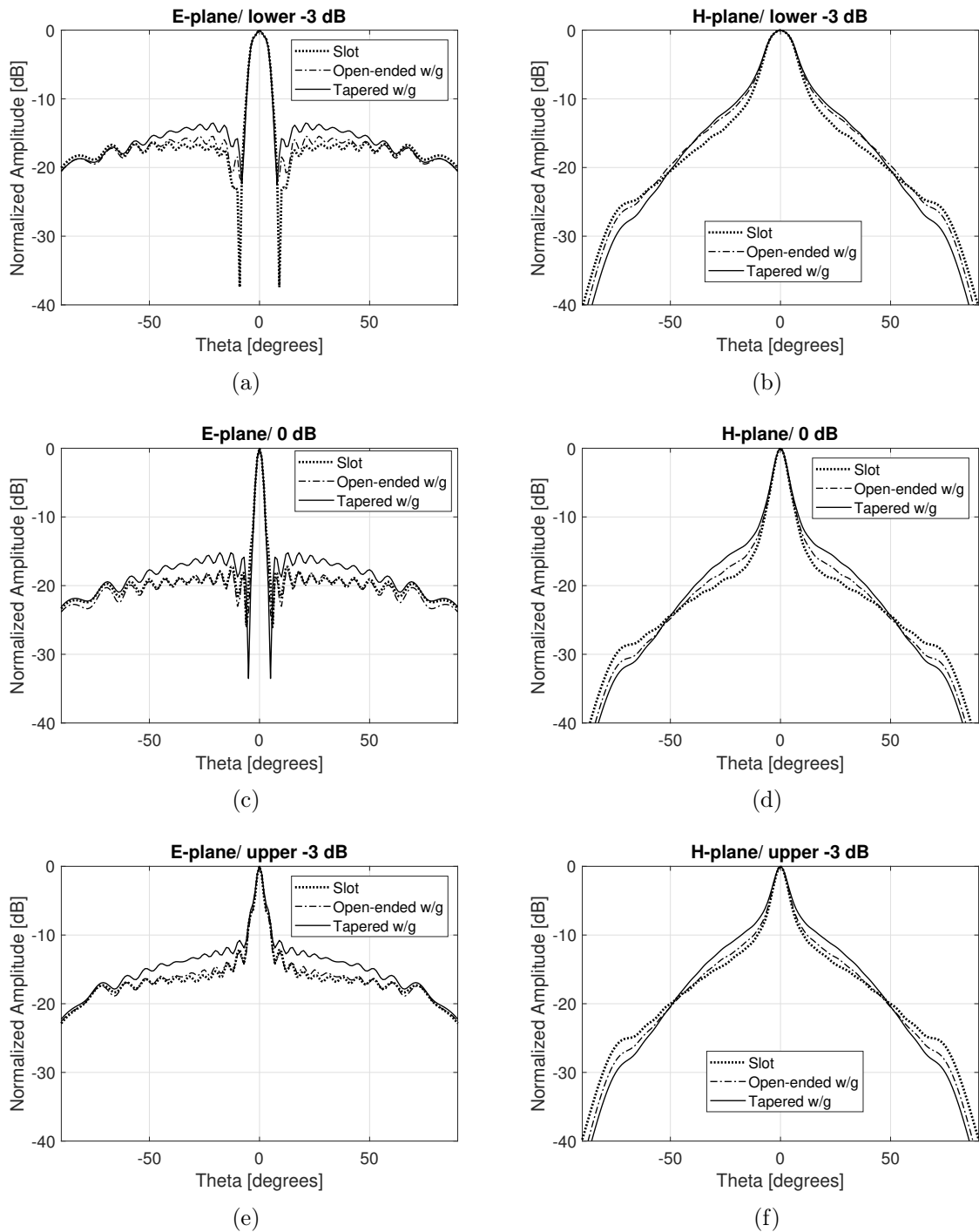


Figure 4.10: Comparison of simulated radiation patterns at various frequencies of interest for the three types of Bull's Eye antennas. *E*-plane (a) lower -3 dB, (c) 0 dB, (e) upper -3 dB. *H*-plane (b) lower -3 dB, (d) 0 dB, (f) upper -3 dB.

4.2 Fabricated Prototype of 300 GHz Bull's Eye with Tapered Aperture

The tapered aperture Bull's Eye antenna of Section 4.1.3 was fabricated at the University of Birmingham with CNC milling. A split-block technique was implemented for the challenging fabrication of this antenna. The metal body was cut in two halves symmetrically across the E -plane of the waveguide, which is the best suggested way to split a waveguide so as not to disturb the radiating fields. Also, in order to fit the threads of the waveguide flange inside the metal plane, the thickness of the ground plane was extended to 7 mm. Such an extension, after simulations, did not affect the overall performance of the antenna. A picture of the manufactured antenna is shown in Fig. 4.11.

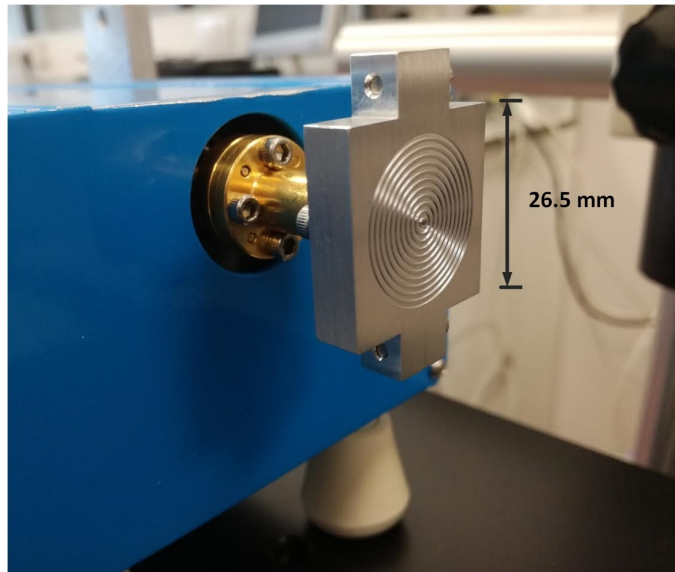


Figure 4.11: Fabricated prototype of the tapered Bull's Eye antenna at 300 GHz.

The antenna was measured with a Vector Network Analyzer and two reference horn antennas of 16 dBi gain, fed by a WR-3 waveguide, and bandwidth from 282 GHz to 298 GHz. It should be noted that the Fraunhofer limit for this Bull's Eye antenna was calculated around 0.2 m, from the known formula $2D^2/\lambda_0$, where D is the maximum

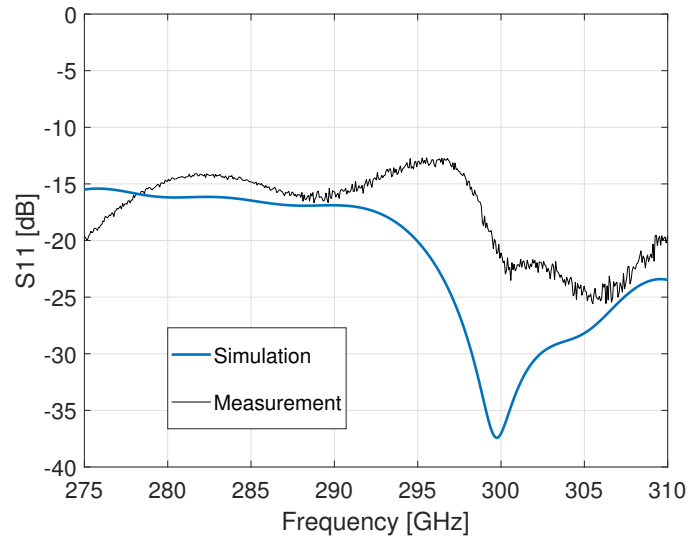


Figure 4.12: Measured S11 of the tapered Bull's Eye antenna compared to simulated.

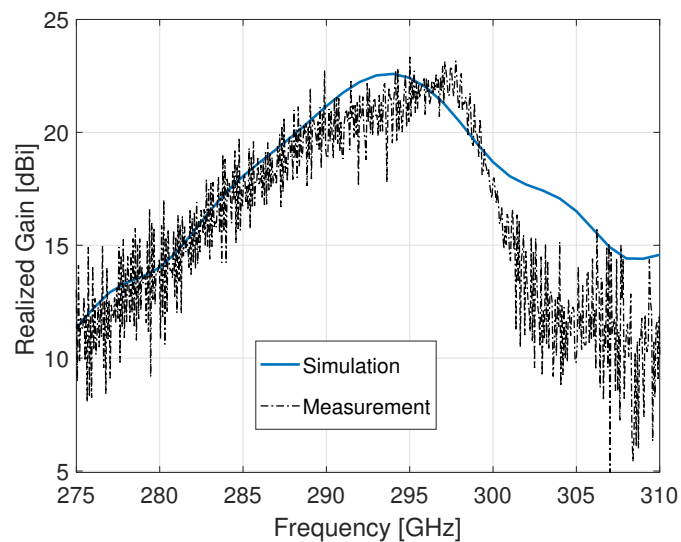


Figure 4.13: Measured realized gain of the tapered Bull's Eye antenna compared to simulated.

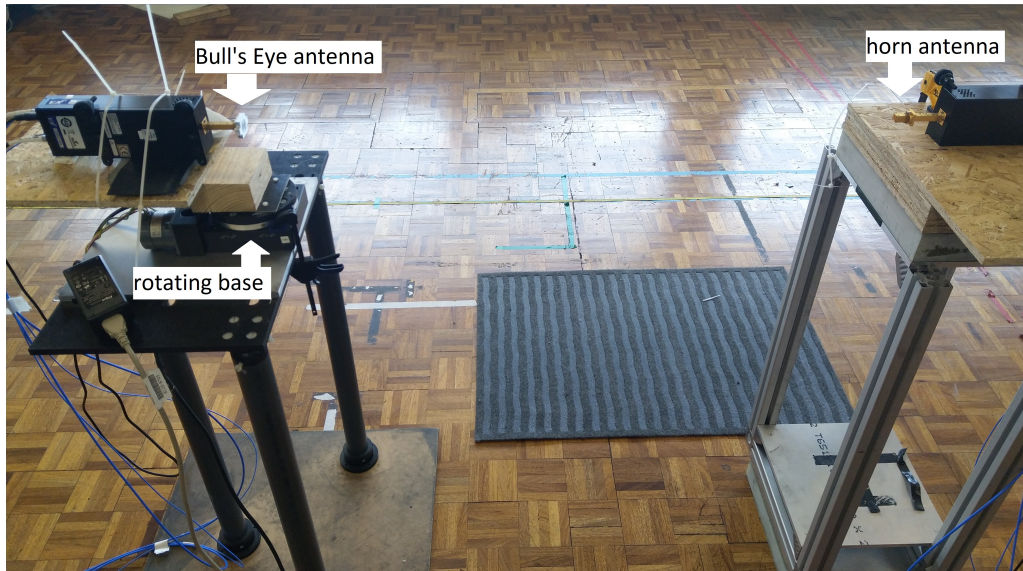


Figure 4.14: Setup for radiation pattern measurement at 300 GHz.

diameter of the antenna. In this case, as D was considered the diameter of the outer indented ring. The realized gain and radiation pattern measurements were conducted with the two-antenna method, as explained in [3].

The measured S_{11} parameters and realized gain in comparison with the simulated ones can be seen in Figs. 4.12 and 4.13. Overall, a very good agreement between simulation and measurement can be observed. The measured input matching is way below the limit of -10 dB, while the maximum realized gain reaches 22 dBi at 298.5 GHz. A shift is observed by 3.5 GHz at the maximum frequency, which also affects the 3-dB bandwidth of the antenna. The ripple is attributed to the faulty port of the VNA used at the time for the measurement. For the measured antenna, this bandwidth is approximately from 289 GHz to 300 GHz.

A rotating base was used in order to measure the radiation patterns of the antenna. The setup of Fig. 4.14 was used for the radiation pattern measurement. Only the H planes of the Bull's Eye antenna were measured, due to difficulties to align the E -planes

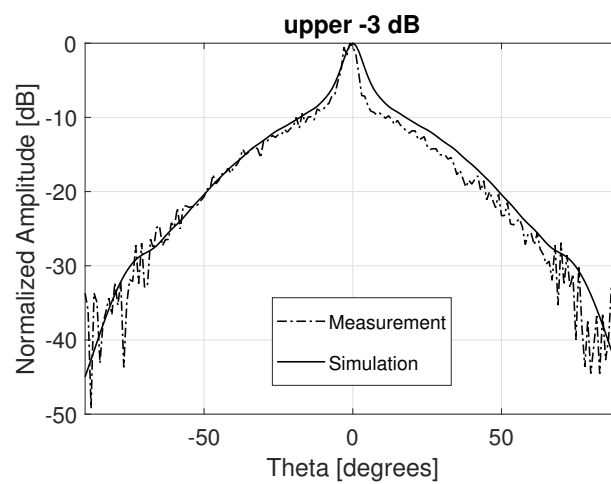
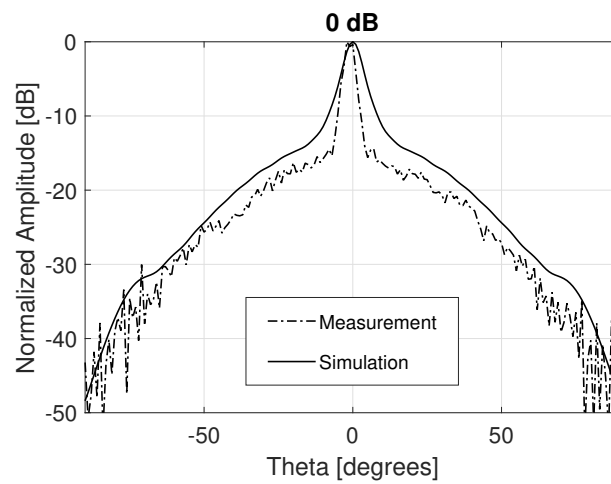
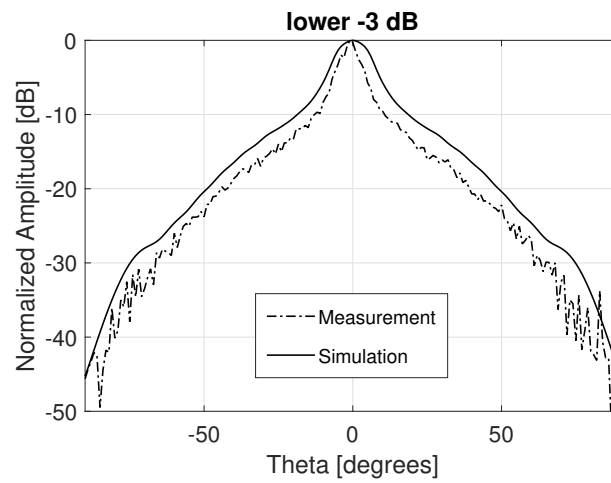


Figure 4.15: Normalized H -plane measurements of the tapered Bull's Eye antenna compared to simulated, at (a) lower -3 dB, (b) 0 dB, (c) upper -3 dB.

both the antennas with the facilities available at the time. The antenna was scanned from -90° to $+90^\circ$ with a step of 1° . The Bull's Eye antenna and the 300 GHz horn antenna were placed at a farfield distance of nearly 1 m.

Since from the measured gain plot of Fig. 4.13 a shift at the frequency of maximum gain was noticed, it is reasonable to compare measured and simulated patterns between the corresponding frequencies at 3-dB band. The measured H -plane pattern of 298.5 GHz, which is the measured frequency of the measured maximum gain, is compared to the simulated H -plane pattern at 296 GHz. Fig. 4.15 shows the measured versus the simulated patterns within the 3-dB gain spectrum.

A good agreement between measurement and simulation is observed. In fact, the measured H -planes exhibit a lower side lobe level than simulations, even up to -5 dB lower at specific angles. A very small misalignment of 0.5° or 1° is present, however it should be noted that the alignment between the phase centers of the two antennas is very difficult at these frequencies. Any other discrepancies can be attributed to fabrication process inaccuracies that have a significant effect in this frequency band.

A fabricated prototype of a Bull's Eye antenna with tapered waveguide aperture operating at the Ku band was fabricated and measured. The measured results are available in Appendix A.

4.3 Conclusion

In this Chapter, two novel feeding techniques, the open-ended waveguide aperture and the tapered waveguide aperture, have been presented as an alternative to the typical slot aperture. The purpose of introducing these two novel aperture types is to enhance the

input matching performance of the antenna, and maintain a satisfactory performance across the operating frequency band. In particular, for the presented Bull's Eye antenna designs at around 300 GHz, the open-ended waveguide aperture achieves S11 values below -10 dB, and the tapered waveguide aperture achieves an S11 below -15 dB.

Since the novel feeding aperture designs are directly scalable from the microwave to the low THz frequencies, their fabrication process is facilitated, especially towards higher frequencies, where the limitations of the fabrication tools introduce constraints related to the machining of subwavelength parts (namely, a slot aperture). Also, with the use of an open or a tapered waveguide aperture any optimization process is avoided, a necessary step when designing a slot aperture, due to their straightforward design guidelines. These advantages are demonstrated with the presented measured results of a fabricated prototype at 300 GHz, which are in very good agreement with simulations.

In the following Chapters, the significance of these results will be demonstrated in applications where the S11 parameters need to be below -10 dB across a wide bandwidth, due to the special broadband design of the Bull's Eye antenna which affects the achievable matching bandwidth.

References

- [1] M. Beruete, I. Campillo, J. S. Dolado, E. Perea, F. Falcone, and M. Sorolla, "Dual-Band Low-Profile Corrugated Feeder Antenna," *IEEE Trans. Antennas Propag.*, vol. 54, no. 2, pp. 340–350, 2006

- [2] M. Beruete, U. Beaskoetxea, T. Akalin, "Flat Corrugated and Bull's-Eye Antennas", in *Aperture Antennas for Millimeter and Sub-Millimeter Wave Applications*, Springer, 2018

- [3] C. A. Balanis, "Antenna Theory: Analysis and Design", 2nd ed., *New York: Wiley*, 1997.

Chapter 5

Dual-depth corrugations for broadband Bull's Eye antennas

Most cited corrugated antenna implementations have mainly exploited the periodicity d of the indented rings for the determination of the operational bandwidth, where it should be $d \approx \lambda_0$ for an optimum transmission of power [1, 2]. A modulation in the shape of corrugations [3], the width of the gaps [4], or even the superposition of corrugated planes in a multilayer configuration [5], are some of the procedures suggested in literature for the expansion of gain bandwidth. Although the antenna aperture efficiency has been enhanced in [4] and a dual band operation has been achieved in [5], a remarkable enhancement of the 3-dB gain bandwidth performance of such antennas has not been realized thus far.

It has been noted briefly in Chapter 2 that for a certain value of d , the depth h of the corrugations can determine the resonant frequency. This effect has been exploited for only a few applications so far [6]. In this Chapter, a new design is proposed that employs two different corrugation depth values and aims at the enhancement of the typically limited

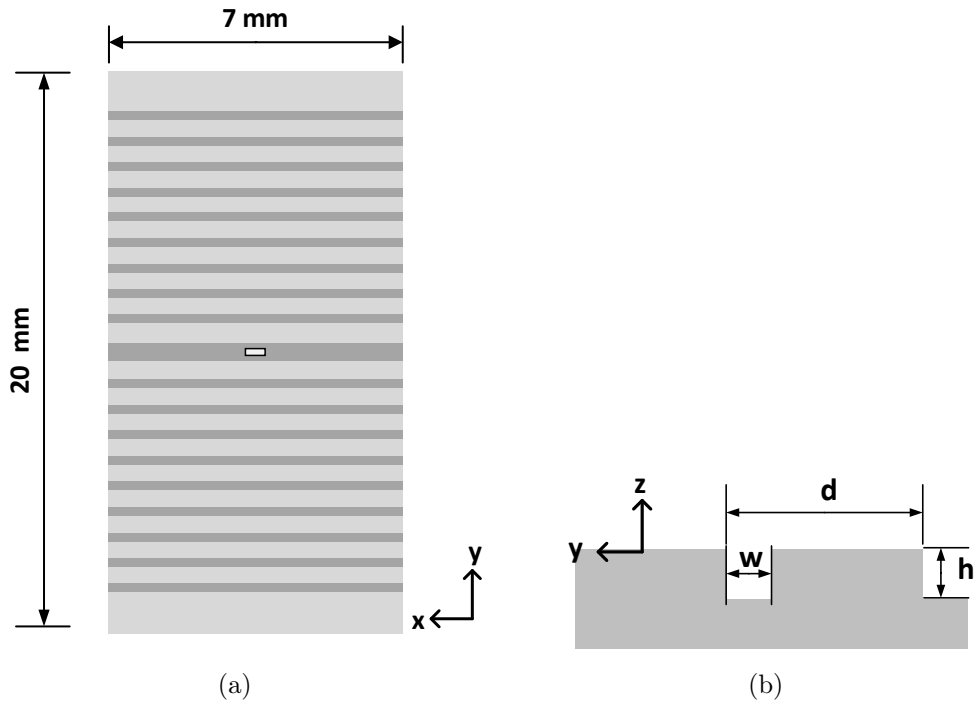


Figure 5.1: 1-D corrugated metallic antenna at 300 GHz (a) Front view of antenna (b) Unit cell.

3-dB gain bandwidth of such antennas. The proposed optimum model of 10 rings at 300 GHz delivers a 3-dB gain bandwidth of 8.85%, which is the best reported so far for this type of corrugated antennas of the same size. The study is performed for an antenna at the low-THz spectrum, around 300 GHz, in order to demonstrate the scalability of this technique to such high frequencies, where the fabrication of prototypes can be challenging. A leaky wave analysis of this novel design is performed, with the use of the novel analytical periodic method of Section 3.2. A prototype of this design was fabricated. Measurements show very good agreement with the simulated model which has been slightly redesigned in order to account for the fabrication tolerances.

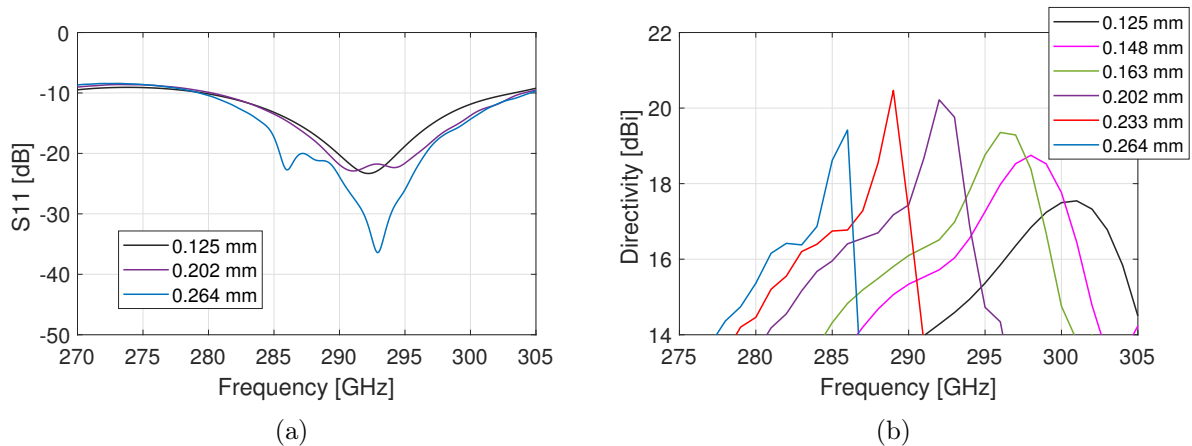


Figure 5.2: Simulated effect of depth h on the 1-D corrugated antenna of Fig. 5.1 with (a) S_{11} (b) Directivity.

5.1 Effect of corrugations' depth h

One of the corrugated metal plate design parameters is the depth h of the corrugations, which is required to be smaller than $\lambda_0/4$ and frequency dependent as in

$$h \approx \frac{(2n + 1)\lambda_0}{4} \quad (5.1)$$

where n is a non-negative integer and λ_0 is the free space wavelength (Fig. 5.1).

An experimental demonstration of the effect of corrugations' depth on the far field antenna performance is presented here. The reference antenna is a one-dimensional corrugated metallic surface as in Fig. 5.1. The antenna is excited via a subwavelength slot aperture, fed by a WR-3 waveguide for operation around 300 GHz. It consists of 10 unit cells at each side of the aperture. The optimized design details of Fig. 5.1 are $d = 0.96$ mm, $w = 0.61$ mm and the depth h of the corrugations is a variable inserted to the parametric sweep analysis. The half wavelength slot is 0.584 mm \times 0.159 mm wide.

A parametric study around h has been performed via CST Microwave Studio, with d

and w fixed. Fig. 5.2 shows the effect of depth h in S11 and directivity. The maximum limit of the parametric sweep of h is around $\lambda_0/4$, which is the upper limit when the TM surface mode is supported, based on the analytical theory of Chapter 2, and the corrugated surface remains of high impedance. For values of h around $\lambda_0/5$ the directivity is over 20 dBi. However, for smaller values of h (around $\lambda_0/10$), the antenna is more broadband in terms of gain-bandwidth than it is for large h and same maximum directivity. For example, for $h = 0.148$ mm the 3-dB gain bandwidth of the antenna is 12 GHz, while for $h = 0.264$ mm the 3-dB gain bandwidth is only 4 GHz.

The matching bandwidth of the antenna remains relatively unchanged for various depths h (Fig. 5.2.a). This can be attributed to the fact that the S11 bandwidth is mainly determined by the feeding slot mechanism and the selection of the slot's dimensions. The addition of the corrugated texture excites the radiating leaky mode, as explained in Chapters 2 and 3, and determines the farfield characteristics of the antenna, which are effectively described by figures such as gain/directivity.

These findings could be extended to the planar corrugated design (Bull's Eye antenna).

5.2 The Dual-Depth Concept

A 3-dB gain (directivity) bandwidth enhancement technique is proposed in this Section that takes advantage of the depth qualities of the corrugations, by employing different values of h for different sets of rings. The novel design consists of a number of rings N , with periodicity d (Fig. 5.3). While keeping d constant, a parametric sweep is conducted only for the depth h of the corrugations. The first $N/2$ unit cells are designed to operate at a frequency f_1 corresponding to the depth h_1 and the next $N/2$ unit cells are designed

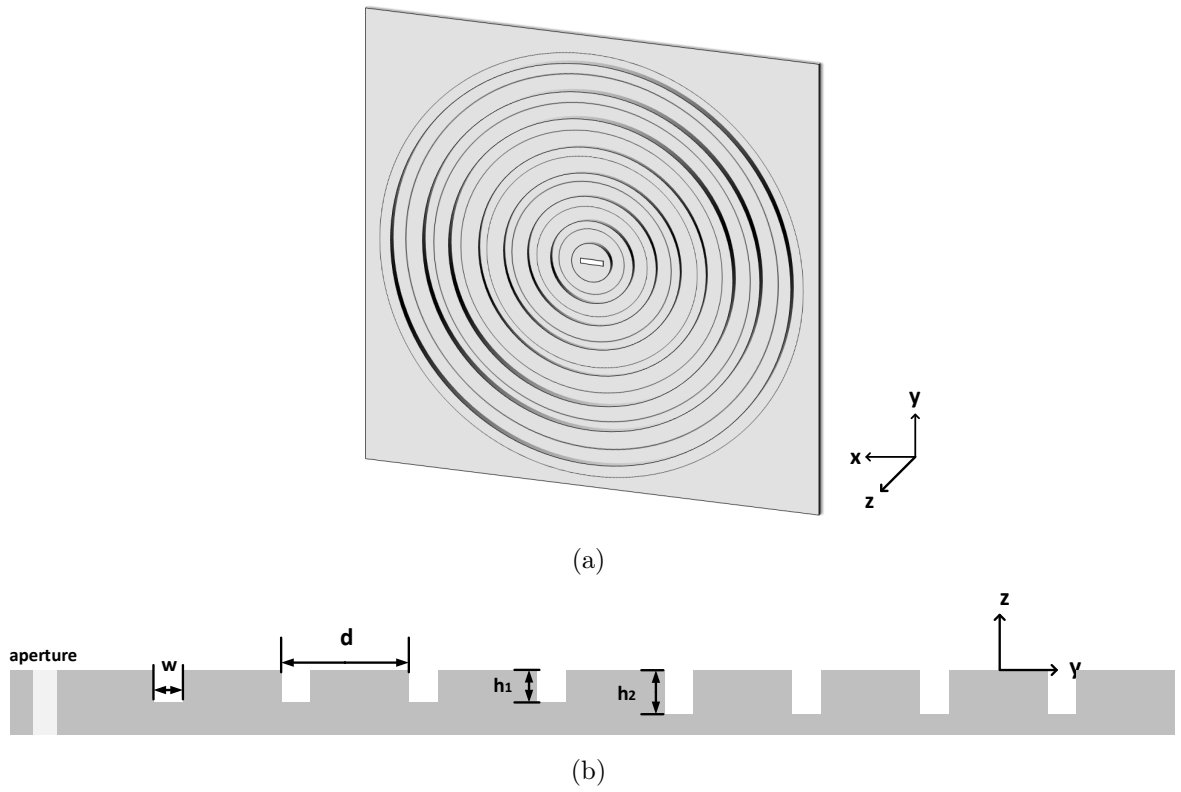


Figure 5.3: Schematic of the dual-depth Bull's Eye antenna with $N = 8$ (a) perspective (b) profile.

to operate at a frequency f_2 corresponding to the depth h_2 .

The design process of this bandwidth enhancement technique can be viewed in the simulation results of Figs. 5.4 and 5.5. The design details of the simulated antennas are the same as in the previous, while keeping h_1 constant and varying h_2 . The comparison is between the single depth antennas h_1 and h_2 of the same size ($N = 10$). The central ring around the aperture has a radius of 1.05 mm ($\sim \lambda_0$). The overall size of all antennas is 25 x 25 mm². The terms " h_1 " and " h_2 " denote the single depth antennas of corresponding depth, and " $h_1 + h_2$ " denotes the dual-depth antenna.

Two peaks are observed in the directivity plot of the dual depth antenna (Fig. 5.5). When the h_1 and h_2 values are selected in proximity, the 3-dB gain bandwidth does not cover the area around the smaller peak yet, which is generated by the set of rings with h_2 .

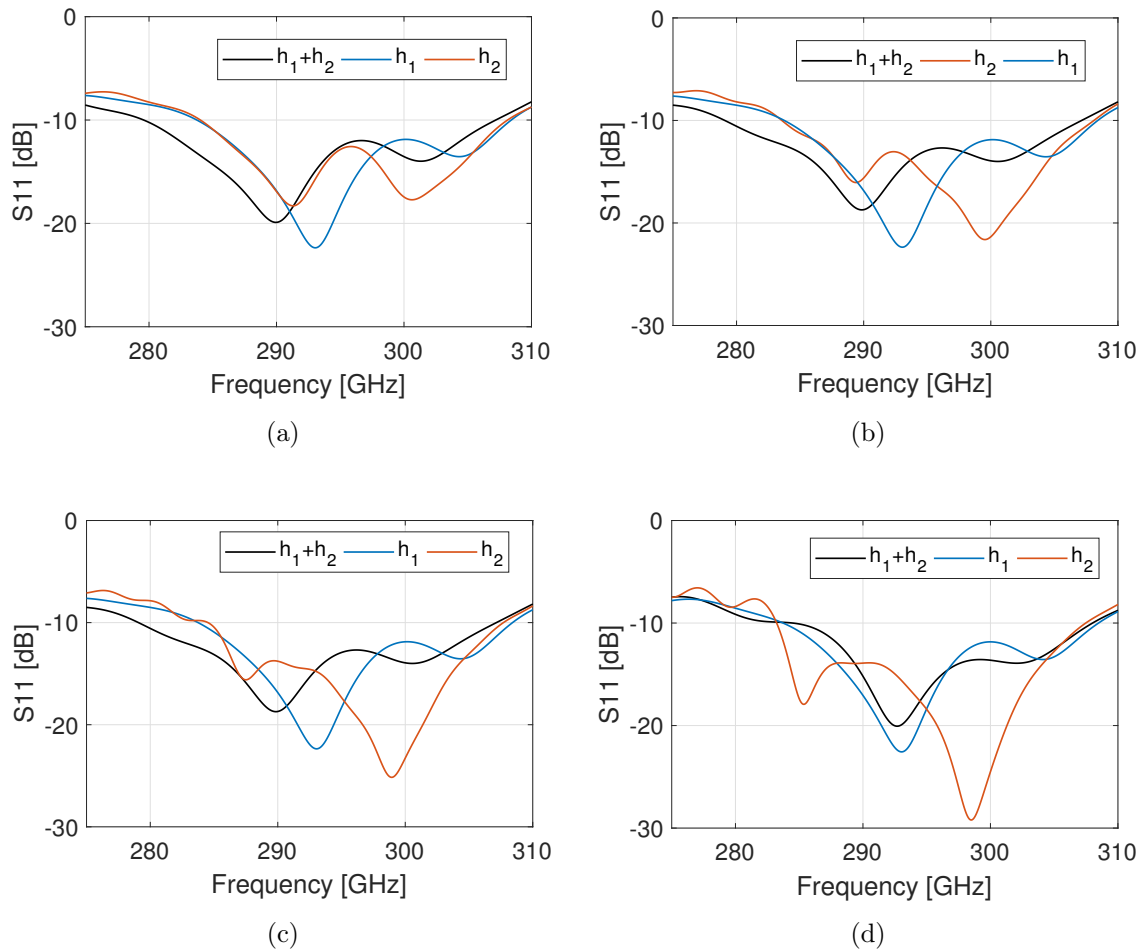


Figure 5.4: Simulated S11 of Bull's Eye antennas of $N = 10$ for different sets of h_1, h_2 (a) (0.14 mm, 0.18 mm), (b) (0.14 mm, 0.21 mm), (c) (0.14 mm, 0.24 mm), (d) (0.14 mm, 0.266 mm).

The maximum directivity of the dual depth design is lower as h_2 obtains larger values, with the advantage of increasing the bandwidth around the zone of h_2 . When h_1 and h_2 values are sufficiently far apart, the 3-dB gain bandwidth covers both zones around the two peaks. The optimum model is shown in Figs.5.4.d and 5.5.d, where h_1 and h_2 are reasonably different, and h_2 reaches the limit of $\lambda_0/4$ at around 300 GHz, as suggested by the known design parameters for corrugated metallic planes and relative theory. The S11 bandwidth remains relatively unaffected when two depths are employed instead of one (Fig. 5.4).

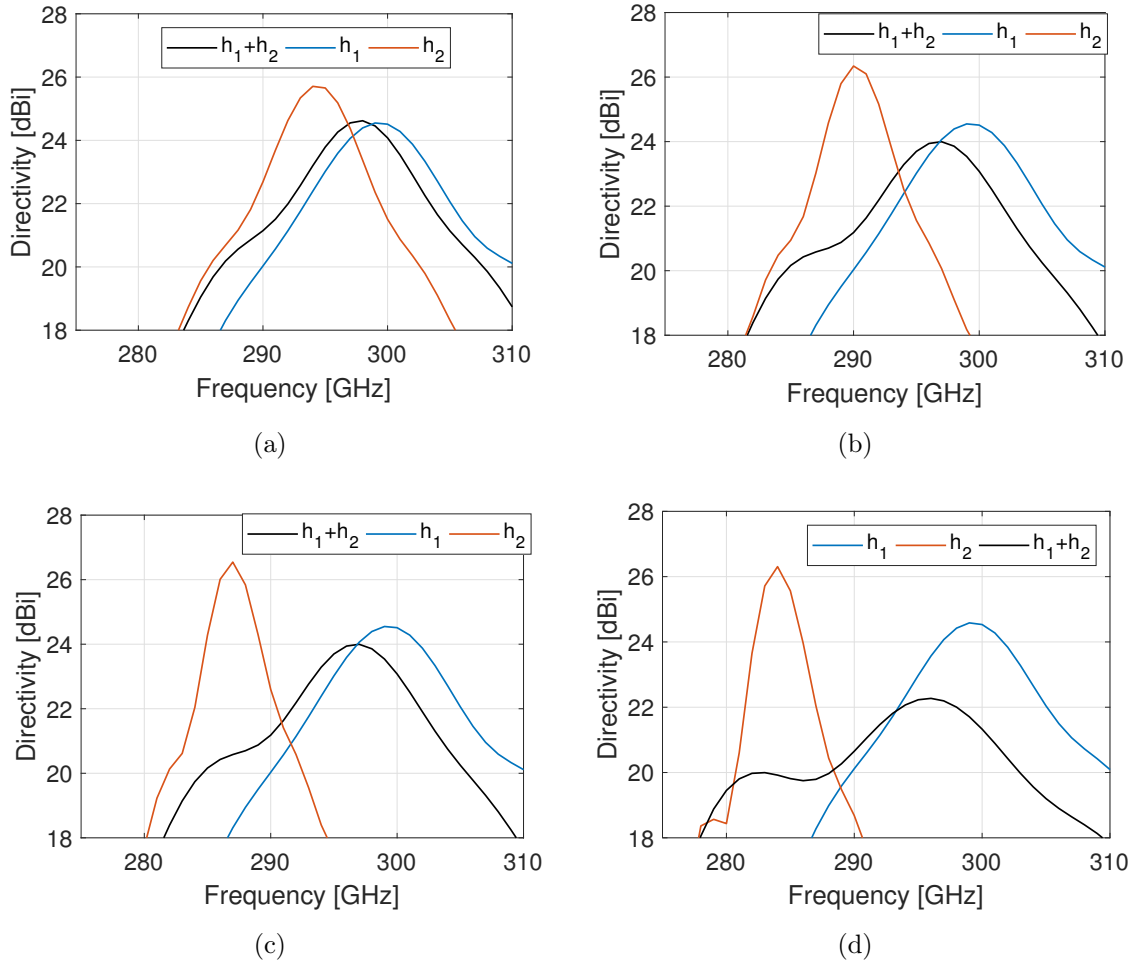


Figure 5.5: Simulated directivity of Bull's Eye antennas of $N = 10$ for different sets of h_1, h_2 (a) (0.14 mm, 0.18 mm), (b) (0.14 mm, 0.21 mm), (c) (0.14 mm, 0.24 mm), (d) (0.14 mm, 0.266 mm).

A simulation was performed for the case when $h_1 > h_2$ or, equivalently, when the first set of unit cells operates at the lower frequency. For the case of $(h_1, h_2) = (0.24 \text{ mm}, 0.14 \text{ mm})$ the S11 and directivity plot is shown in Fig. 5.6. The output performance is not towards the goal of bandwidth enhancement, rather than an average between the two antenna performances h_1 and h_2 . Therefore, for an effective transmission of this proposed dual-depth design, it is compulsory that $h_1 > h_2$.

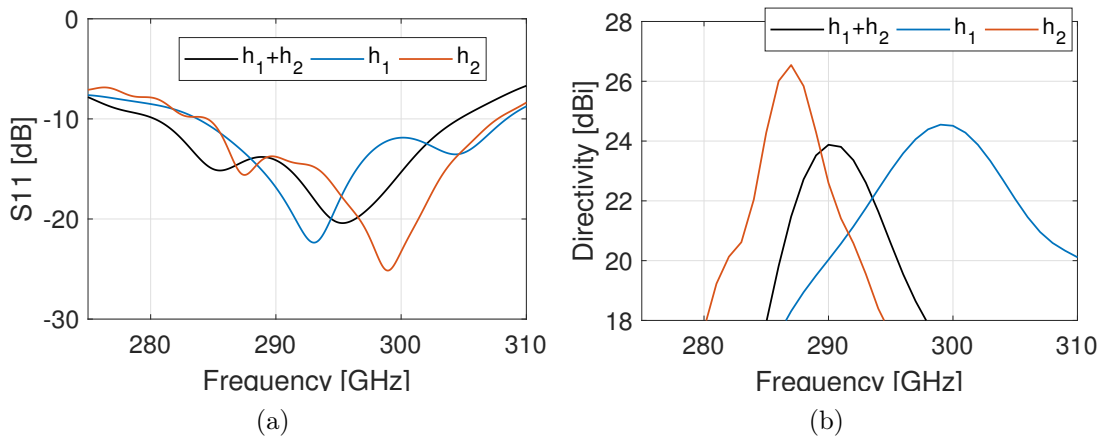


Figure 5.6: Simulated (a) S_{11} and (b) directivity of Bull's Eye antennas of $N = 10$ for $(h_1, h_2) = (0.24 \text{ mm}, 0.14 \text{ mm})$.

5.2.1 Optimized Slot-Fed Dual-Depth Bull's Eye Antenna

It is of high interest to examine depth values h_1 and h_2 that are reasonably far apart and achieve the similar maximum directivity for the same size, therefore the optimum design of Figs. 5.4.d and 5.5.d is investigated in this Section.

Since at least 4 or 5 periods are required for the leaky wave phenomenon to take effect, only designs of $N \geq 8$ are designed and simulated (at least 4 unit cells for each depth h_1 or h_2). For a thorough examination of the optimum dual-depth design, different antenna sizes are examined ($N = 8, 10, 12$, where N is the number of rings). Tables 5.1-5.3 summarize the simulation results for each N size dual-depth antenna. The comparison is only between the dual-depth antenna and the single h_1 antenna, since the latter is more broadband than the antenna of h_2 (Fig. 5.2). The fourth column of each Table refers to the *gain-bandwidth product (GBWP)*, which is a figure of merit that summarizes the overall performance of the antenna in terms of gain and bandwidth.

Tables 5.1-5.3 exhibit the same trends. The dual-depth antenna of N rings achieves the same 3-dB gain bandwidth with the h_1 antenna of $N/2$ rings, with a relative enhancement

Table 5.1: Slot-fed dual-depth Bull's Eye antenna with $N=8$ at around 300 GHz.

	N	3-dB BW [GHz]	Max. Dir [dBi]	GBWP
	4	40	18.57	2410
h_1	6	21.5	21.4	2707
	8	16.3	23.37	3099
$h_1 + h_2$	8	26.75	21.58	3486

 Table 5.2: Slot-fed dual-depth Bull's Eye antenna with $N=10$ at around 300 GHz.

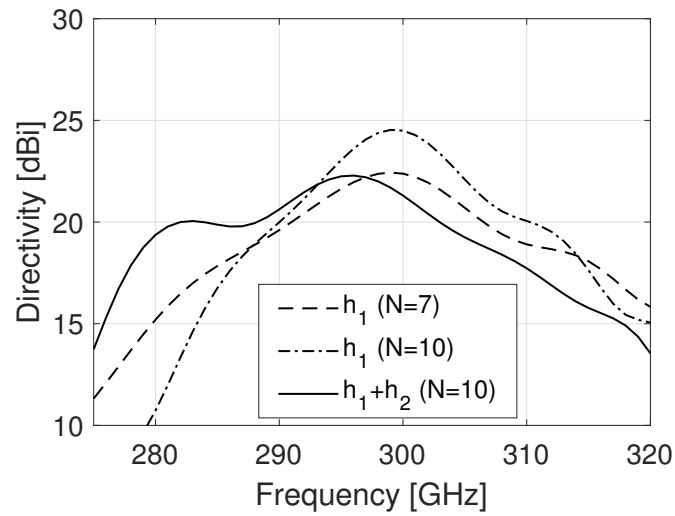
	N	3-dB BW [GHz]	Max. Dir [dBi]	GBWP
	5	24.5	20.1	2329
h_1	7	18.5	22.4	2905
	10	13	24.5	3303
$h_1 + h_2$	10	25	22.3	3908

in maximum directivity by 3.4 dBi ($N = 8$), 2.2 dBi ($N = 10$) and 1.8 dBi ($N = 12$). The case of a h_1 antenna with 4 rings is of a rather low simulated maximum directivity, so discussion is trivial for this case. Also, the dual-depth antenna achieves 10 to 12 GHz extra 3-dB bandwidth, compared to a single depth h_1 antenna of the same size N . This trend is observed however only for dual-depth designs of up to $N=12$. Simulations showed that dual-depth antenna sizes with $N > 12$ return to the typical gain performance of the single depth h_1 antennas of the same size.

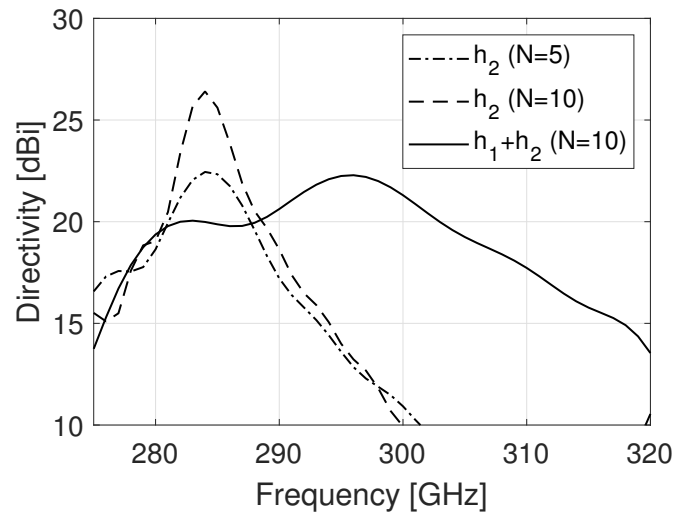
Moreover, the dual-depth design is between 5 to 6.5 GHz more broadband than a single depth h_1 antenna of the same maximum directivity. In particular, the dual depth design is 1.7% ($N = 8$), 1.9% ($N = 10$) and 0.9% ($N = 12$) more broadband than the h_1 antenna of the same maximum directivity. The GBWP results show that the dual-depth antenna, overall, performs most effectively, compared to the single depth implementations.

 Table 5.3: Slot-fed dual-depth Bull's Eye antenna with $N=12$ at around 300 GHz.

	N	3-dB BW [GHz]	Max. Dir [dBi]	GBWP
	6	21.5	21.4	2707
h_1	8	16.3	23.27	3099
	12	11	25.5	3399
$h_1 + h_2$	12	21.32	23.48	4157



(a)



(b)

Figure 5.7: Comparison between three slot-fed Bull's Eye antennas (simulation results). The dual-depth antenna is compared with (a) the h_1 antenna and (b) the h_2 antenna.

The aforementioned contributions of this design can be viewed in the simulated results of Fig. 5.7. The dual-depth antenna is compared with single depth antennas h_1 and h_2 of the same maximum size and the same maximum directivity. The dual-depth design (h_1+h_2) achieves a 3-dB gain bandwidth that is extended approximately between the lower limit of the 3-dB bandwidth of the h_2 antenna and the upper limit of the h_1 antenna. While the matching bandwidth remains relatively unaffected, the directivity plot of the dual-

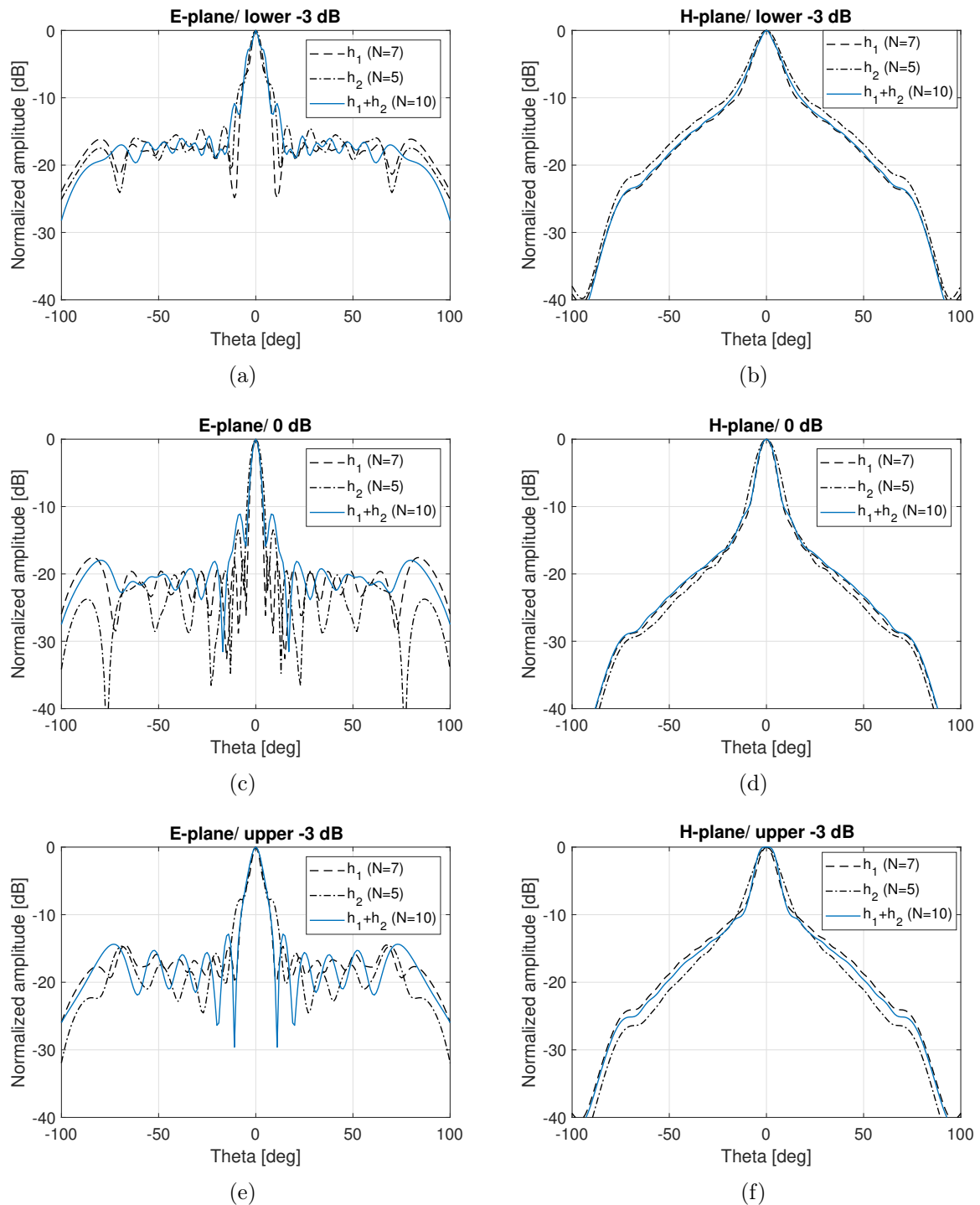


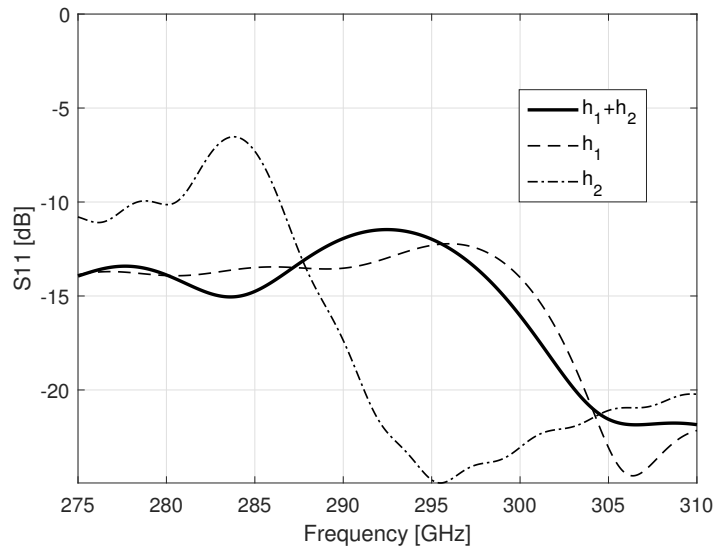
Figure 5.8: Simulated E - and H - planes at the 3-dB spectrum of the dual-depth and the single depth antennas of the same maximum directivity. E -plane: (a) lower -3 dB, (c) 0 dB, (e) upper -3 dB. H -plane: (b) lower -3 dB, (d) 0 dB, (f) upper -3 dB.

depth antenna shows clearly two peaks at two discrete frequency zones which correspond to each depth value. The maximum directivity of 22.2 dBi is observed at 296 GHz (while the maximum of the h_1 antenna is at 299 GHz). and the second peak of 20 dBi is at 282 GHz (while the maximum of the h_2 design is at 284 GHz). The 3-dB gain bandwidth of this novel design is 25 GHz, or 8.6%, and it covers the frequencies from the lower 3-dB limit of the h_2 antenna until the upper 3-dB limit of the h_1 antenna.

The simulated radiation patterns across the 3-dB gain bandwidth are available in Fig. 5.8. The $N = 10$ dual-depth antenna is compared with the single depth (h_1 and h_2) antennas of the same maximum directivity. At the lowest frequency of the 3-dB spectrum, both farfield planes of the dual-depth antenna are very similar with these of the single h_2 antenna. At the frequencies of 0 dB, upper -3 dB, the dual-depth antenna exhibits similar patterns with the h_1 antenna. At angles around $\pm 20^\circ$ the E -planes of the dual-depth antenna exhibit high side lobes, which is the contribution of the set of rings with h_2 at higher frequencies.

5.2.2 Optimized Waveguide-Fed Dual-Depth Bull's Eye Antenna

The analysis of Chapter 4 demonstrated that a subwavelength slot aperture is the most directive compared to the open-ended waveguide and the tapered aperture, however it limits the matching bandwidth, hence the achievable realized gain. Fig. 5.4 shows that despite the fact that the 3-dB bandwidth of the dual-depth antenna includes the band between 280 and 285 GHz, the matching response there is borderline satisfactory. In order to secure a good matching performance at all the available 3-dB bandwidth, the slot aperture is replaced with a waveguide aperture. The aperture's dimensions are the

Figure 5.9: Simulated S11 of waveguide-fed Bull's Eye antennas with $N=10$.Table 5.4: Waveguide-fed dual-depth Bull's Eye antenna with $N=10$ at around 300 GHz.

	N	3-dB BW [GHz]	Max. Dir [dBi]	GBWP
	5	25	19.63	2137
h_1	7	16	22.2	2449
	10	13	23.9	2978
$h_1 + h_2$	10	25.4	21.65	3387

typical of the feeding WR-3 waveguide. Fig. 5.9 confirms that an antenna with an open-ended waveguide aperture achieves a matching performance below -10 dB at the frequency band of interest.

The findings of Chapter 4 allow the safe assumption that the same trends in S11 and gain/directivity can be expected in the performance of the dual-depth antenna with a waveguide aperture, compared to the same antenna with a slot aperture. A comparison procedure similar to the previous subsection is available in Table 5.4. The antennas are compared in terms of 3-dB gain bandwidth, maximum directivity and gain-bandwidth product. The achieved maximum directivity is about 1 dBi lower than the corresponding slot realization, which is expected, due to the analysis of Chapter 4. The 3-dB gain bandwidth for the design of 10 rings is 8.85%.

5.3 Leaky Wave Analysis of the Dual-Depth Antenna

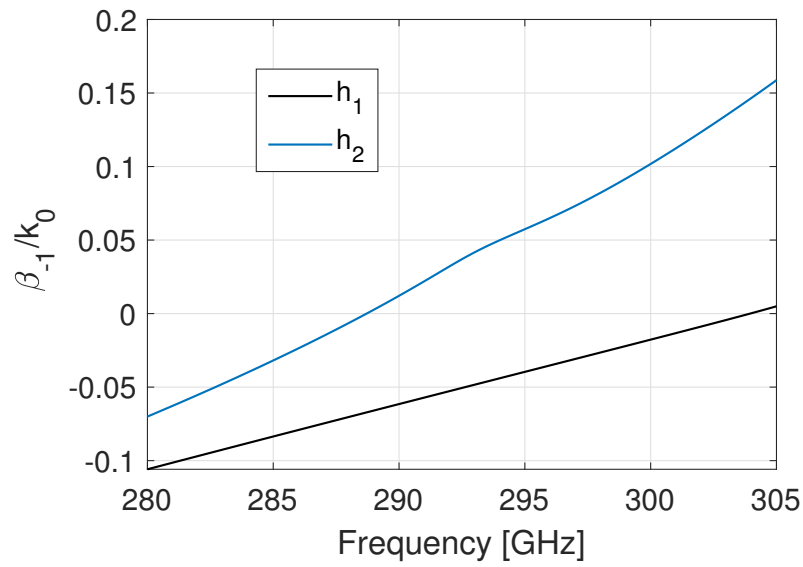
The farfield radiation of the dual-depth corrugated antenna can be explained with the known leaky wave theory. Due to the fact that both h_1 and h_2 are smaller than $\lambda_0/4$, the formation of a TM surface mode is permitted on the corrugations, which converts to a leaky wave. Also, since the gap width w is larger than $\lambda_0/2$, the leaky wave analysis can be done with the analytical periodic method described in Section 3.2.

The complex longitudinal wavenumber k_y which characterizes the leaky mode is calculated from a transverse resonance equation at $z = 0$ (Fig. 5.3.b). For the analysis of the dual-depth corrugated model, a leaky wave analysis is performed for a single depth antenna of h_1 and a single depth antenna of h_2 . The antennas are considered infinitely long in size. Due to their periodic modulation with $d \approx \lambda_0$, we can safely assume the propagation only of the $n = -1$ Floquet harmonic of the longitudinal guided wave as

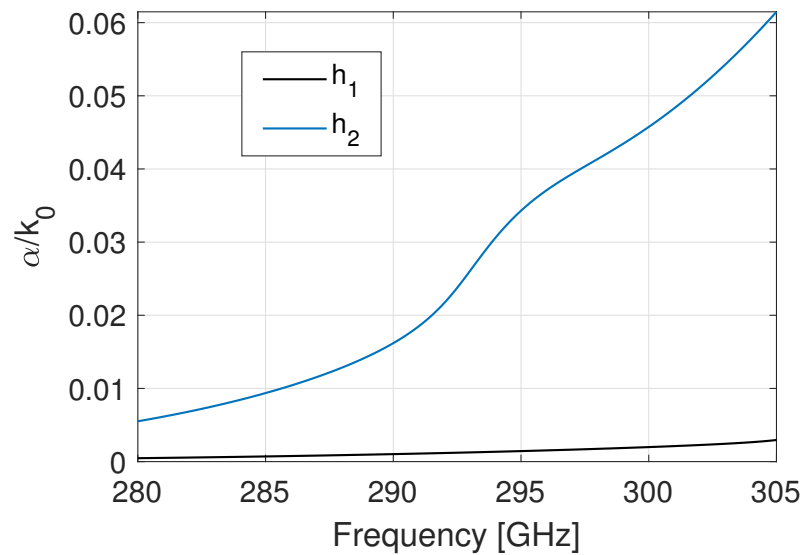
$$k_{y-1} = k_y - 2\pi/d = \beta_{-1} - j\alpha \quad (5.2)$$

where β_{-1} is the phase constant of the -1 harmonic and α is the attenuation constant.

Fig. 5.10.a shows the propagation constant distribution with frequency for each single depth design. Both antennas are characterized by a fast wave ($|\beta_{-1}/k_0| < 1$), with the main beam scanning from the backward to the forward quadrant as β_{-1} obtains both negative and positive values. From the condition ($|\beta_{-1}| < \alpha$) for an infinite size symmetrically-fed leaky wave antenna to radiate at broadside, for the h_2 antenna the maximum radiation is expected around 285 GHz and for the h_1 antenna maximum radiation is expected around 303 GHz. These analytical results can be confirmed from the



(a)



(b)

Figure 5.10: Leaky-wave analysis of each single depth antenna (a) propagation constant and (b) attenuation constant.

full-wave simulations of the finite size models (see Fig. 5.7). A small declination in the frequency band of maximum radiated power is expected due to the fact that the leaky wave analysis assumes infinite size antennas and full-wave simulations refer to finite size models.

From the graph of Fig. 5.10.b it is apparent that the losses increase with the increase of the depth h . This implies that corrugated designs with large values of h approach sufficiently the infinite size assumption, from $L = 0.18\lambda_0/\alpha$, where L is the half-length of the antenna. Large values of α also limit the $|\beta_{-1}| < \alpha$ bandwidth which is a requirement for broadside radiation, which explains why the h_2 model achieves a smaller 3-dB gain bandwidth than the h_1 model.

Conclusions can be drawn from the presented leaky wave analysis for an infinite size dual-depth design. For the dual-depth design it is necessary that a backward wave ($\beta_{-1} < 0$) is launched initially from the first set of rings of h_1 , followed by a forward wave ($\beta_{-1} > 0$) excited by the second set of rings of h_2 . Where the guided waves are backward or forward at the same frequencies, the antenna operates outside its 3-dB bandwidth (split-beam radiation pattern).

At lower frequencies (around 280 GHz), the radiation of the h_2 antenna dominates (its β_{-1} values close to zero), with the radiation pattern side lobes produced mainly by the h_1 design. At higher frequencies, the reverse farfield behaviour is observed, with the main beam produced by the h_1 rings and the higher directivity attributed to lower corresponding α values. From Fig. 5.7 the total maximum directivity of the dual-depth antenna is observed at 295 GHz, where the $|\beta_{-1}|$ values of each single depth design are the closest to zero at the same time (Fig. 5.10.a). These noted trends are verified by the simulated farfields of Fig. 5.8.

Finally, the high attenuation constant α of the h_2 design explains the findings of Table 5.3, where $N = 12$ and the antenna performance is similar to the h_1 antenna. The effect of the h_2 unit cells attenuates significantly with respect to h_1 unit cells, as N approaches the

infinite size assumption. For this reason, the matrix pencil method could not be applied directly on an (approaching infinite size) dual-depth antenna, due to the attenuated effect of the large number of unit cells with h_2 .

5.4 Fabricated Prototype and Measured Results

The optimized dual-depth antenna with 10 rings and a waveguide aperture was selected as for fabrication due to the achieved matching response below -10 dB. The prototype was fabricated at the University of Birmingham (Fig. 5.11).

A three-axis CNC milling machine was used to create the corrugated rings on the surface of an aluminum plate. The fabrication proceeded by splitting the plate in two halves across the E -plane of the waveguide, as suggested for minimum disturbance of the main radiating mode. The two metallic blocks were joined back together with screws that were attached on two extra metal blocks added on both sides of the antenna. The thickness of the plate had to be extended from the initial value 0.91 mm to 7 mm, so that the pins of the waveguide flange could fit perfectly inside the ground plane. Simulations showed that such modifications did not affect the performance of the antenna.

The antenna was measured with a network analyzer and the antennas used were two horn antennas from 282 to 298 GHz, fed with WR-3 waveguides. It should be mentioned that the Fraunhofer distance for the Bull's Eye antenna is calculated at nearly 0.8 m from $2D^2/\lambda_0$, where D is the longest dimension of the antenna (the diameter of the outer corrugated ring). The gain of the Bull's Eye antenna was measured with the known substitution method [7].

Initial measurements demonstrated that the operation of the antenna was shifted

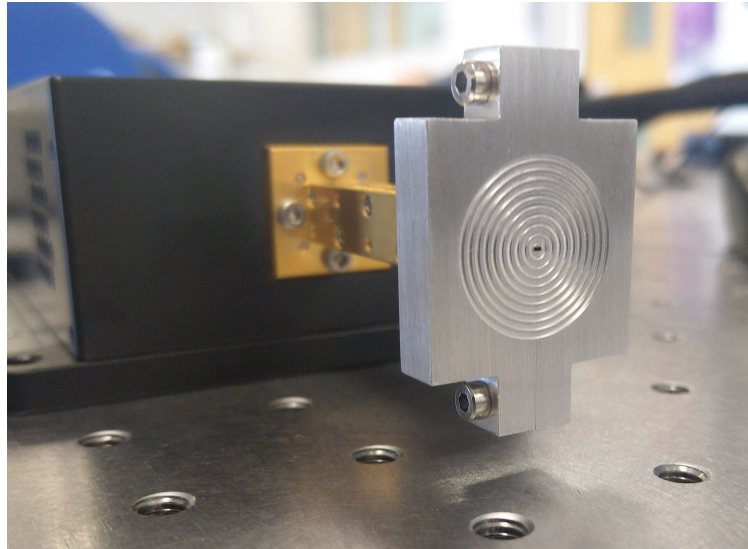


Figure 5.11: Fabricated dual-depth antenna at 300 GHz.

towards higher frequencies, which implied some slight discrepancies for the dimensions of the fabricated prototype. Such inaccuracies are expected to have a severe impact at low THz frequencies. An infrared scan revealed the actual dimensions of the fabricated prototype (Fig. 5.12). From this graph, where x is the longitudinal distance of the antenna, dimensions are $d = 0.9728$ mm, $w = 0.562$ mm, $h_1 = 0.167$ mm (inner ring) and $h_2 = 0.302$ mm (outer ring). The measured S11 and realized gain of the fabricated prototype are compared to the simulated of the redesigned antenna in Fig. 5.13.

Overall, a very good agreement between simulation and measurement can be observed. The matching response is very broadband, as the measured S11 values below -10 dB show. The curve of the measured gain shows two maxima of 22.5 dBi at 301 GHz and 20.5 dBi at 285 GHz, at the same frequencies as the redesigned simulated antenna. The observed ripples (less than 2 dB) in the realized gain are due to the similar variation of the reference horn antenna gain.

The setup of Fig. 4.14 was used in order to measure the radiation patterns of the antenna. The Bull's Eye antenna and the 300 GHz horn antenna were placed at a farfield

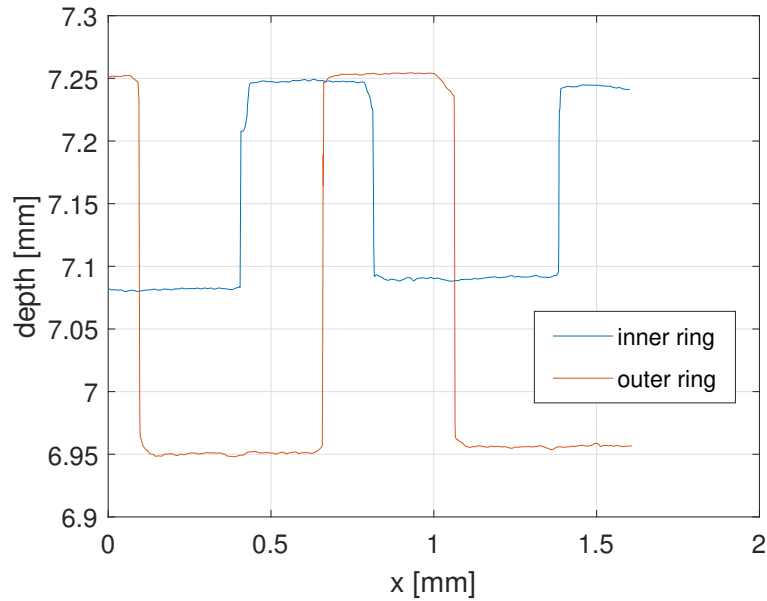


Figure 5.12: Infrared scan of the fabricated dual-depth antenna at 300 GHz.

distance of approximately 1 m. The Bull's Eye antenna was mounted on a rotating base. The angles from -90° to $+90^\circ$ were scanned for both planes at several frequency points, with a resolution of 1° per rotation. A comparison between measurement and simulations at selected frequencies can be seen in Figures 5.14 and 5.15.

A very good agreement between simulation and measurements is evident with respect to the radiation patterns. Fig. 5.14, in particular, demonstrates a lower measured SLL than in simulations in all of the frequencies. This can be attributed to fabrication inaccuracies that were not detected by the infrared scan. Regarding the E -planes, the agreement is very good, although at some frequency points a small asymmetry between the negative and the positive quadrant is detected (5.15). This can be attributed to an imperfect bending of the two split pieces back together. Since the splitting was made across the E -plane of the antenna, it is expected this plane to be more affected from any imperfections and dimension discrepancies. Also, for the measurement of the E -plane the ports of the VNA had to be rotated by 90° , since no L-shape tool was available, therefore

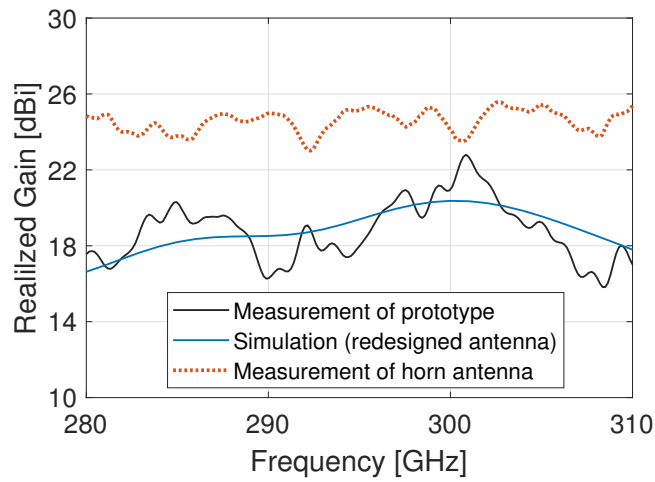
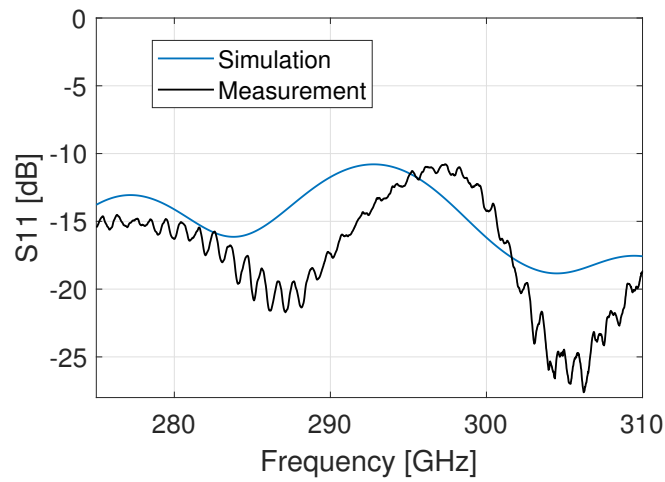


Figure 5.13: Measured versus simulated (a) S_{11} parameters and (b) Realized gain of the waveguide aperture fed Bull's Eye antenna. The simulated results refer to the redesigned antenna.

the ports were not that stably fixed to the base as previously. This might have led to a small misalignment between the antennas during the movement of the rotating base. Overall, a highly directive performance is observed at both planes for frequency points that cover the 3-dB bandwidth.

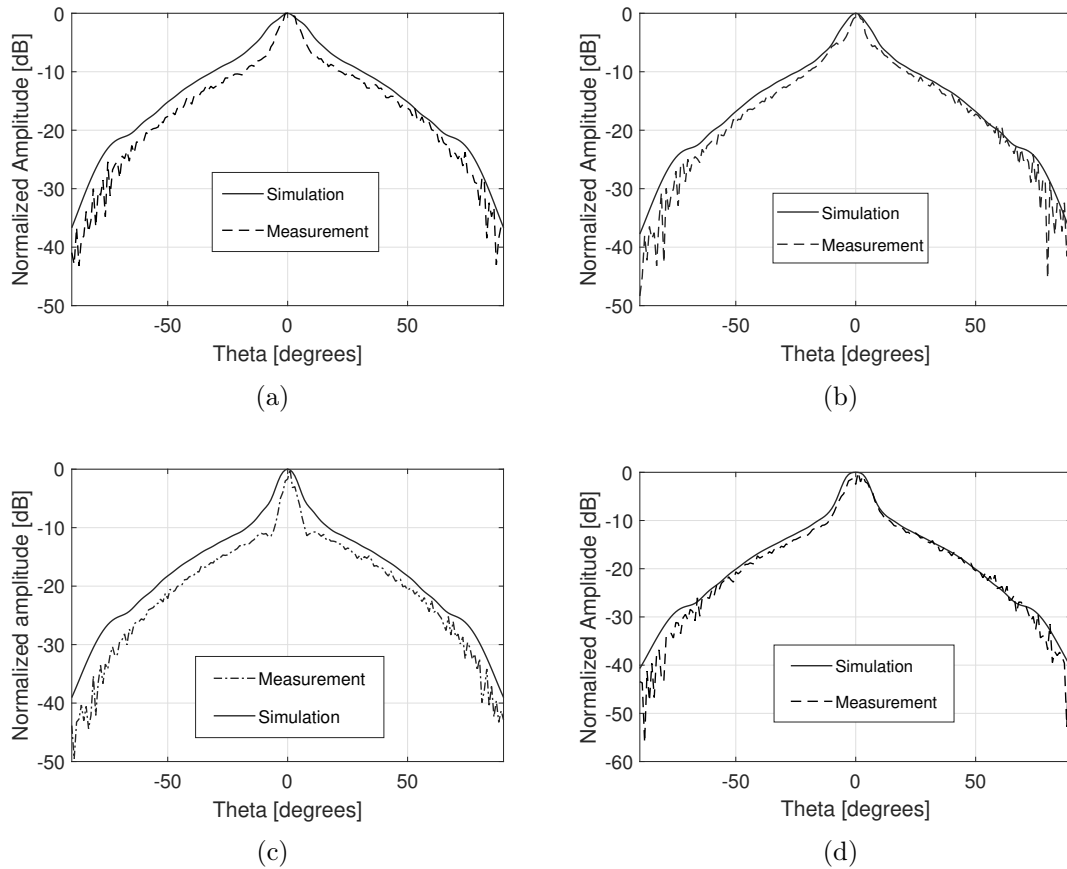


Figure 5.14: Normalized H -plane measurements at (a) 281.2 GHz, (b) 288.1 GHz, (c) 296 GHz, (d) 304.2 GHz.

5.5 Conclusion

A bandwidth enhancement technique has been proposed in this Chapter, for Bull's Eye antennas operating at low THz frequencies. This technique exploits the depth qualities of the corrugations, by employing two different values for two sets of indented rings. This technique, although it has been presented for higher frequencies, can be also implemented to 1D and 2D corrugated antennas on microwaves and mm-waves.

An initial design for broadside operation around 300 GHz is presented, which achieves a 3-dB gain bandwidth of 8.85% with a maximum gain of 21.7 dBi. An extensive simulation study has proven that the dual-depth corrugated design outperforms in gain-bandwidth

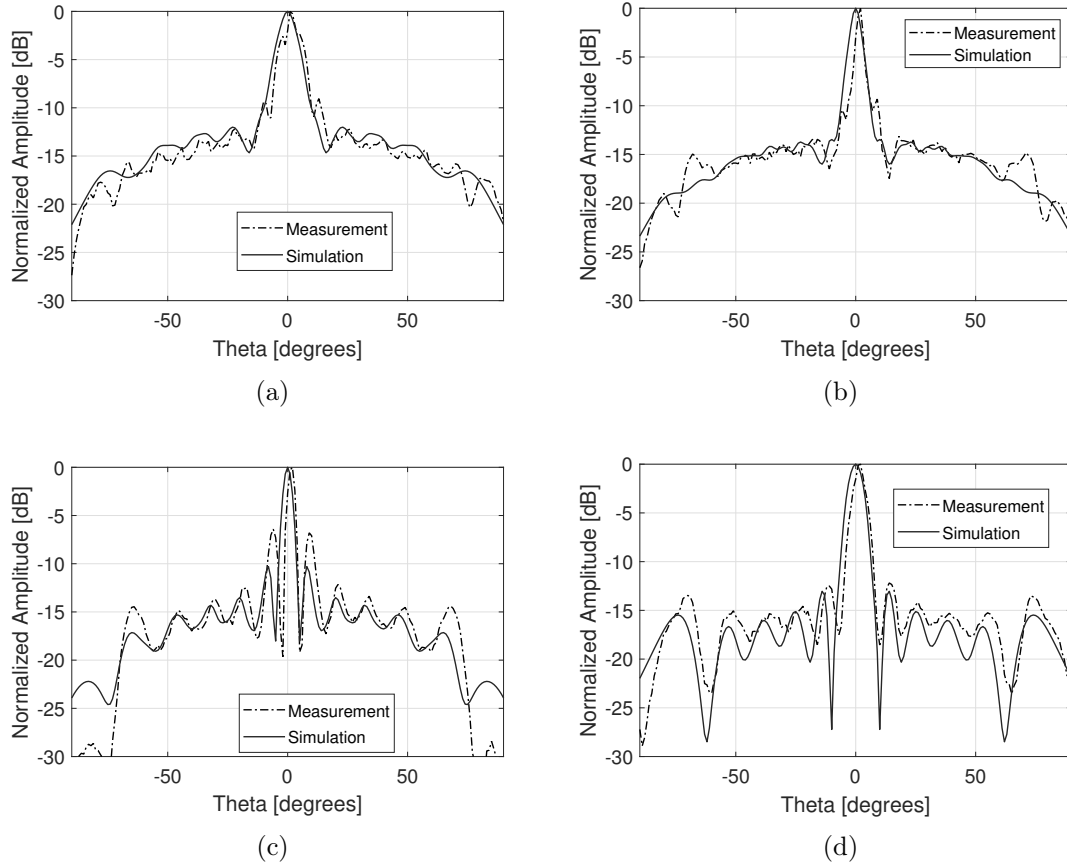


Figure 5.15: Normalized E -plane measurements at (a) 281.2 GHz, (b) 284.2 GHz, (c) 296 GHz, (d) 304.2 GHz.

all standard implementations of similar maximum gain, similar size, or similar bandwidth.

The novel analytical leaky-wave periodic method of Chapter 3 has been implemented on the single depth antennas of h_1 , h_2 in order to extract conclusions for the operation of the dual-depth design. For the dual-depth antenna, the frequency of broadside operation for the symmetrically-fed antenna can be estimated, and the principle of operation is explained with leaky wave analysis terms.

The optimum prototype uses the open-ended waveguide aperture introduced in Chapter 4. It was fabricated and experimentally tested, validating the simulations. The small frequency shift compared to the original design is attributed to inaccuracies of the fabrication process which have a significant effect in this frequency band.

References

- [1] M. Beruete, I. Campillo, et.al. "Very low profile "Bull's Eye" feeder antenna", *IEEE Antennas Wireless Propag. Lett.*, vol. 4, pp. 365–368, 2005.
- [2] C. J. Vourch and T. D. Drysdale, "V-Band "Bull's Eye" Antenna for CubeSat Applications," in *IEEE Antennas and Wireless Propagation Letters*, vol. 13, pp. 1092-1095, 2014.
- [3] U. Beaskoetxea et al., "77-GHz high-gain bull's-eye antenna with sinusoidal profile," *IEEE Antennas Wireless Propag. Lett.*, vol. 14, pp. 205–208, 2015.
- [4] U. Beaskoetxea and M. Beruete, "High aperture efficiency wide corrugations bull's-eye antenna working at 60 GHz," *IEEE Trans. Antennas Propag.*, vol. 65, no. 6, pp. 3226–3230, 2017.
- [5] Alkaraki, S., Gao, Y., Parini, C.: "Dual-layer corrugated plate antenna", *IEEE Antennas Wirel. Propag. Lett.*, 2017, 16, pp. 2086–2089
- [6] M. Beruete, I. Campillo, J. S. Dolado, J. E. Rodríguez-Seco, E. Perea, F. Falcone, and M. Sorolla, "Dual-band low-profile corrugated feeder antenna", *IEEE Trans. Antennas Propag.*, vol. 54, no. 2, pp. 340–350, Feb. 2006.
- [7] C. A. Balanis, *Antenna Theory: Analysis and Design*, 2nd ed., *New York: Wiley*, 1997.

Chapter 6

Broadband Corrugated Antennas with Complex Shaped Unit Cells

The narrowband gain performance of conventional corrugated metallic antennas has been discussed in the previous Chapters. An enhancement in the 3-dB gain bandwidth of a planar corrugated antenna has been achieved in Chapter 5, with a suitable pairing of sets of unit cells of different depths. This implementation made use of the classical rectangular corrugated unit cell.

This Chapter introduces novel metallic corrugated unit cells with complex shapes. Such non-conventional shaped unit cells create more than one resonant gaps (equivalent to parallel-plate waveguides) within one period, and possess extraordinary leaky wave properties. The optimum models exhibit improved performance farfield features, such as large 1-dB gain bandwidth or enhanced 3-dB gain bandwidth for a moderate antenna size of 6 rings. The presented results correspond to corrugated antennas operating at around 15 GHz for ease of fabrication with CNC milling, due to their subwavelength

design details.

6.1 The Impact of Standard Shaped Gaps on Planar Corrugated Antennas

The leaky wave analysis of Chapter 3 for corrugated designs with two categories of gap sizes (smaller than $\lambda_0/2$ and larger than $\lambda_0/2$) has given insight into the characteristics of the radiation patterns of the corresponding finite size antennas. It has been revealed that for designs with narrow gaps, the dominant *TEM* mode inside the gaps is characterized by a high attenuation constant (or leakage rate), which results in low directive antennas. On the other hand, for gap widths larger than half-wavelength, the dominant *TM₁* mode is responsible for highly directive radiation patterns, due to its small attenuation. In this Section, the numerical relationship between the gap size and the realized bandwidth and directivity is explored for antennas of a fixed overall size.

The reference Bull's Eye antenna of this study is for optimum performance at 15 GHz. Radiation takes place via an open-ended waveguide aperture with the standard WR-62 dimensions of the feeding waveguide. The periodicity d of the rings is 19.62 mm and the depth of rings is 3.3 mm. The overall size of this antenna is $24 \times 24 \text{ cm}^2$ and the total plate height is 7.5 mm. For a fixed periodicity d , a parametric sweep with respect to the gap width w is performed in CST Microwave Studio, while tracking the maximum realized gain and corresponding 3-dB gain bandwidth of the antenna. Fig. 6.1 shows the results of this parametric study.

For w between 10 mm and 11.7 mm (slightly larger than $\lambda_0/2$), there is a continuous

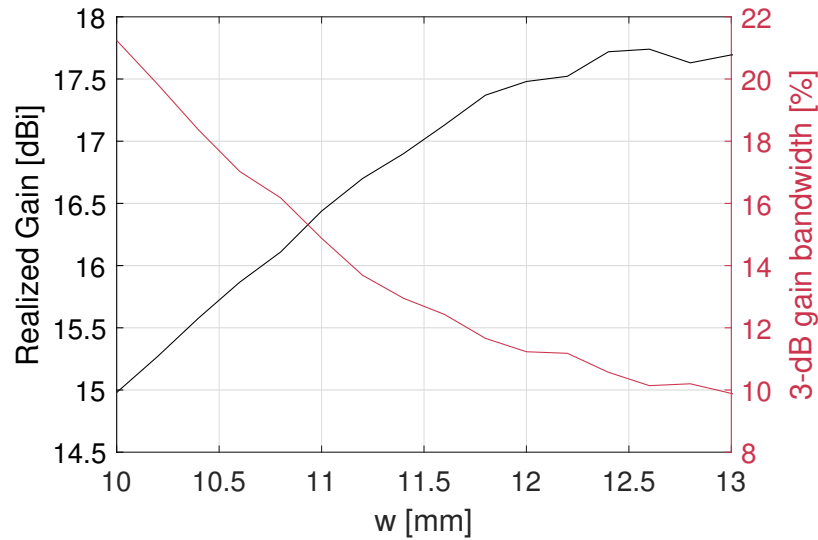


Figure 6.1: A comparative study between gap width w , peak realized gain and 3-dB gain bandwidth for a 2D corrugated antenna with six rings at around 15 GHz (simulation results).

drop of the 3-dB gain bandwidth by $\sim 10\%$, while the maximum gain increases by ~ 2 dBi (from 15 dBi to 17 dBi). For $w > 11.7$ mm, the achievable maximum gain reaches a saturation point of 17.7 dBi. The 3-dB gain bandwidth at this point is no more than 1.5 GHz (9.4 %). For very large gap values (over 13.6 mm) compared to the periodicity, the achieved maximum gain slightly drops as the 3-dB gain bandwidth continues to shrink.

Therefore, as a compromise between high gain and satisfactory gain bandwidth, the antenna should be designed with gap widths slightly over $\lambda_0/2$. The numerical results of this Section will be used as a reference conventional Bull's Eye antenna in the following Sections, where novel types of corrugations are studied and the choice of operation at the Ku band will be more evident.

6.2 The Perturbed Corrugation Concept

A novel shaped corrugated unit cell is introduced in this Section, as depicted in Fig. 6.2. In the middle of the central gap (w), a metallic perturbation of height h_b and length l_b

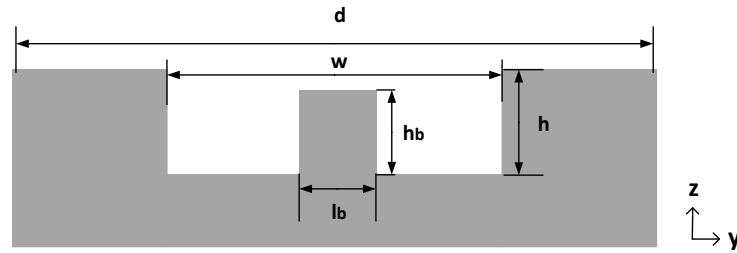


Figure 6.2: Cross section of a metallic unit cell with perturbed corrugation (design details).

is inserted. The concept of this engineering process is to increase the overall longitudinal resonant path by creating a second parallel plate waveguide inside the main gap (w). For direct comparison with the unit cell of Section 6.1, the dimensions the unit cell of Fig. 6.2 are selected as $d = 19.6$ mm, $h = 3.3$ mm for operation at 15 GHz. The rest of the parameters w , h_b and l_b are variable, and their effect is examined separately.

A Bull's Eye antenna with 6 perturbed rings as in Fig. 6.6 is studied in this paragraph. The overall size of this antenna is 24×24 cm² and $h_p = 7.5$ mm. The height of perturbation h_b is subject to parametric study, while its length h_b is set arbitrarily to 1 mm ($\ll \lambda_0$). Three perturbed shaped corrugated antennas are simulated, with $w < \lambda_0/2$, $w \sim \lambda_0/2$ and $w > \lambda_0/2$. Their simulated directivity performance is available in Fig. 6.4 for each w case. A maximum gain similar to the directivity is expected, due to the use of the open-ended waveguide aperture.

The impact of the perturbed corrugation on the overall antenna directivity is not significant when $w < \lambda_0/2$, except from the small shift towards higher frequencies (about 1 GHz topmost when $h_b = h$). When $h_b = h$ (maximum directivity 15 dBi), the 1-dB bandwidth is extended, as the directivity obtains values between 14 dBi and 15 dBi for the frequencies between 13.8 GHz and 15.3 GHz.

When $w \sim \lambda_0/2$ and $w > \lambda_0/2$ an impressive enhancement in directivity is achieved, along with slightly enhanced 3-dB gain bandwidth for some h_b cases. In particular, in Fig.

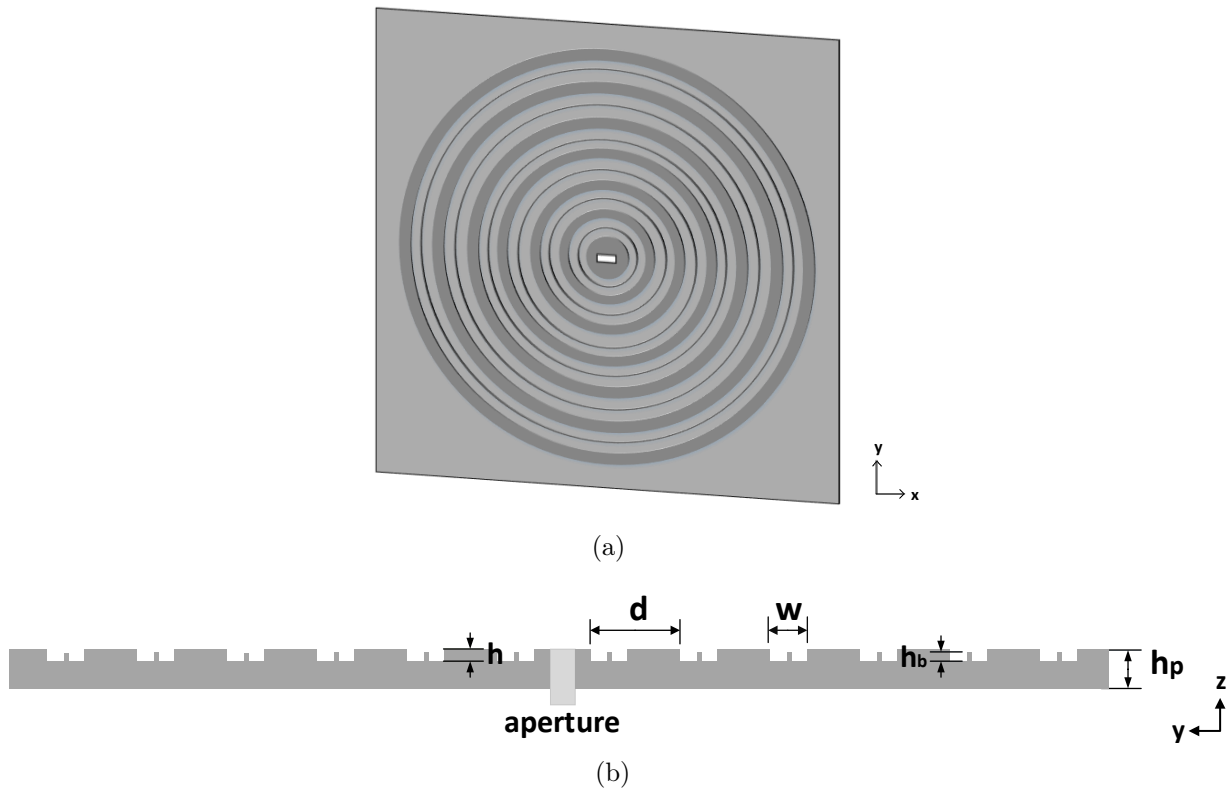


Figure 6.3: Perturbed Bull's Eye antenna with 6 rings and waveguide aperture. (a) Front view, (b) Profile.

6.4.b, the directivity reaches up to 21 dBi for $h_b = h$, compared to only 14 dBi achieved by the standard shaped design. When $h_b = h/2$, the maximum directivity is 15.5 dBi with a 3-dB gain of nearly 19.5%, while from a conventional Bull's Eye antenna of the same size, the same maximum directivity is met with 18.9% bandwidth (Fig. 6.1). Furthermore, when $h_b = 2h/3$ and maximum directivity is 17.5 dBi with a 3-dB bandwidth of 12.6%, a conventional Bull's Eye antenna of the same size achieves this directivity with 11.3% bandwidth (Fig. 6.1). In Fig. 6.4.c, when $h_b = h$ a maximum directivity of up to 21.8 dBi can be reached. In this case, however, the increase is no more than 4 dBi compared to the conventional design. This is due to the already strong TM_1 mode which is characterized by low attenuation constant.

Regarding the parameter l_b , simulations showed that it does not affect the design

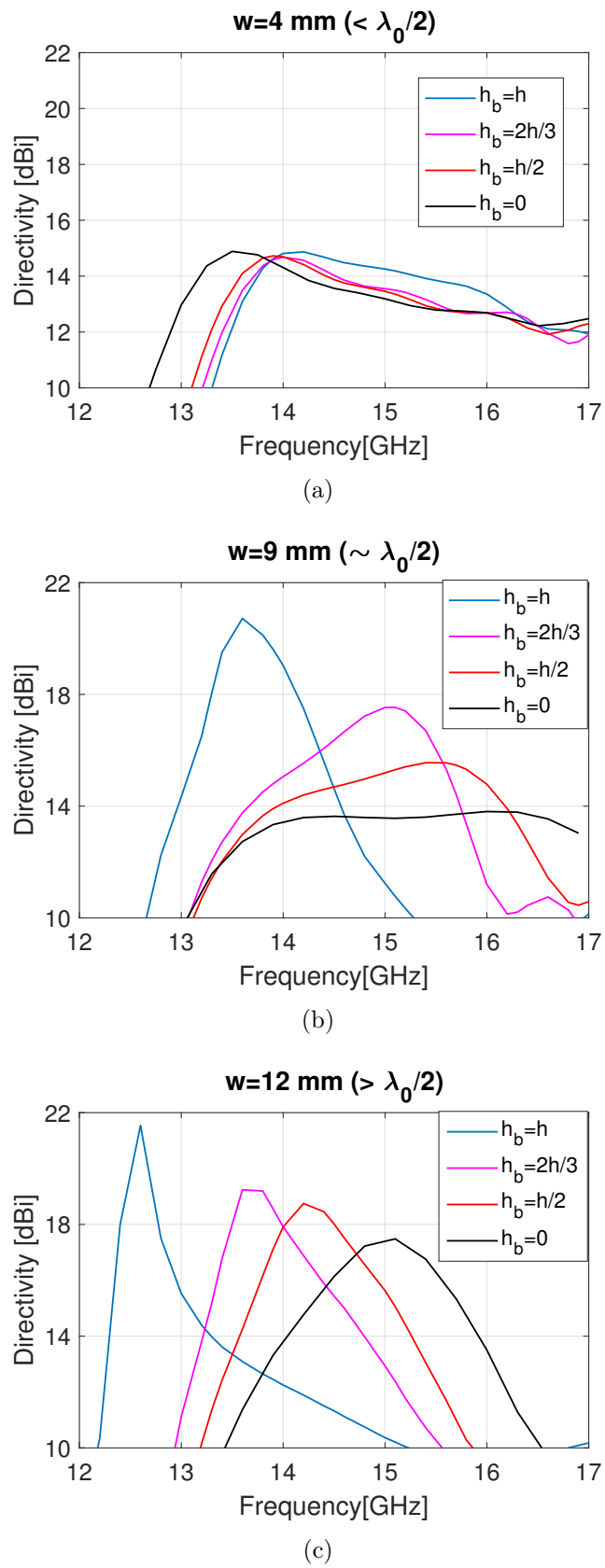


Figure 6.4: Simulation results for the Bull's Eye antenna of Fig. 6.6 (a) $w = 4 \text{ mm}$, (b) $w = 9 \text{ mm}$, (c) $w = 12 \text{ mm}$.

performance, therefore it can be fixed to an arbitrary value.

In conclusion, the first elements towards the bandwidth enhancement of Bull's Eye designs are offered with the proposed perturbed corrugations when h_b obtains values between $h/2$ and $2h/3$, and when the main gap w is at the order of half wavelength.

6.3 The Double Corrugation Concept

Towards the goal of high gain and broadband antenna performance, another new concept of corrugated unit cell is examined here, with details as in Fig. 6.5. A "corrugation within corrugation" concept is employed, or "double corrugation", with a secondary corrugation with horizontal length $(d - w)/2$, gap w_r and height h_r formed within a standard shaped unit cell of design parameters d, h, w . The incorporation of this unit cell into a finite size antenna is demonstrated below for a planar configuration.

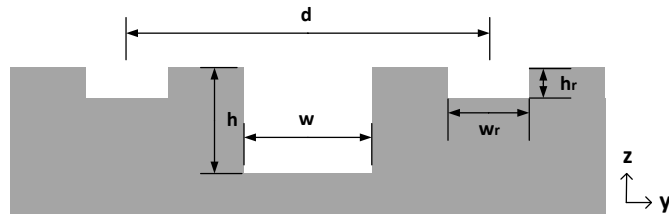


Figure 6.5: Cross section of corrugated metallic unit cell with double corrugation (design details).

The effect of the double corrugation concept is investigated for a six ring planar design, simulated in CST for various gap cases. The design details for this antenna are : $d = 19.6$ mm, $h = 3.3$ mm, $h_p = 7.5$ mm and overall antenna size 24×24 cm². The feeding is via an open-ended waveguide aperture for operation at 15 GHz. Simulated directivity results are available in Fig. 6.7 for three antennas with $w < \lambda_0/2$, $w \sim \lambda_0/2$ and $w > \lambda_0/2$, dependant on the width w_r and the height h_r of the secondary corrugation.

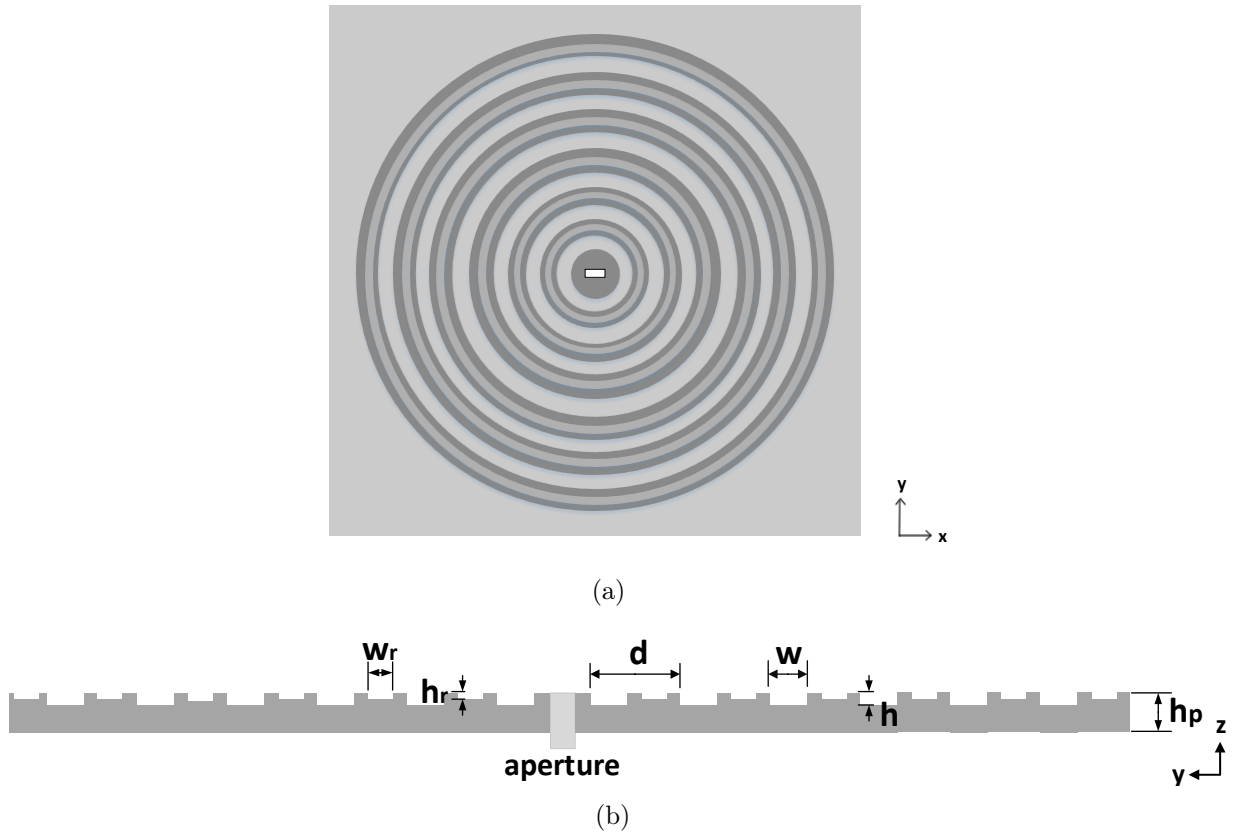


Figure 6.6: Double corrugated Bull's Eye antenna with 6 rings and waveguide aperture. (a) Front view. (b) Profile.

The effect of the secondary corrugation (w_r , h_r) is significant for w up to $\lambda_0/2$. The directivity increases with the increase of h_r , along with a shift towards lower frequencies. In particular, when $w < \lambda_0/2$, the enhancement in directivity is up to 8 dBi compared to the standard Bull's Eye antenna, for the parameter set of ($w_r = 4$ mm, $h_r = 2$ mm). When $w \sim \lambda_0/2$, a maximum directivity of 17 dBi is achieved, for the same set of w_r , h_r . The effect of the double corrugation is not significant for the overall radiation when $w > \lambda_0/2$, which can be easily explained by the strong TM_1 mode dominating inside an electrically large gap w .

The double corrugation effect is stronger when h_r is larger, as the directivity is maximized at lower frequencies. This shift can be explained from the increase of the overall

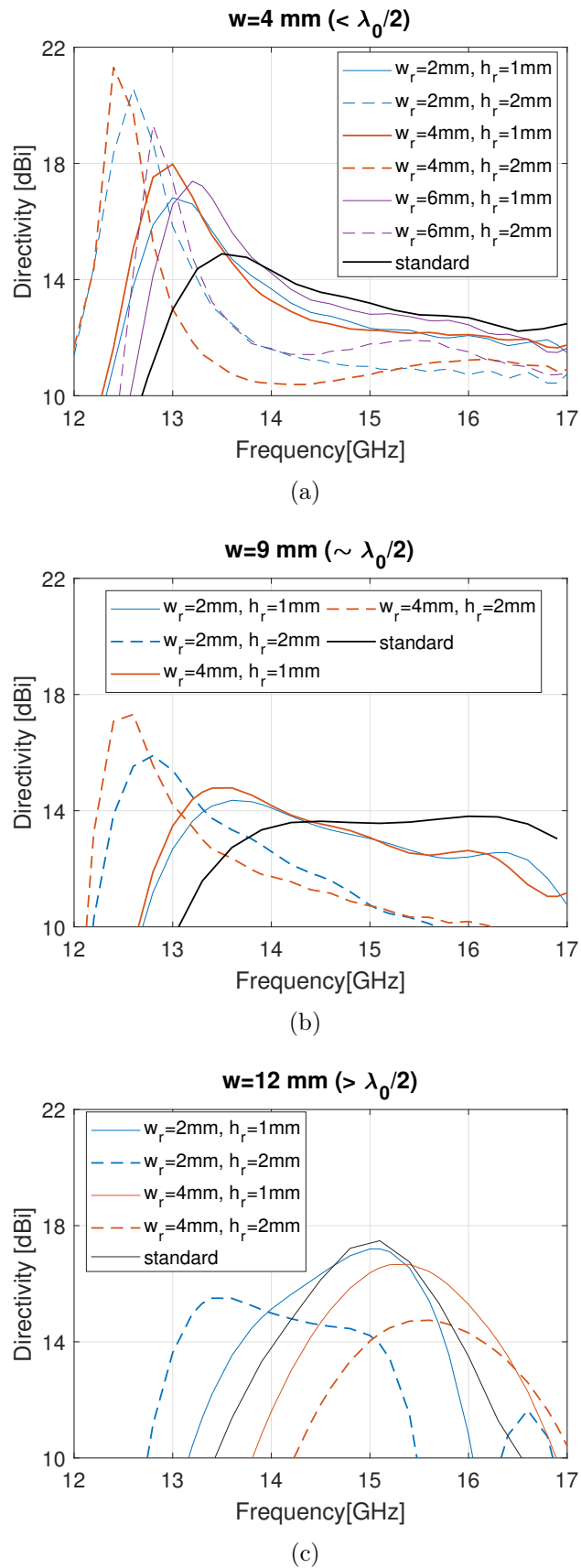


Figure 6.7: Simulation results for the Bull's Eye antenna of Fig. 6.6 (a) $w = 4 \text{ mm}$, (b) $w = 9 \text{ mm}$, (c) $w = 12 \text{ mm}$.

resonant path. According to the depth (h) relationship with the resonant wavelength λ_0 as $h \approx \frac{(2n+1)\lambda_0}{4}$, the directivity plot shifts further to the left, as h , h_r obtain bigger values.

6.4 The Hybrid Corrugation Concept

The novel perturbed and double corrugated unit cell concepts, are now combined into a hybrid type of corrugation, just as in Fig. 6.8. The aim of this combined concept is to take advantage of both distinct effects in directivity and bandwidth enhancement. It has been proven already that the perturbed effect is significant only when $w \geq \lambda_0/2$, while in Section 6.3 it was demonstrated that the double corrugation concept takes effect only for gaps $w \leq \lambda_0/2$. Therefore, the optimization process for the hybrid unit cell is for w around $\lambda_0/2$.

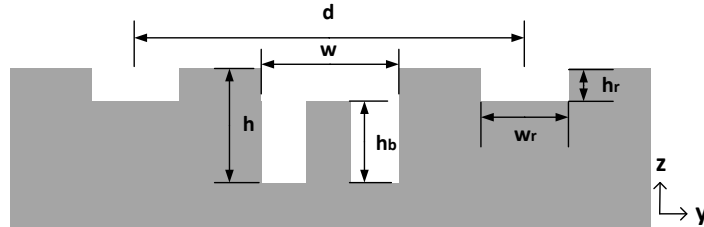


Figure 6.8: Cross section of corrugated metallic unit cell with hybrid corrugation (design details).

A six hybrid unit cell Bull's Eye antenna is designed and simulated in parametric sweep. The design details for this antenna are same as in the previous Sections: $d = 19.6$ mm, $h = 3.3$ mm, $h_p = 7.5$ mm and overall antenna size 24×24 cm². The antenna is fed with a waveguide aperture, for operation at around 15 GHz. Novel designs with improved characteristics have been generated for various sets of w_r, h_r, h_b , while l_b has been set to 1 mm. The performance of the hybrid type of corrugated antenna is demonstrated below in terms of fractional bandwidth and maximum directivity, compared to a

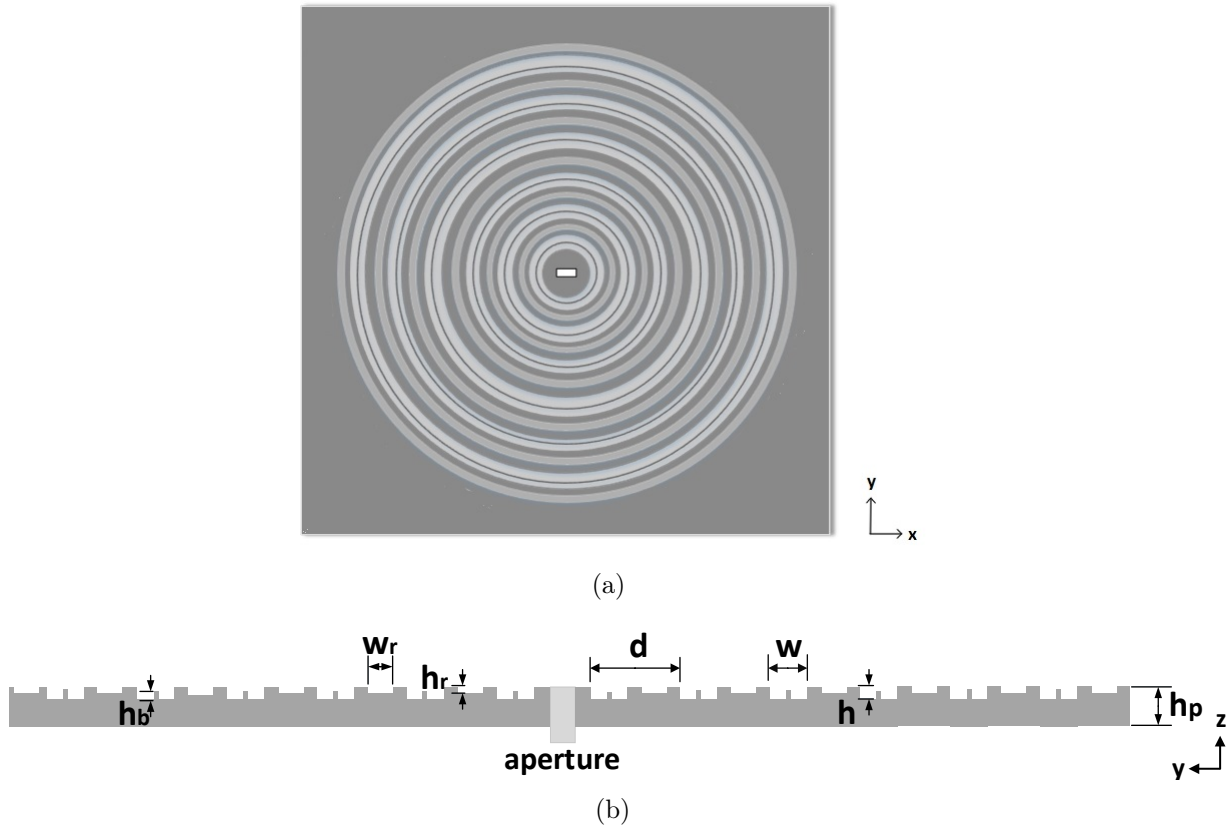
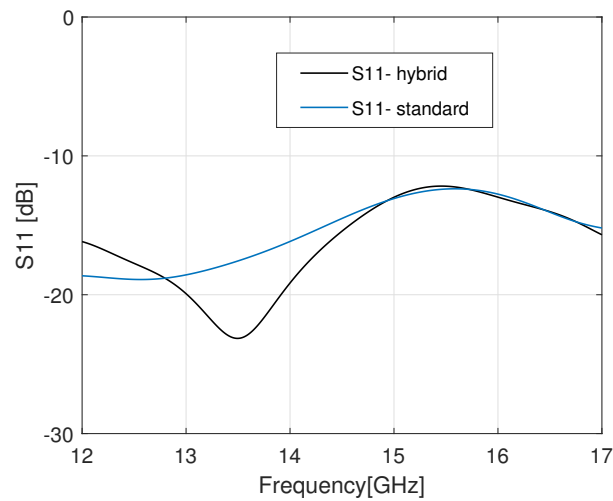


Figure 6.9: Hybrid corrugated Bull's Eye antenna with 6 rings and waveguide aperture. (a) Front view. (b) Profile.

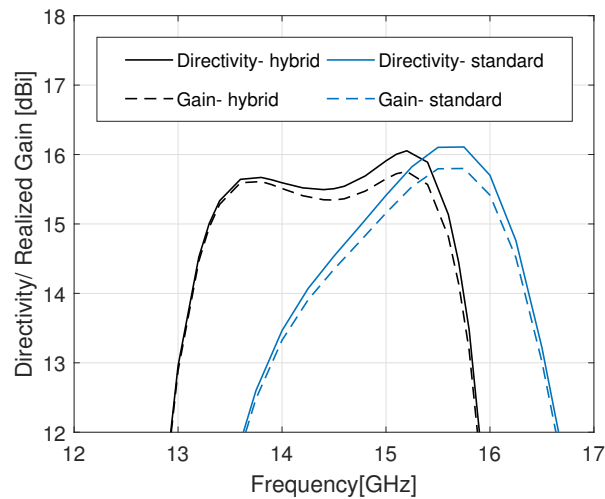
conventional corrugated design of the same size. Two optimized prototypes are presented, each demonstrating different radiation properties.

6.4.1 Optimized Hybrid Prototype with Flat Gain Response

A novel planar design of six corrugations is presented in this Section, exhibiting for the first time a flat gain response along with high directivity. The design details of the optimized novel antenna are $w_r = 8$ mm, $h_r = 1$ mm, $h_b = 1.64$ mm, $w = 9.4$ mm, $h = 3.31$ mm, while the standard Bull's Eye antenna of the same maximum directivity uses a gap of $w = 10.6$ mm (Fig. 6.1). The simulated farfield performance of this hybrid prototype is shown in Fig. 6.10 for S11, directivity and realized gain. A comparison is also presented



(a)



(b)

Figure 6.10: Simulation results of an optimized hybrid Bull's Eye antenna with flat gain response and comparison with a standard Bull's eye antenna with similar directivity/gain in (a) S_{11} , (b) Directivity and realized gain.

between the proposed novel design and a standard uniform Bull's eye antenna design with the same maximum gain (directivity).

The maximum directivity of both designs is 16 dBi (realized gain 15.8 dBi). The extraordinary characteristic of this novel hybrid design is the large 1-dB gain bandwidth, which covers the frequency range from 13.2 GHz to 15.6 GHz (16.4 %). Such a flat gain response cannot be achieved for corrugated antennas with relatively high directivity. For

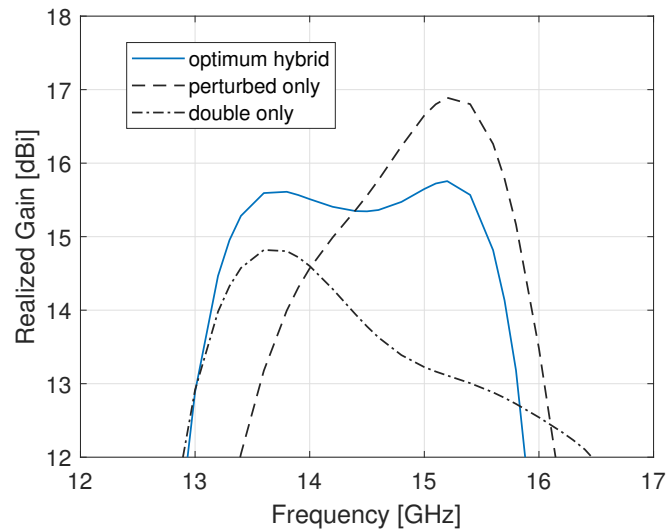


Figure 6.11: Contribution of each corrugation type in the hybrid effect of the flat gain antenna.

example, a flat directivity response for a standard Bull's Eye antenna is observed in Fig. 6.4.b, however its maximum value is only 13.8 dBi. From Fig. 6.10.b, the 1-dB gain bandwidth of the standard design is only 9.1%. The 3-dB gain bandwidth of the hybrid model is at 19.64 %, while for the standard antenna it is 17.47 %. The hybrid design maintains a good matching response below -10 dB.

The effect on each corrugation in the realized gain of the hybrid antenna can be viewed separately in Fig. 6.11. The optimum model is compared with two antennas of the same size; the first antenna consists of perturbed corrugations only and the second antenna consists of double corrugations only, with the same dimensions as with the optimum hybrid design. The flat gain response of the hybrid model exhibits two peaks, each generated by the different component of the hybrid corrugated unit cell. The peak of maximum gain (15.7 dBi) is generated by the perturbed corrugations, at 15.2 GHz, and the second peak that maintains the flat gain (15.6 dBi) at 13.6 GHz is generated by the double corrugations. It is interesting to notice that the realized gain of the hybrid antenna over the 3-dB frequency spectrum lies in the average between the two other plots.

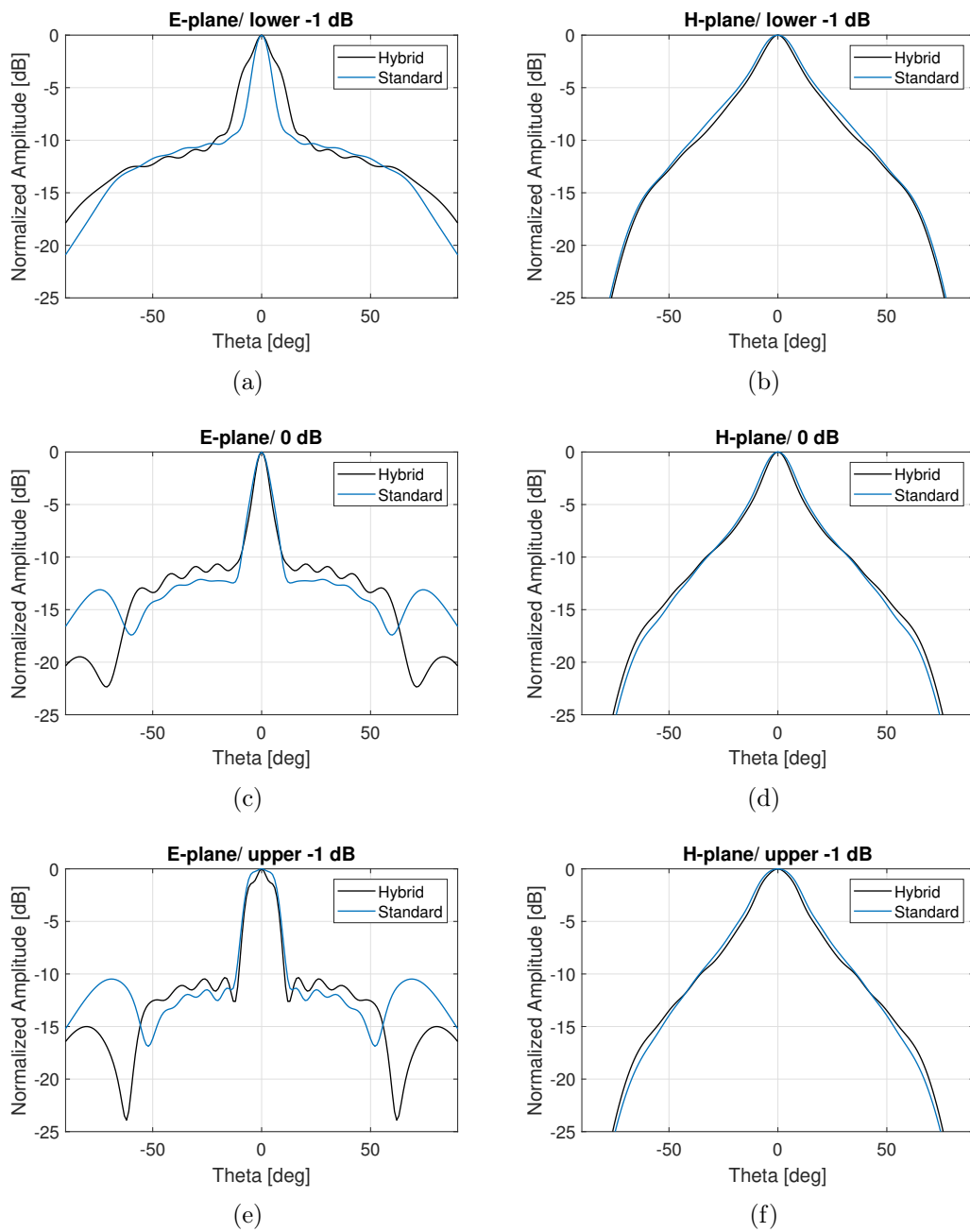


Figure 6.12: Simulated radiation patterns of the hybrid antenna with flat gain and the standard antenna of the same maximum gain. *E*-plane: (a) lower -1 dB, (c) 0 dB, (e) upper -1 dB. *H*-plane: (b) lower -1 dB, (d) 0 dB, (f) upper -1 dB.

The simulated radiation patterns are shown in Fig. 6.12, at the frequencies which determine the 1-dB gain spectrum. For the hybrid antenna, these frequencies are: lower -1 dB at 13.2 GHz, 0 dB at 15.2 GHz and upper -1 dB at 15.65 GHz. For the standard antenna, they are: lower -1 dB at 14.75 GHz, 0 dB at 15.75 GHz and upper -1 dB at 16.17

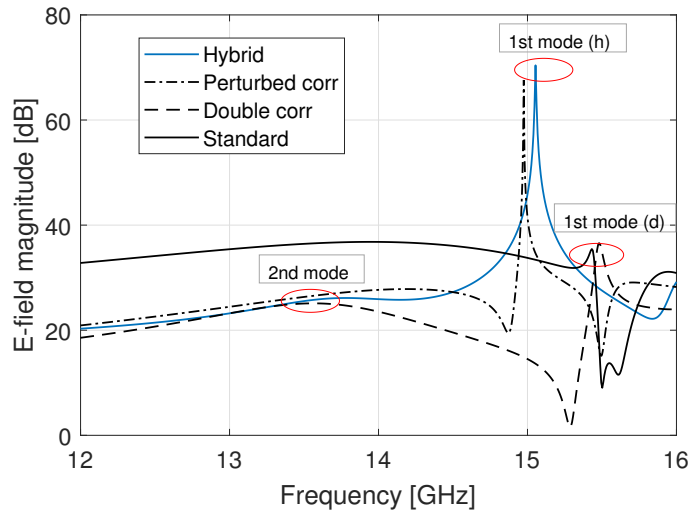


Figure 6.13: Simulated E -field magnitude of each corrugated unit cell case for $\beta=0$.

GHz. The H -planes are not affected by the hybrid effect. At the frequency of maximum gain, the side lobe level of the E -plane is at -10 dBi for the hybrid antenna and -12 dBi for the standard antenna, maintaining a highly directive lobe. At bigger angles (over $\pm 60^\circ$) the side lobe level of the hybrid antenna is significantly suppressed by more than 5 dBi compared to the standard antenna at the frequencies of maximum directivity and upper -1 dB, and about 4 dBi at the frequency of lower -1 dB. At the lower limit of the 1-dB spectrum, however, the standard design exhibits a narrower main lobe.

An explanation of the hybrid effect phenomenon can be offered by the application of the unit cell periodic method on a unit cell, terminated with periodic boundaries in the lateral plane. The longitudinal (y) electric field strength is then tracked at carefully placed probes, with a 3-D discrete port as excitation.

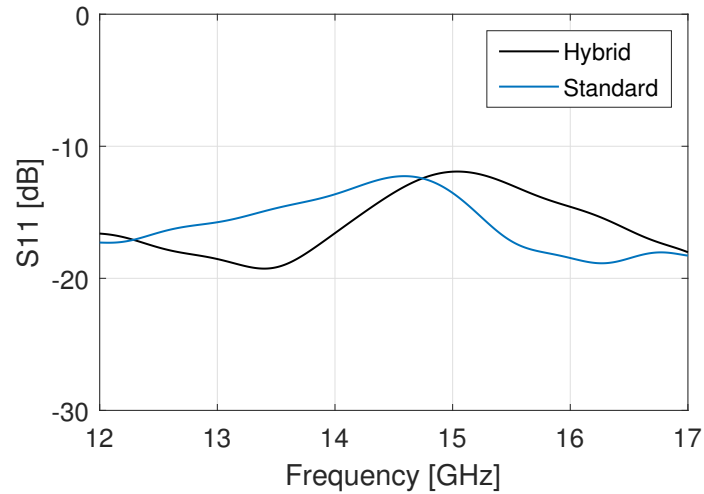
Fig. 6.13 shows the electric field distribution for $\beta = 0$ (or zero phase shift). For comparison purposes, at this same point of the dispersion diagram, the E -field plot is depicted for the separate complex shaped unit cells that form the optimum hybrid, and the standard corrugated unit cell.

Radiation close to broadside for a unidirectional hybrid antenna is expected at around 15.4 GHz (peak of maximum electric field strength). The maximum E -field strength at this frequency (about 75 dBV/m) seems to be the contribution of the perturbed corrugation, as it can be seen from its separate plot (dashed-dotted line). A second leaky mode emerges at around 13.5 GHz, which is the contribution of the double corrugation effect (dashed line). The double corrugated unit cell excites two modes, one at around 15.6 GHz and one at around 13.6 GHz. These findings can be confirmed from full-wave simulations of the corresponding finite size models of Fig. 6.11. The two peaks of the hybrid design gain response are generated by the corresponding modes of Fig. 6.13 where the open stopband frequencies are determined.

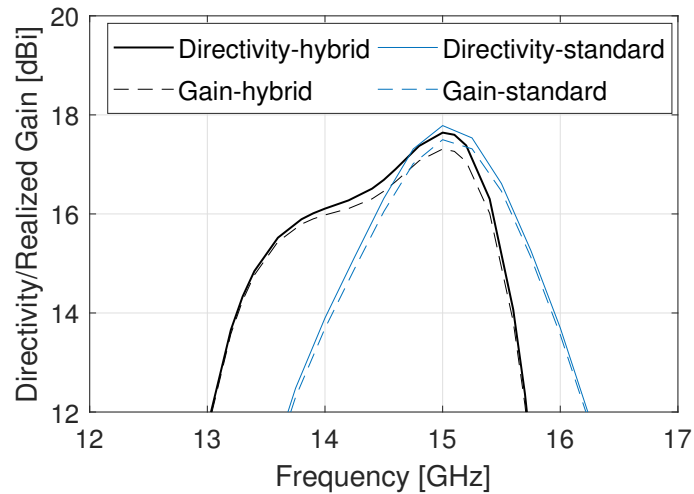
This prototype was fabricated with CNC milling at the University of Birmingham. The ground plane was extended to 10 mm in order to fit the pins of the waveguide flange inside the metal. However, due to restricted campus operations, it has been not possible to conduct measurements of this prototype. Still, since the antenna operates at the Ku band, it is not expected to have severe mismatch between simulations and measurements. The measurements of a standard Ku Bull's Eye antenna with tapered waveguide aperture, presented in Appendix A, demonstrate a very high agreement between simulations and measurements. Similar agreement is expected for the fabricated hybrid Bull's Eye antenna.

6.4.2 Optimized Prototype with Enhanced 3-dB Gain Bandwidth

The second optimum prototype obtained from the optimization process, is a six-unit cell antenna with significantly enhanced 3-dB gain bandwidth. The optimized details of the



(a)



(b)

Figure 6.14: Simulation results of an optimized hybrid Bull's Eye antenna with enhanced 3-dB gain bandwidth response and comparison with a standard Bull's eye antenna with similar directivity/gain in (a) S11, (b) Directivity and realized gain.

hybrid antenna are $w_r = 5.67$ mm, $h_r = 1$ mm, $h_b = 1.5$ mm, $w = 10.4$ mm, while for the standard antenna of the same size and maximum directivity, it is $w = 12.3$ mm.

Fig. 6.14 shows the simulated S11, gain and directivity for the optimized hybrid corrugated antenna and the standard corrugated antenna of the same size, and similar gain. The novel hybrid design with a waveguide aperture, maintains a good S11 level below -10 dB. The maximum directivity is 17.3 dBi for both antennas, at 15.1 GHz.

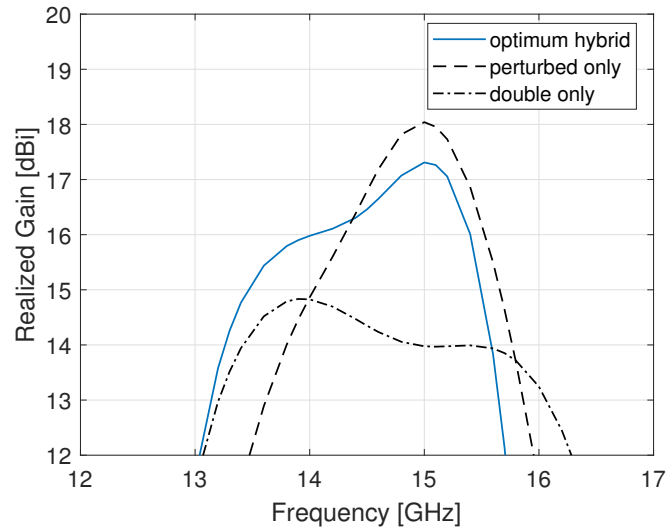


Figure 6.15: Contribution of each corrugation in the hybrid effect of the antenna with enhanced 3-dB gain bandwidth.

However, the fractional 3-dB gain bandwidth of the antenna is 15.67%, while for the standard antenna is only 11.1 %.

The effect of each corrugation in the realized gain of the hybrid antenna can be examined separately in Fig. 6.15. The first antenna consists of perturbed corrugations only and the second antenna consists of double corrugations only, with the same dimensions as with the optimum hybrid design. The maximum gain response of the hybrid model at around 15 GHz is generated by the perturbed corrugation, while a second peak at around 13.7 GHz is generated by the double corrugations. In a similar fashion with the prototype of Section 6.4.1, we can safely comment that the double corrugations contribute in the extension of the 3-dB gain bandwidth, due to the existence of a second mode at around 13.5 GHz.

The simulated radiation patterns are shown in Fig. 6.16, at the frequencies which determine the 3-dB gain spectrum. For the hybrid antenna, these frequencies are: lower -3 dB at 13.3 GHz, 0 dB at 15 GHz and upper -3 dB at 15.6 GHz. For the standard

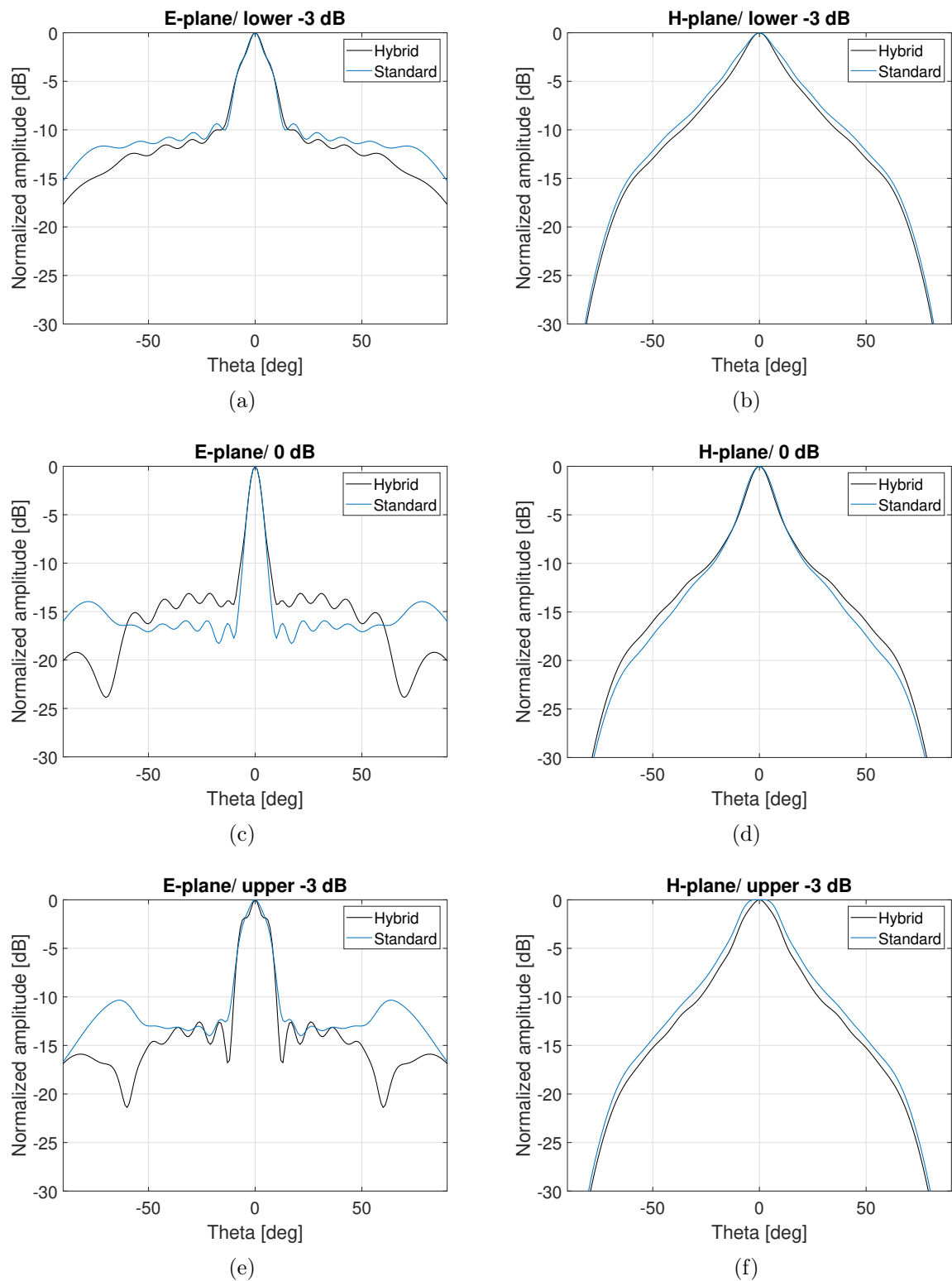


Figure 6.16: Simulated radiation patterns of the hybrid antenna with enhanced 3-dB gain bandwidth and the standard antenna of the same maximum gain. *E*-plane: (a) lower -3 dB, (c) 0 dB, (e) upper -3 dB. *H*-plane: (b) lower -3 dB, (d) 0 dB, (f) upper -3 dB.

antenna, they are: lower -3 dB at 14.13 GHz, 0 dB at 15 GHz and upper -3 dB at 15.7 GHz. At the frequency point of maximum gain, the side lobe level of the E -plane is at -13 dBi for the hybrid antenna and -16 dBi for the standard antenna, maintaining a highly directive lobe at broadside. At bigger angles (over $\pm 60^\circ$) the hybrid antenna performs better (side lobe level below -20 dBi), while for the standard antenna the side lobe level is higher than -15 dBi. At the limits of the 3-dB spectrum the hybrid antenna maintains a suppressed side lobe level compared to the standard antenna, especially at angles over $\pm 60^\circ$.

6.5 Implementation of Different Feeding Techniques on Hybrid Corrugated Bull's Eye Antennas

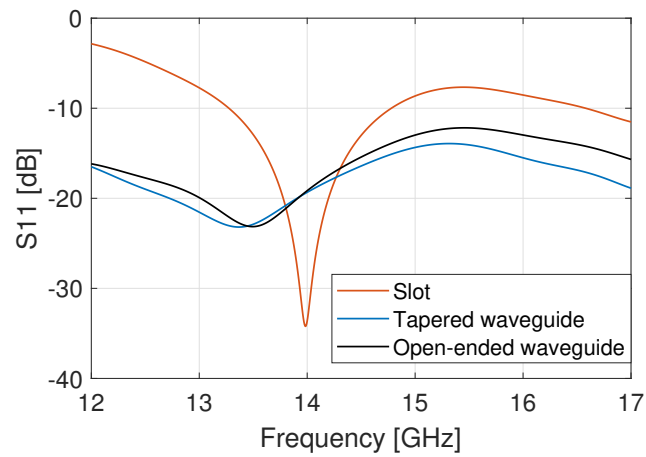
The feeding techniques of Chapter 4 are implemented in this Section on the optimum hybrid Bull's Eye antenna prototype of Section 6.4.1, which uses an open-ended waveguide aperture. This proposed design with flat gain response is compared against two identical corrugated antennas of the same number of rings, one with a subwavelength slot aperture and one with a tapered waveguide aperture with tapering factor $r = 2$. For the slot aperture implementation, a subwavelength slot of optimized dimensions is used with $s_x = 11.6$ mm and $s_y = 4.8$ mm. For the tapered waveguide implementation, the central ring diameter that surrounds the aperture is extended from 19.6 mm (d) to 21.6 mm. All other design details remain the same as their corresponding in Section 6.4.1.

Simulated results in S11, realized gain and directivity are compared in Fig. 6.17 for the three different feeding techniques of Chapter 4. The conclusions of Chapter 4 can be

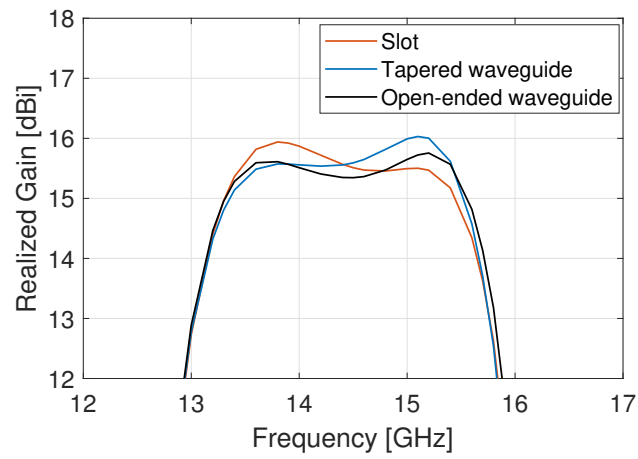
applied in this case of hybrid corrugations as well, as explained below.

The S11 bandwidth of the slot aperture is limited, as it is below -10 dB only between 13.25 GHz and 14.8 GHz. For the open-ended aperture antenna the S11 is below -12 dB at all the frequency band examined, while for the tapered aperture antenna the S11 is below -14 dB. The directivity plot for the slot aperture antenna consists of two peaks of similar magnitude (one around 13.7 GHz and one around 15.2 GHz), around 16 dBi. This similar magnitude is not maintained in the realized gain performance, where the peak around 15.2 GHz is about 0.5 dBi lower than the peak around 13.7 GHz. This loss in gain is attributed to the high reflection coefficient beyond 14.8 GHz. The other two implementations (open-ended waveguide and tapered waveguide), achieve a similar plot in directivity and realized gain due to the very good S11 performance. The 1-dB gain (directivity) bandwidth for all implementations is approximately 16.14% and the 3-dB gain (directivity) bandwidth is 19.64%.

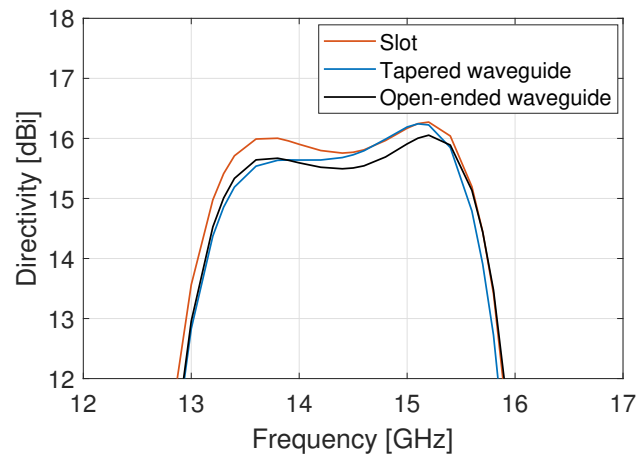
The conclusions from this simulation study of the three feeding aperture types are similar as in Chapter 4, verifying their scalability from low THz to microwave frequencies. The tapering of the waveguide aperture in this microwave implementation, however, does not offer a significant improvement in S11 compared to the open-ended waveguide. Likewise, the peak realized gain is similar (from 15.8 to 16 dBi) in all three implementations. It is preferable, therefore, to use an open-ended waveguide aperture as a compromise between a good S11 bandwidth and a high gain performance. Similar conclusions can be expected for the application of these feeding techniques on the optimum hybrid design of Section 6.4.2.



(a)



(b)



(c)

Figure 6.17: Comparison of the optimized hybrid Bull's Eye antenna with flat response with three different feeding techniques in simulated (a) S_{11} , (b) realized Gain and (c) directivity.

6.6 Conclusion

In this Chapter, novel corrugated unit cell designs have been presented at microwave frequencies, for the facilitation of potential fabrication. The perturbed and the double corrugation concept have been introduced for the first time with extensive simulation results, and next, they have been combined into a hybrid design. The optimization process of a hybrid Bull's Eye antenna with 6 rings has come up with two novel prototypes with enhanced performance characteristics.

The first novel prototype achieves a large 1-dB gain bandwidth of 16.14%, extended 3-dB gain bandwidth of 19.64% and maximum realized gain of 15.8 dBi. This design outperforms a conventional Bull's Eye antenna of the same gain and same size. The second novel prototype achieves an extended 3-dB gain bandwidth of 15.67% and maximum gain of 17.3 dBi, while for a standard Bull's Eye antenna of the same gain, the fractional bandwidth is only 11.1%. For each of the proposed antennas, a simulation study is presented that demonstrates the contribution of each corrugation type on the overall performance. It is suggested that the hybrid corrugations excite a second radiating leaky mode that contributes to the enhancement of the 1-dB (or 3- dB) gain bandwidth.

Additionally, the three feeding techniques presented in Chapter 4 have been applied on the optimum hybrid design with flat gain response. The conclusions from this simulation study verify the trends observed in Chapter 4, indicating the open-ended waveguide as the preferred feeding aperture with respect to satisfactory S11 and gain.

It should be noted that the presented hybrid Bull's Eye antennas are not the only designs produced by the optimization process that outperform their corresponding standard shaped antennas. Several optimized models, not presented in this thesis, have achieved an

extended 3-dB and 1-dB bandwidth along with a high gain, however, the models shown are the best compromise between high gain and broadband performance.

Chapter 7

Conclusions

7.1 Thesis Review

The scope of this dissertation has been to investigate the leaky wave phenomena associated with radiation from periodically corrugated metallic surfaces, as well as the proposal of novel practical antennas of this type with improved radiation characteristics. In particular, leaky wave analysis methods have been proposed and implemented for the first time on corrugated antennas with gaps larger than half-wavelength, deriving from the mathematical background of Chapter 2. Furthermore, novel corrugated antennas at microwave and low THz frequencies have been designed, fabricated and measured that outperform several known implementations that have been briefly reviewed in Chapter 1.

The characteristics of the leaky mode excited from periodically corrugated metallic surfaces with gaps larger than half wavelength have been studied for the first time in Chapter 3, with the use of classical electromagnetic theory. A novel analytical periodic method has been proposed for this purpose, which consists in the numerical solution of a

transverse resonance equivalent network and the extraction of the complex wavenumber of a higher order mode inside the gaps. Additionally, a unit cell dispersion analysis technique and the known matrix pencil method have been applied for the first time on such corrugated unit cells (antennas). All methods have been proven to be very accurate in the estimation of the leaky mode, and the limitations of each have been discussed. The farfield behaviour of the infinite size symmetrically fed antennas has then been calculated with a simple array factor approach. Theoretically calculated radiation patterns at frequencies of interest are compared with simulated data from finite size antennas, with very good agreement. This is another contribution of this Chapter, as it is the first time a quantitative approach to the calculation of radiation patterns of corrugated antennas with larger gaps is available. The methodologies developed in this Chapter have been later used in Chapter 5, for the dispersion analysis of the proposed dual-depth corrugated antenna, and in Chapter 6, for the comprehension of the leaky wave behaviour of the hybrid corrugated antenna.

The problem of the inherent limited bandwidth of periodically corrugated antennas has been addressed in Chapters 4 to 6. In Chapter 4, novel feeding mechanisms for a low THz Bull's Eye antenna have been proposed. The typical subwavelength slot aperture, which results in a narrowband matching response, has been replaced with an open ended waveguide aperture and then, a tapered waveguide aperture. A reflection coefficient below -10 dB has been secured with the waveguide aperture and below -14 dBi with the tapered waveguide aperture at a very wide frequency band. A prototype with a tapered aperture has been fabricated and measured results exhibit good agreement with simulations.

In Chapter 5, the narrowband gain performance of standard Bull's Eye antennas has

been tackled by introducing a novel design technique that exploits the depth qualities of the corrugations. The proposed configuration is a dual-depth corrugated antenna, with high gain and enhanced 3-dB gain (directivity) bandwidth. The antenna outperforms standard Bull's Eye antennas of the same size and the same maximum directivity. A suitable leaky wave analysis of the single depth standard antennas gives further insight into the complex leaky wave phenomenon of the dual depth antenna. The optimum dual depth antenna with 10 rings at low THz was fabricated and measured results have been presented.

Chapter 6 has presented another contribution of this research work towards the enhancement of the 3-dB gain bandwidth of Bull's Eye antennas, by introducing novel types of complex shaped corrugations. First, a perturbed corrugated unit cell has been investigated, with significant increase in maximum directivity. Next, a double corrugation concept has been presented that excites two strong leaky modes when the central gap of the corrugations is up to half wavelength. A hybrid corrugated unit cell has been then explored, that combines both concepts. The generated hybrid Bull's Eye antennas at Ku band operate with extraordinary characteristics, such as large 1-dB gain bandwidth and extended 3-dB gain bandwidth. The optimum prototype with flat gain response was fabricated, however measurements could not be performed due to restricted campus operations. In Appendix A, measurements have been presented for a conventional Bull's Eye antenna at 15 GHz, as a similar agreement is expected for the hybrid Bull's Eye antenna at this frequency spectrum.

7.2 Future Directions

A known limitation of the unit cell method associated with the calculation of the attenuation constant is the failure to generate logical values for α when the electric component of the near radiated field is strong (high error rate). The setup for such a calculation could be further investigated, as this method offers the significant advantages of simplicity and small computational time compared to other full-wave methods, i.e. the matrix pencil. Furthermore, the approximation of the radiation patterns in this thesis considers only the radiation produced by the excitation of the longitudinal leaky mode. As future development, more complex phenomena could be inserted into the analysis, such as an estimation of the reflections when the leaky wave reaches the edge of the finite size structure (edge diffraction phenomenon). The analysis could also be expanded in order to include non-periodic or holographic leaky wave antennas of this type.

The novel Bull's Eye prototypes presented in this thesis have tackled successfully the inherent bandwidth problem of conventional corrugated planar antennas, by introducing a dual depth concept and a hybrid corrugation concept. However, the gain bandwidth could be further improved by combining both the dual depth and the hybrid design methodologies into a single design. Also, this dissertation offers a first approach to the comprehension of the leaky wave radiation of such antennas. As a further step, a rigorous leaky wave analysis could be developed for the quick and accurate calculation of the excited fast waves deriving from a complex shaped unit cell. This could assist in the development of quick design methodologies that will allow an effective modelling of such antennas, depending on the desired farfield characteristics (extended 1-dB bandwidth and 3-dB bandwidth, maximum gain etc). The known reciprocity technique for radiation

pattern calculation could be implemented on the complex shaped antennas of Chapter 6 for the theoretical calculation of their farfield patterns.

7.3 Impact

The findings of this dissertation have been presented or accepted for presentation at several international conferences , namely the European Conference on Antennas and Propagation (EuCAP), IEEE International Symposium on Antennas and Propagation (AP-S), Loughborough Antennas and Propagation Conference (LAPC), International Workshop on Antenna Technology (iWAT) and Antennas and Propagation Conference (APC). Parts of this work have been submitted to IEEE Antennas and Wireless Propagation Letters, IEEE Transactions on Terahertz Science and Technology, or are currently prepared for submission to IEEE Access or Nature Scientific Reports.

APPENDICES

Appendix A

Measurement of a Ku Band Bull's Eye

Antenna

A standard Bull's Eye antenna at around 15 GHz has been designed with the tapered waveguide aperture of Chapter 4. The antenna composes of 5 concentric rings with optimized dimensions as $w = 13.3$ mm, $d = 19.6$ mm, $t = 3.3$ mm, and total plate height $h = 6.5$ mm. The tapered waveguide aperture is of dimensions $t_x = 20$ mm and $t_y = 12$ mm. The antenna was fabricated with CNC milling on an aluminium plate. Fig. A.1 shows the fabricated prototype.

Measured results of S11 and realized gain, compared to simulations, are shown in Fig. A.2. The experimental reflection coefficient demonstrates a very satisfactory transmission

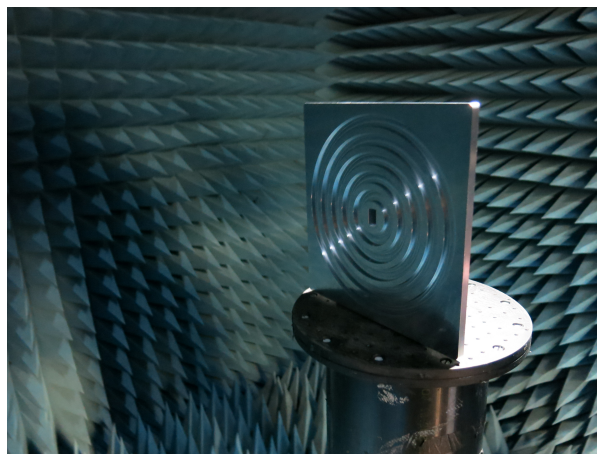
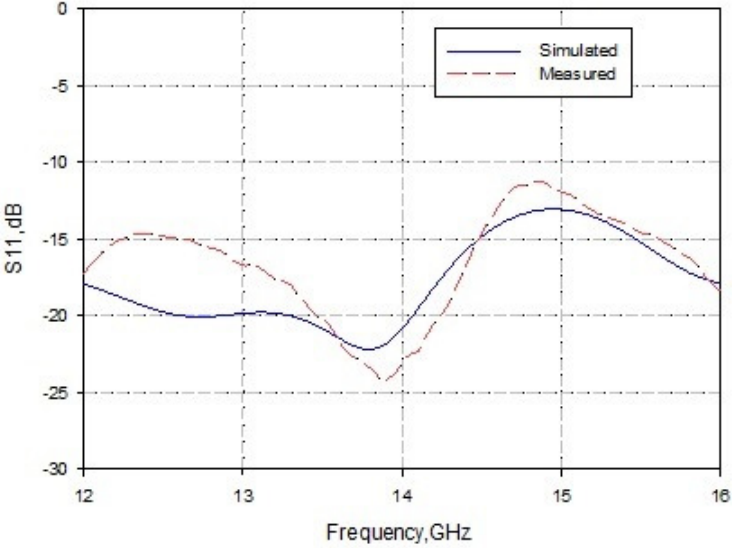
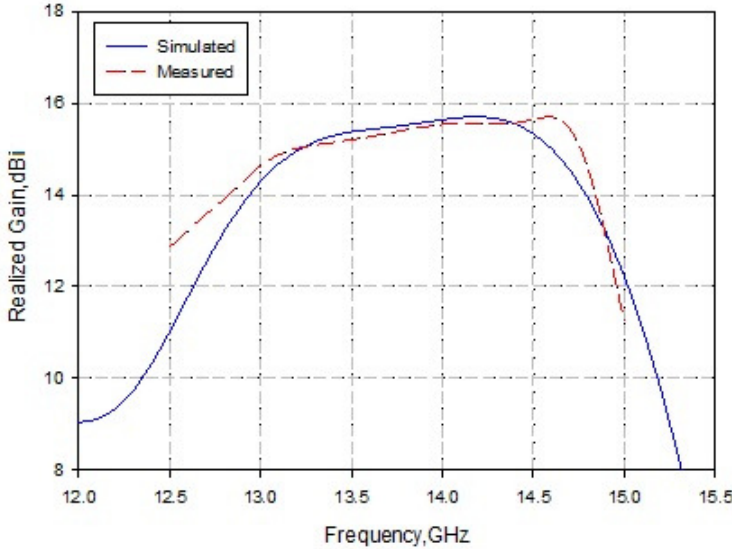


Figure A.1: Fabricated prototype of a 15 GHz standard Bull's Eye antenna.



(a)



(b)

Figure A.2: Measured (a) S11 and (b) Realized Gain of the standard Bull's Eye antenna with tapered aperture compared to the simulated results.

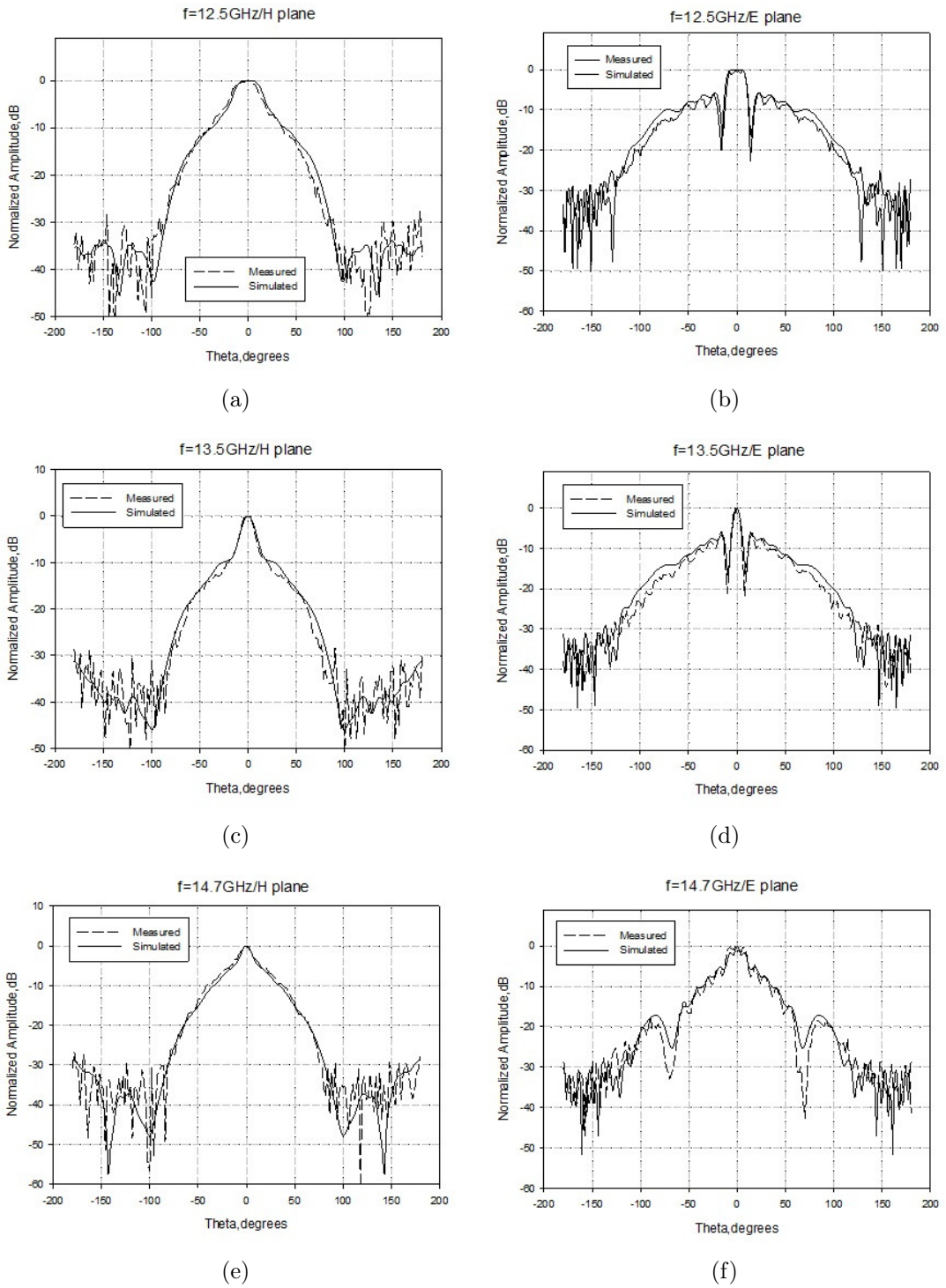


Figure A.3: Measured far-field radiation patterns of the tapered Bull's Eye antenna at 12.5 GHz: (a) H -plane and (b) E -plane, 13.5 GHz: (c) H -plane and (d) E -plane, and 14.7 GHz: (e) H -plane and (f) E -plane.

in all the frequency band examined (below -10 dB), while the measured realized gain reaches a maximum value of 15.7 dBi at 14.7 GHz. The experimental 3-dB gain bandwidth is even larger than the predicted by CST Microwave Studio, approximately 21%. Overall, a very good agreement between simulated and measured results can be noticed.

Fig. A.3 depicts the measured far-field patterns in both radiation planes at specific frequencies of interest, compared to the simulated patterns. The E -planes produce a very narrow beam, however they generate strong side lobes in all the frequencies shown. The best performance in both planes can be observed at 13.5 GHz, where the S_{11} parameter obtains its lowest value (below -20 dB).